

Time Series Searching, Forecasting, and Classification 1  
with Applications in Bioinformatics 2  
時系列の探索・予測・分類とその生命情報学へ 3  
の応用 4

Coleman Yu 5  
余 浩旻



# Abstract

7

Time series data are ubiquitous across many different fields. Much of the data are inherently time series data. Additionally, some data, such as strings, images, and object shapes, that are not originally time series data, can be transformed into time series. Many data mining tasks, such as classification, clustering, and motif finding, have been defined for time series data. Hence, by developing appropriate transformation methods, we can apply a plethora of well-established time series methods to our problems.

This thesis contributes two aspects in time series data mining and bioinformatics. They are a novel application of time series classification to solve complex biological problems by transforming biological data into time series and developing a more expressive distance measure framework that removes certain underlying assumptions.

In the first part, we demonstrate the utility of time series analysis in bioinformatics by studying the problem of predicting Human Dicer Cleavage Sites. Recall that bioinformatics operates at the intersection of **biology**, **biotechnology**, and **informatics**. In this work, we formulate a specific **biology** problem, which is predicting Human Dicer Cleavage sites in microRNA biogenesis, into a machine learning framework. In particular, a multivariate time series classification problem, which is the **informatics** part. Due to current limitations in **biotechnology**, we are constrained to using 1-D RNA sequence inputs rather than 2-D or 3-D data, because these are more expensive to obtain. We propose MTSCCleav, a method that encodes RNA sequences and the probabilities of base pairs in predicted secondary structures into time series data. To the best of our knowledge, we are the first to make use of the probabilities of base pairs in this kind of classification task on RNA data. By doing this, we frame the problem of predicting Human Dicer Cleavage sites into a Multivariate Time Series Classification (MTSC) problem. Existing approaches rely on opaque deep neural networks or complex feature engineering. They are slow, and the feature engineering is over-designed. In contrast, our approach is simple, intuitive, and computationally efficient. The proposed transformation methods allow us to use any well-established time series tools to analyze this biological problem. Experiments demonstrate that MTSCCleav achieves comparable and even better accuracy to state-of-the-art methods while delivering a 3.7X to 28.8X speedup. Furthermore, our perturbation experiments reveal that regions near the center of pre-miRNAs are essential for cleavage-site prediction, consistent with the existing literature.

39 In the second part, we address the limitations of existing similarity measures. Simi-  
40 larity search is a core subroutine in time series data mining tasks. For example, recent  
41 studies show that a simple 1-NN classifier with an appropriate distance measure can out-  
42 perform many advanced, complicated methods. While Dynamic Time Warping (DTW)  
43 and Uniform Scaling (US) are prevailing measures for handling local distortions and  
44 global scaling, respectively, and some studies have demonstrated that combining both  
45 DTW and US is necessary to obtain meaningful results. Current approaches apply a  
46 single scaling factor to the entire sequence. We argue that since distinct phases of a pro-  
47 cess often evolve at different speeds, a single scaling factor is insufficient. We introduce  
48 the first distance measure framework, namely PSD, that achieves invariance to multiple  
49 scaling factors. We also provide speed-up techniques to enable efficient computation of  
50 the PSD. Experiments show that PSD better reflects the similarity between time series  
51 with multiple phases, and that the identified phases (segmentation) provide a clearer  
52 understanding of the data.

53 In the third part, we study a time series primitive, namely matrix profile, in the  
54 application of time series forecasting. For a given time series  $T$  and an integer  $m$ , the  
55 matrix profile provides the information about (1) the location of its nearest neighbor  
56 and (2) the distance between it and the nearest neighbor of **each**  $m$ -subsequence in  $T$ .  
57 Obviously, the matrix profile also provides us the information for the  $k$ -nearest neighbors  
58 of each subsequence simply by running the same algorithm for  $k$  times. In our application,  
59 we are only interested in the left nearest neighbors of each subsequence because they  
60 refer to the historical occurrences. We can obtain the immediate subsequences of these  
61 historical occurrences as covariates to feed into the forecaster to improve its accuracy.

62 Collectively, this thesis advances the fields of time series data mining and bioinfor-  
63 matics by demonstrating the use of time series analysis to address fundamental biological  
64 questions and proposing a new, more expressive distance measure framework.

# Acknowledgements

65

To begin, I want to express my deepest gratitude to my PhD supervisor at Kyoto University, Prof. Tatsuya Akutsu. I thank him for his kindness and patience. He is a brilliant researcher who can explain complex concepts simply. In a seminar, he showed that simply using clear notation makes presentations much easier to follow. More importantly, he helps students when they are in “valleys” in their lives. When a car is off track, it needs a push—so do people. I am equally indebted to my MPhil supervisor at The Hong Kong University of Science and Technology (HKUST), Prof. Raymond Chi-Wing Wong. He has continued to help and advise me even after I graduated from HKUST.

Akutsu-sensei taught me the importance of reading good materials. In the weekly seminars, he organized reading seminars, assigning some of his favorite books for us to read and discuss. His favorite book is “Probability and Computing” by Mitzenmacher and Upfal. Additionally, through the journal club he organized, students were asked to present the core ideas from their ten selected papers published in leading venues, such as Nature, Science, Cell, and PNAS. Reading beyond my fields helped me identify research gaps others missed. I think some great ideas are born when we merge the ideas from different fields. He also emphasized the importance of mathematics and proof. It is what computer scientists can stand out in the field of bioinformatics. I think it becomes especially true now, since advances in AI make it possible for almost everyone to code (i.e., Vibe coding). He advised me to use the existing tools, libraries, and studies to leverage my own research. He also taught me that a good researcher must master both oral and written presentation; otherwise, others may misinterpret your talent and the effort you put in. When we are reading a paper, he urges us to identify the novelty and analyze the pros and cons of the paper.

Raymond taught me the power of focus and “First Principles”. I was always surprised that he did not use reference management software like Zotero, preferring to annotate hard copies and even type .bib files manually. He told me that when he starts to do research, he will print out the papers and get focused on the stack of papers (hard copies) in front of him. I am not saying it is beneficial not to use tools, but I want to emphasize the power of focus that underlies his work routine. He taught me that every good research starts with a set of good papers. He also emphasized that there is no right or wrong in research, only what you choose to do about it. His research receipt works as follows. When you

97 are tackling a problem, you first review the relevant existing studies to understand the  
98 state of the art (SOTA) for it. If the existing work addresses your particular problem,  
99 you can apply and adapt it to your problem setting. But most of the time, since your  
100 problem must be a particular version of a general problem, the existing general solution  
101 should not work well for it. It means that you have some room to improve it. And this  
102 is the research gap!. It reminds me of when we deal with the NP-complete problem.  
103 As Kleinberg and Tardos's Algorithm Design (Chapter 10) suggests, an NP-complete  
104 problem (assuming  $P \neq NP$ ) does not allow us to have an algorithm that possesses  
105 all three of the following desired properties simultaneously: Efficiency, Correctness, and  
106 Generalization. Hence, it is sometimes preferable to address a specific instance of the  
107 problem rather than the general one. He also emphasized the theory. He consistently  
108 noted that you need to add theory to the paper to strengthen it. He always mentioned  
109 that you need three motivations (why you are doing it) and three contributions (what you  
110 have done). Sometimes, I ask why he can write so fast, and he replies, "If you know what  
111 you are doing, then you write fast.". He also taught me that when you don't know some  
112 of the ideas, you just go back to the original idea. Doing a "deep first search" can help  
113 you reach the first principle, a concept that Elon Musk, one of the greatest entrepreneurs  
114 of our time, always emphasized. Without these two supervisors, I would not have made  
115 it this far. I could not have finished this program.

116 I would like to take this opportunity to share some of my thoughts on my PhD journey.  
117 I hope the readers may learn something from what I have gone through. My PhD journey  
118 was, to quote Dickens, "the best of times and the worst of times", and to quote Churchill,  
119 "This was their finest hour". For the best parts, it allows me to explore both in my daily  
120 life and in my research. I tried many things, walked many roads, drank many colas and  
121 alcohol, and met many people. This helped me see problems from new perspectives.  
122 Regarding the worst parts, I am reminded of a quote from one of my favorite movies,  
123 "Les Choristes": "Fond de l'étang". It literally means "Bottom of the Pond". At times, I  
124 felt like a frog at the well's bottom, trying hard to get out. Research is fun but also hard.  
125 Research is about exploring something new. It is about publishing (so others can learn  
126 from it). When I am stuck, the best solution is to aim for a reachable, well-defined goal.  
127 The goal should be clear, with obvious rewards and requirements. Also, make sure the  
128 effort of your actions can be accumulated. Like the frog, do not jump randomly, but aim  
129 to move to stable platforms towards escape. Then, each jump matters for your progress.  
130 Two of the materials helped me; they are "Eat the Frog!" and "THE PH.D. GRIND".

131 I would like to thank my thesis committee members. I would like to acknowledge  
132 Tamura-sensei and Mori-sensei (a former member) of the Akutsu laboratory. Tamura-  
133 sensei taught me to focus on the input-output relationship when encountering new algo-  
134 rithms/methods, and Mori-sensei introduced me to the fascinating application of time-  
135 series analysis to gene expression data, especially in trajectory inferences (i.e., pseudo-

time). I would like to thank the many communities that made my life in Japan colorful. 136  
Thank you to the people of the dormitories where I lived at the Uji and Yoshida cam- 137  
puses. I am grateful to my Japanese language teachers. I also cherish the friends I met 138  
through Akutsu’s laboratory and the extracurricular activities, including Kendo, Table 139  
Tennis, Naginata, Karate, and Aikido. I also met many interesting people from various 140  
international student events. 141

I am honored to receive the Asian Future Leaders Scholarship Program (AFLSP) 142  
scholarship to support my studies in Japan. I have made a great choice by enrolling in 143  
Kyoto University Design School, which has provided me with many valuable interdisci- 144  
plinary experiences and opportunities to meet people outside my field. In this program, 145  
I have conducted fieldwork in Okinawa, Hong Kong, and Bali, a rare opportunity for 146  
researchers in computer science. I would also like to thank the Institute for Chemical 147  
Research (ICR) for the Research Assistant position in the Akutsu laboratory. 148

Finally, I would like to express my deepest gratitude to my family and my friends who 149  
have stayed by my side with their countless acts of support; I have nothing to return to 150  
them but my love and time. 151

A special acknowledgment goes to my niece. As you grow up, I hope you explore the 152  
world and fulfill your eagerness for knowledge. Find materials that interest you. One 153  
day, you might find this thesis online and, I hope, find it worth reading and inspiring. 154



# List of Publications

155

This thesis is based on the following papers.

156

- (Chapter 3) **Coleman Yu**, Raymond Chi-Wing Wong, and Tatsuya Akutsu, “MTSC-Cleav: a Multivariate Time Series Classification (MTSC)-based Method for Predicting Human Dicer Cleavage Sites”, submitted to *IEEE Access*, under review 157  
158  
159
  - (Chapter 4) **Coleman Yu**, Tatsuya Akutsu, and Raymond Chi-Wing Wong, “Scaling with Multiple Scaling Factors and Dynamic Time Warping in Time Series Searching”, submitted to *IEEE Access*, under review 160  
161  
162
  - (Chapter 5) **Coleman Yu**, Raymond Chi-Wing Wong, and Tatsuya Akutsu, “Leveraging Nearest Neighbors for Time Series Forecasting with Matrix Profile”, in preparation 163  
164  
165
- Other publications 166
- **Coleman Yu** and Raymond Chi-Wing Wong, “A Melody Composer for both Tonal and Non-Tonal Languages”, the 43rd International Computer Music Conference 2017, Shanghai, China on 16-20 Oct, 2017 167  
168  
169
  - Yi Zheng, Bogdan Enescu, Jianchang Zhuang, and **Coleman Yu**, “Data replenishment of five moderate earthquake sequences in Japan, with semi-automatic cluster selection”, *Earthquake Science*, 34:310-322, 2021 170  
171  
172



# Contents

173

<b>Abstract</b>	<b>i</b>	174
<b>Acknowledgements</b>	<b>iii</b>	175
<b>List of Publications</b>	<b>vii</b>	176
<b>List of Figures</b>	<b>xiii</b>	177
<b>List of Tables</b>	<b>xv</b>	178
<b>1 Introduction</b>	<b>1</b>	179
1.1 Background . . . . .	1	180
1.2 Contributions . . . . .	2	181
1.3 Organization . . . . .	2	182
<b>2 Preliminaries</b>	<b>3</b>	183
2.1 Distance Measures . . . . .	3	184
2.1.1 Euclidean Distance (ED) . . . . .	4	185
2.1.2 Dynamic Time Warping (DTW) . . . . .	4	186
2.1.3 Derivative Dynamic Time Warping (DDTW) . . . . .	5	187
2.1.4 Weighted Dynamic Time Warping (WDTW) . . . . .	5	188
2.1.5 Weighted Derivative Dynamic Time Warping (WDDTW) . . . . .	6	189
2.1.6 Shape Dynamic Time Warping (shapeDTW) . . . . .	6	190
2.1.7 Amercing Dynamic Time Warping (ADTW) . . . . .	6	191
2.2 Classification . . . . .	7	192
2.2.1 Ridge Classifier . . . . .	7	193
<b>3 MTSCCleav: a Multivariate Time Series Classification (MTSC)-based Method for Predicting Human Dicer Cleavage Sites</b>	<b>9</b>	194
3.1 Background . . . . .	10	196
3.2 Methods . . . . .	12	197
3.2.1 Data Preparation . . . . .	13	198

199	3.2.2	Time Series Encoding . . . . .	16
200	3.2.3	Time Series Classification . . . . .	19
201	3.2.4	Evaluation Metrics . . . . .	23
202	3.3	Results . . . . .	24
203	3.3.1	Channel Ablation Study . . . . .	25
204	3.3.2	Predictive Performance . . . . .	26
205	3.3.3	Running Time Analysis . . . . .	28
206	3.3.4	Subsequence Importance . . . . .	29
207	3.3.5	Summary . . . . .	30
208	3.4	Discussion . . . . .	30
209	3.5	Concluding Remarks . . . . .	31
210	<b>4</b>	<b>Scaling with Multiple Scaling Factors in Time Series Searching</b>	<b>33</b>
211	4.1	Background . . . . .	34
212	4.2	Related Work . . . . .	37
213	4.3	Preliminaries . . . . .	37
214	4.3.1	Euclidean Distance (ED) . . . . .	38
215	4.3.2	Dynamic Time Warping (DTW) . . . . .	39
216	4.3.3	Uniform Scaling (US) . . . . .	41
217	4.3.4	Uniform Scaling & Dynamic Time Warping (USDTW) . . . . .	42
218	4.3.5	Lower Bounds for DTW and USDTW . . . . .	43
219	4.4	Piecewise Scaling Distance . . . . .	46
220	4.4.1	Piecewise Scaling & Dynamic Time Warping (PSDTW) . . . . .	47
221	4.4.2	Speedup Techniques . . . . .	49
222	4.4.3	Guided Distance . . . . .	54
223	4.5	Experiments . . . . .	54
224	4.5.1	Experimental Setup . . . . .	54
225	4.5.2	Experimental Results . . . . .	57
226	4.6	Concluding Remarks . . . . .	60
227	<b>5</b>	<b>Leveraging Nearest Neighbors for Time Series Forecasting with Matrix Profile</b>	<b>63</b>
228	5.1	Introduction . . . . .	63
229	5.2	Related Work . . . . .	66
230	5.3	Method . . . . .	67
231	5.3.1	Problem Formulation . . . . .	68
232	5.3.2	Evaluation Method . . . . .	68
233	5.3.3	Gradient Boosting Regression Tree (GBRT) . . . . .	70
234	5.3.4	Matrix Profile . . . . .	71

5.4	Experiments . . . . .	71	236
5.5	Conclusion and Future work . . . . .	72	237
5.5.1	Conclusion . . . . .	72	238
5.5.2	Future Work . . . . .	72	239
<b>6</b>	<b>Conclusion and Future Directions</b>	<b>75</b>	<b>240</b>



# List of Figures

241

2.1 Alignments. . . . .	4	242
3.1 Predicted secondary structure of the sequence $S$ of pri-miRNA “hsa-let-7a-1” <sup>1</sup> . Experimental evidence suggests that the two deviated mature miRNAs are $UGA \cdots GUU$ and $CUA \cdots UUC$ . They are $S(6 : 27)$ and $S(57 : 77)$ (Both ends are inclusive.). The ends are highlighted in <b>bold</b> . Since $S(6 : 27)$ ( $S(57 : 77)$ ) is near the 5' (3') end, we call it “5p (3p) mature miRNA”. The two scissors indicate the two cleavage sites. The color intensity of the nodes reflects their base-pair probability in this predicted secondary structure. The deeper the color, the higher the probability. The unpaired nodes are uncolored. The raw figure is generated by RNAfold web server <sup>2</sup> . . . . .	11	252
3.2 The overall pipeline of this study. Symbol notations: Cylinder - Dataset, Rectangle - Process, Parallelogram - Input / Output, Rounded Rectangle - Component. . . . .	13	255
3.3 Relationship of the proposed encoding methods. . . . .	16	256
3.4 Features generation in the transformation . . . . .	20	257
3.5 Convolutions of HYDRA for each input time series with a set of random kernels $w$ , organized into $g$ groups with $k$ kernels each. . . . .	21	259
3.6 CD diagrams of channel ablation study. . . . .	26	260
3.7 CD diagrams to compare different classifiers. . . . .	27	261
3.8 CD diagrams to compare different encoding methods. . . . .	28	262
3.9 Results of the perturbation experiment. . . . .	30	263
4.1 Applying nearest neighbor interpolation on $Q$ , which result in Scaled $Q$ , that can better reflect its similarity with $C$ . . . . .	35	265
4.2 $Q$ and $C$ are in different rates. A stretching version of $Q$ is similar to a prefix of $C$ , but not the whole $C$ . . . . .	35	267
4.3 Intuition of piecewise scaling (PS). . . . .	36	268
4.4 Z-normalization. Resulting time series have mean = 0 and std = 1. . . . .	38	269
4.5 Visualization of $D$ with local constraints. The black cells form the warping path. . . . .	40	271

272	4.6	Visualization of LB <sub>Keogh</sub> and LB <sub>Shen</sub> . . . . .	44
273	4.7	Relationship of $L_Q$ and $L_C$ . . . . .	51
274	4.8	Visualization of the GunPoint dataset. Left (Right): A time series of the “Gun” (“Point”) scenario. Critical periods, such as “Aiming”, are annotated.	55
275	4.9	The red solid time series shows an instant in the target set. The blue dashed time series shows an instant in the query set. . . . .	55
276	4.10	Runtime and number of distance calls comparison of GunPoint dataset. (a)-(d) $P = 1$ , (e)-(h) $P = 2$ , (i)-(l) $P = 3$ . . . . .	59
279	5.1	Flattening a 2D window of size $(1 + M) \times w$ to a 1D vector of length $w + M$ . The resulting vector serves as the <i>predictor</i> for the regressor. Its expected <i>response</i> is the vector of length $h$ . The regressor learns from this predictor-response pair. . . . .	64
280	5.2	The <b>left</b> ( <b>right</b> ) matrix profile and the <b>matrix profile</b> of a time series. The <b>matrix profile</b> shows the distances between each $m$ -subsequence and its nearest neighbor, where $m$ is a user-given value. The <b>left</b> ( <b>right</b> ) matrix profile shows the same information but is limited to its left (right) nearest neighbor. For a particular $m$ -subsequence shown by the right gray box, its nearest neighbor is the left gray box, as indicated by the dashed line in the <b>left matrix profile</b> and the <b>matrix profile</b> . Similarly, the nearest neighbor of the left gray box is the right gray box, as indicated by the dashed line in the <b>right matrix profile</b> and the <b>matrix profile</b> . The first (last) point in each box is denoted by a <b>red</b> circle (triangle). $h$ denotes the length of the immediate subsequence of the nearest neighbor. Intuitively, this subsequence should be similar to the immediate subsequence (i.e., future) of the right gray box. To note, the <b>left</b> ( <b>right</b> ) matrix profile starts (ends) at a later (earlier) index because the corresponding nearest neighbor with length $m$ does not exist. . . . .	65

# List of Tables

299

3.1	Selected representative records from miRBase. For the last two columns, the first line shows the name, the second line shows its location in the original sequence, and the third line indicates whether its existence has experimental evidence. The selected one is highlighted in <b>bold</b> . . . . .	300 301 302 13 303
3.2	The whole sequence of “hsa-let-7a-1” and its predicted secondary structure by RNAfold. The corresponding positions of the two mature miRNAs and the probability of the unpaired “U” are highlighted in <b>bold</b> . . . . .	304 305 14 306
3.3	The first row shows the “four strings” of “hsa-let-7a-1”. Their complementary strands are shown in the second row. As a whole, they are referred to as the “eight strings”. . . . .	307 308 15 309
3.4	Time series encoding. $P$ is the corresponding base-pair probability sequence of $S$ . $p_i = 1$ if we encode $S$ without incorporating base-pair probability sequence. . . . .	310 311 18 312
3.5	Comparison of rocket-based classifiers [1]. $\mathcal{N}(0, 1)$ : a standard normal distribution, $U(0, 1)$ : a uniform distribution between 0 and 1, 1 <sup>st</sup> order difference: $\Delta T = t_2 - t_1, t_3 - t_2, \dots, t_n - t_{n-1}$ . . . . .	313 314 23 315
3.6	Channel ablation study. The best results are highlighted in <b>bold</b> . . . . .	25 316
3.7	Performance on the 45 combinations between encoding methods and the ROCKET-based classifiers. The best results are highlighted in <b>bold</b> . . . . .	317 27 318
3.8	Comparative analysis between MTSCCleav with the best combination of the encoding method and classifier, with the SOTA, DiCleave, on the three datasets. The best results of using MiniROCKET have also been shown to compare the computational efficiency. The best results are highlighted in <b>bold</b> . . . . .	319 320 321 322 28 323
4.1	Details of the ten datasets for the experiments . . . . .	56 324
4.2	The accuracy comparison for eight distance measures of the GunPoint dataset . . . . .	325 57 326
4.3	The accuracy comparison for six PSED-guided distance measures of the GunPoint dataset . . . . .	327 58 328
4.4	The accuracy comparison for eight distance measures of the ten datasets	60 329

330	4.5	The accuracy comparison for six PSED-guided distance measures of the		
331		ten datasets . . . . .	60	
332	4.6	The number of distance calls and runtime on PSED_vanilla and PSED_parallel_bsf		
333		of the ten datasets . . . . .	61	
334	5.1	Dataset Statistics. $N$ is the number of time series in the dataset, while		
335		$ T  = n$ is the length of each time series. “rate” refers to the measuring		
336		rate. $w$ is the size of the look-back window. $h$ is the size of the forecasting		
337		window, also known as the forecasting horizon. $T_{\text{train}}$ is the training subse-		
338		quence of $T$ . $T_{\text{test}}$ is the test subsequence of $T$ . To note, $ T_{\text{train}}  +  T_{\text{test}}  = n$ .		
339		. . . . .	71	

# Chapter 1

340

## Introduction

341

### 1.1 Background

342

Human generates a ton of data nowadays. We are producing more new data in one single day today than in the first twenty-one centuries of AD combined. We are drowning in information but thirsty for knowledge. It is natural for us to develop computational methods to accelerate the process of “harvesting” knowledge from information.

343

344

345

346

Computational tasks focus on the relationship between input and output. We would like to find the hidden function behind. To note, there are two ways to solve a problem. One is the algorithmic approach, and the other is the machine-learning approach. In Chapter 3, it demonstrates a machine learning approach to analyze a biology problem. In Chapter 4, we solve an algorithmic problem on distance measure.

347

348

349

350

351

There are two large categories of machine learning. They are supervised learning and unsupervised learning. Classification may be the most intuitive form of supervised learning. The input is data points with labels. We learn a model from the relationship between data points and the labels. The model predicts the labels for the new data points. They have many applications. For example, in medical applications, it involves classifying patients as healthy or diseased, or tumors as benign or malignant. The term “supervised” means the model has access to labeled data. In other words, it requires labeled training examples that provide ground truth. So, the model can learn the boundary between the categories. Our first study focuses on a classification problem in biology.

352

353

354

355

356

357

358

359

360

A representative of unsupervised learning is undoubtedly clustering. We aim to group data into distinct clusters. The key difference is that the data lack predefined labels. By grouping them, we aim to identify natural patterns hidden in the data. One example is clustering cells based on their gene-expression profiles. These clusters might reveal distinct cell types. Note that we do not have the ground truth for the cluster set. In bioinformatics, we typically use enrichment analysis to determine whether specific gene functions are enriched in these clusters. Cell types often show enrichment for genes

361

362

363

364

365

366

367

368 responsible for specific functions. This set of genes defines their biological role. In  
369 clustering, we first need to define a measure of similarity between two objects. And  
370 what should be ignored. This is called invariance. For example, in image classification,  
371 it should be invariant with respect to the zooming effect and the rotation effect. In  
372 Chapter 4, we define a new distance measure framework that achieves invariance when  
373 two time series are in different scaling factors.

## 374 1.2 Contributions

375 In this study, our contributions mainly include two parts. First, we propose the usage  
376 of the base pair probability sequence from the predicted secondary structure of RNA se-  
377 quence as a new information for the classification task. We apply Rocket-based classifiers  
378 to identify the human dicer cleavage sites. Because of the simplicity of the transformation  
379 method and the classifiers, our proposed method achieves 3.7X to 28.8X speedup while  
380 achieving better or comparable results than the current state-of-the-art method. Second,  
381 we propose a new distance measure framework, namely PSD, that can incorporate any  
382 existing distance measures to achieve invariance for two time series with multiple rates.  
383 Experiments show that our methods outperform ED, DTW and the other five DTW-  
384 based methods. Besides, we propose to use the segmentation result returned by PSD  
385 to improve the accuracy of other distance measures. Third, we propose leveraging left  
386 nearest neighbors for each forecasting window as new covariates to improve the accu-  
387 racy of the underlying forecaster. We use a simple gradient boosting regression tree as  
388 the underlying forecaster. Experiment shows that this simple method can improve the  
389 accuracy.

## 390 1.3 Organization

391 In Chapter 2, we review some of the basic knowledge in biology and time series data  
392 mining, in particular, we focus on distance measures and Rocket-based classifiers. In  
393 Chapter 3, we introduce our study of the problem of predicting human dicer cleavage  
394 sites. We proposed a novel approach to frame this task as a multivariate time series  
395 classification problem by introducing nine encoding methods and making use of Rocket-  
396 based classifiers. In Chapter 4, we introduce a new distance measure framework, namely  
397 PSD. It releases the assumption that there is only one scaling factor existing throughout  
398 the whole time series. In Chapter 5, we introduce how to create new covariates in time  
399 series forecasting using matrix profile. This method can improve the accuracy of the  
400 existing forecaster by providing useful covariates. In Chapter 6, we give a conclusion to  
401 these two studies and provide future work on them.

# Chapter 2

402

## Preliminaries

403

In this chapter, we provide background on time series, with a focus on distance measures 404  
and classification, particularly the ridge classifier, which is used in the ROCKET-based 405  
classifiers for time series classification. The remaining preliminary knowledge will be 406  
provided in the corresponding chapters. Section 2.1 gives an overview of the existing 407  
distance measures used in the evaluation in Chapter 4. Section 2.2 reviews the additional 408  
knowledge about the classifiers used in Chapter 3. We start with the definition of a time 409  
series. 410

### 2.1 Distance Measures

411

A general form of a time series  $T$  is an ordered pair of  $n$  real-valued variables,  $T = 412$   
 $(b_1, c_1), (b_2, c_2), \dots, (b_n, c_n)$ , where  $b_i$  is the behavioral attribute and  $c_i$  is the contextual 413  
attribute, where  $1 \leq i \leq n$ .  $c_i$  refers to the time stamp at which the measurement  $b_i$  414  
is taken. Since the measurements are always taken in a uniform manner,  $t_i$  is simply 415  
incrementing from 1 to  $n$  uniformly. Hence, we can represent a time series more concisely 416  
as  $T = t_1, t_2, \dots, t_n$ , where  $t_i = b_i$ . 417

We may be interested not only in the entire time series but also in a segment of it, 418  
called a subsequence. A subsequence  $T(i : j)$  of a time series  $T$  is a shorter time series, 419  
which is a contiguous subset of time points in  $T$ , that starts from position  $i$  and ends at 420  
position  $j$ . Formally,  $T(i : j) = t_i, t_{i+1}, \dots, t_j$ , where  $1 \leq i \leq j \leq n$ . We call  $T(1 : m)$  as 421  
the prefix of length  $m$  of  $T$ ,  $m$ -prefix in short. 422

To quantify the similarity between two time series, we need to define a distance 423  
measure, also known as a similarity measure, between them. Many distance measures 424  
have been proposed in the literature. Among them, the most established measures are 425  
undoubtedly Euclidean Distance (ED) and Dynamic Time Warping (DTW). They are 426  
representatives of the two board classes of distance measures, namely “lock-step” and 427  
“elastic”. 428

429 **2.1.1 Euclidean Distance (ED)**

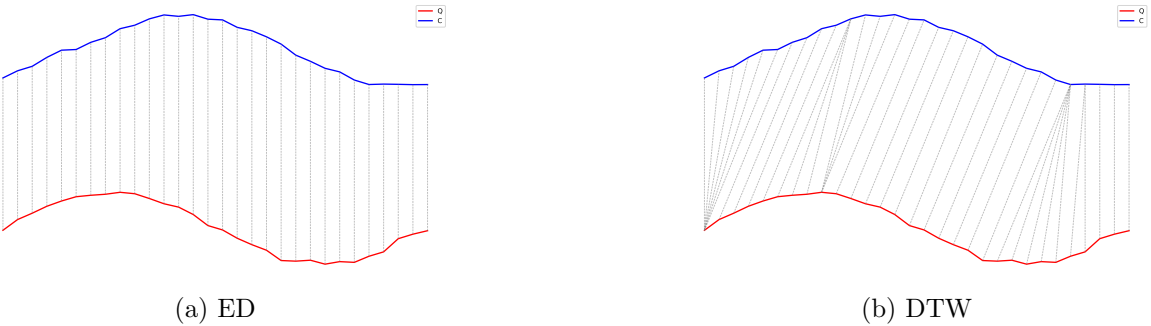


Figure 2.1: Alignments.

430 ED is a lock-step distance measure. Given two time series  $Q$  and  $C$  with the same  
 431 length  $n$ , it compares the time point  $q_i$  of  $Q$  with the time point  $c_i$  of  $C$  at the same time  
 432 (index). Note that, traditionally, lockstep distance measures require the two time series  
 433 to have the same length because of the one-to-one alignment, as shown in Figure 2.1.  
 434 However, in the setting of query by content, where it is always the case that  $|Q| < |C|$ ,  
 435 we can still apply a lock-step distance measure by either comparing  $Q$  with  $C(1 : |Q|)$   
 436 or padding  $Q$  using its last element to lengthen it to the same length of  $C$ . Minkowski  
 437 distance is a generalization of Euclidean distance. Minkowski distance is the  $L_p$ -norm of  
 438 the difference between the two time series  $X$  and  $Y$ , defined as:

$$D(X, Y) = \left( \sum_{i=1}^n |x_i - y_i|^p \right)^{\frac{1}{p}} \quad (2.1)$$

439 When  $p = 2$ , it corresponds to the Euclidean distance. When  $p = 1$ , it corresponds to  
 440 the Manhattan distance. When  $p = \infty$ , it corresponds to the Chebyshev distance. In our  
 441 studies, we focus on the Euclidean distance. Other lock-step distance measures include  
 442 Pearson correlation distance. It accounts for the linear association between the two time  
 443 series using the Pearson correlation coefficient. To note, there is another measure called  
 444 Edit Distance for strings. And Edit Distance is also sometimes abbreviated as ED in  
 445 string processing or bioinformatics. In this study, we focus on time series analysis and  
 446 use ED to denote Euclidean distance rather than edit distance.

447 **2.1.2 Dynamic Time Warping (DTW)**

448 Dynamic Time Warping is an elastic measure [2]. In contrast to lock-step distance mea-  
 449 sures, elastic distance measures allow one-to-many point matching, as shown in Figure 2.1.  
 450 The one-to-many point matching allows the elastic distance measures to warp in the time  
 451 axis (i.e., temporally) such that it can handle the local temporal distortions. While it

will be detailed in Chapter 4, it is briefly explained here. In short, it minimizes the cumulative distance between two time series, subject to constraints, by finding an optimal warping path  $W^*$  in a cost matrix, where  $W$  is the set of all possible paths and  $W^*$  is the optimal one. The constraints typically are (1) Boundary conditions, (2) Continuity, and (3) Monotonicity. Note that we can reduce pathological warping and accelerate computation by introducing a warping window. DTW with a warping window constraint is called constrained DTW (cDTW). Two famous windows are the Sakoe-Chiba band [2] and the Itakura parallelogram [3]. In the study, we focus on the Sakoe-Chiba band.

### 2.1.3 Derivative Dynamic Time Warping (DDTW)

The Derivative Dynamic Time Warping (DDTW) is a variant of DTW [4]. Instead of comparing original raw values, it compares two time series using their first-order derivatives, but with an approximation. In DTW, a point on a rising trend may be mapped to a point on a falling trend. It goes against our intuition. It can be solved by comparing their first-order derivatives, which encodes the slope information. The derivative  $T'$  of a time series  $T$  is computed approximately as follows.

$$t'_i = \frac{(t_i - t_{i-1}) + \frac{t_{i+1} - t_{i-1}}{2}}{2} \quad (2.2)$$

This estimate is simply the average of “the slope of the line through  $t_i$  and  $t_{i-1}$  (i.e., its left neighbor)” and “the slope of the line through  $t_{i-1}$  (i.e., its left neighbor) and  $t_{i+1}$  (i.e., its right neighbor)”. The  $1/2$  term in the second item of the numerator comes from the fact that the separation in time of the  $t_{i-1}$  and  $t_{i+1}$  is 2. Note that the estimate is not defined for the first and last elements of the time series in the above equation. In these boundary cases, we use the estimates of the second and penultimate (i.e., the second-to-last thing) as the estimates for the first and last elements, respectively.

### 2.1.4 Weighted Dynamic Time Warping (WDTW)

The Weighted Dynamic Time Warping (WDTW) is a variant of DTW [5]. It is a penalty-based DTW designed to prevent pathological paths. Recall that a warping window (e.g., Sakoe-Chiba band) is enforced on the cost matrix of DTW, such that some paths are excluded. Only the paths that reside entirely in the warping window are feasible. This constraint may be too strict. WDTW uses a softer way for the same purpose. Instead of using a window to forbid the alignment of  $x_i$  and  $y_j$  that are far away in time. WDTW weights the cost of such alignment by multiplying it by a modified logistic weight function (MLWF)  $\omega(k)$ , defined as follows.

$$\omega(k) = \frac{\omega_{\max}}{1 + \exp(-g \cdot (k - m_c))} \quad (2.3)$$

483 Where:

- 484 •  $k = |i - j|$ . It is the phase difference (i.e., distance on the time axis from the  
485 diagonal. The diagonal refers to the line where  $i = j$ .)
- 486 •  $\omega_{\max}$  is the desired upper bound for the weight parameter, which is suggested to be  
487 set to 1.
- 488 •  $m_c$  is the midpoint of a sequence.  $m_c = m/2$ .
- 489 •  $g$  is a constant that controls the level of penalization. It controls the curvature  
490 (slope) of the function.

491 Intuitively, if  $x_i$  and  $y_j$  are far apart temporally, it will have a larger weight to discourage  
492 their alignment and vice versa.

### 493 2.1.5 Weighted Derivative Dynamic Time Warping (WDDTW)

494 [5] also proposed the weighted version of DDTW. In brief, a weight is applied to the local  
495 cost function when computing DTW on the first derivative.

### 496 2.1.6 Shape Dynamic Time Warping (shapeDTW)

497 The Shape Dynamic Time Warping (shapeDTW) is a variant of DTW [6]. The main mod-  
498 ification to the original DTW is the way the local distance between points is computed.  
499 Recall that DTW compares single scalar points. shapeDTW compares local descriptors.  
500 The local descriptors are constructed using a sliding window on the original series, such  
501 that for each point  $x$ , a  $L$ -subsequence with  $x$  as the center is extracted to compute the  
502 higher-level feature of  $x$ .  $L$  is the user-given length of the subsequence to consider. By  
503 default, it is set to 15. There are several ways to construct such a descriptor. For exam-  
504 ple, a raw subsequence (i.e., a set of neighbor points surrounding the point of interest),  
505 Piecewise aggregate approximation (PAA) [7, 8], slope, derivative, HOG-1D [9].

506 Then, the distance between descriptors is calculated rather than between raw values.  
507 When a raw subsequence is chosen to construct the local descriptors, a common metric  
508 used for comparing two local descriptors is the Euclidean distance. In the evaluation, a  
509 raw subsequence is chosen to construct the local descriptors.

### 510 2.1.7 Amercing Dynamic Time Warping (ADTW)

511 The Amercing Dynamic Time Warping (WDTW) is a variant of DTW [10]. It is also  
512 designed to constrain the amount of warping, as in cDTW and WDTW. While cDTW  
513 imposes a hard window and WDTW uses multiplicative weights (i.e., MLWF), ADTW

introduces an additive penalty for non-diagonal alignment. The word “Amercing” means 514  
 “fining”. The non-diagonal alignments are required to pay the fines. Unlike WDTW, 515  
 which uses a multiplicative weight based on the position of the alignment, ADTW applies 516  
 an additive penalty  $\omega$  based on the action of warping. The non-diagonal alignments are 517  
 penalized. Formally, the recursive relation for ADTW is defined as: 518

$$D(i, j) = d(q_i, c_j) + \min \begin{cases} D(i - 1, j - 1), \\ D(i - 1, j) + \omega, \\ D(i, j - 1) + \omega \end{cases} \quad (2.4)$$

ADTW penalizes the last two alignment actions.  $\omega$  is a user-given hyperparameter. 519  
 It should be a non-negative scalar constant. In practice, it is defined through cross- 520  
 validation, which determines the optimal  $\omega$  by training on a subset of data or heuristic 521  
 search, which searches values in a user-given range. 522

To note, ADTW generalizes ED and DTW. If  $\omega = 0$ , no need to pay the fine for the 523  
 non-diagonal alignment, which reduces to DTW. If  $\omega \rightarrow \infty$ , the non-diagonal alignment 524  
 becomes prohibitive, and it reduces to ED. 525

## 2.2 Classification

In Chapter 3, we use ROCKET (RandOm Convolutional KErnel Transform) and its 527  
 variants, including MiniRocket, MultiRocket, and Hydra, as the time series classifiers on 528  
 the time series resulting from our encoding methods. Technically, they are not classifiers 529  
 in their own right but rather feature extractors. These features are also called summary 530  
 statistics. They are high-dimensional feature vectors that capture the characteristics of 531  
 the original time series. The summary statistics are then fed to the classifiers to output 532  
 the final classification results. 533

### 2.2.1 Ridge Classifier

The classifier that is usually chosen to work with ROCKET and its variants is a ridge 535  
 classifier. The main advantage of it is speed. ROCKET and its variants generate a large 536  
 number of features. 537

A ridge classifier is a wrapper that uses a ridge regression model as a routine to perform 538  
 classification. It first maps the categorical labels of targets into continuous numbers, does 539  
 the regression, and finally thresholds the numerical results from the regressor to obtain 540  
 the classification result. 541

542 Given a training dataset  $D = \{(x_i, y_i)\}_{i=1}^n$  with  $n$  instances, where  $x_i \in \mathbb{R}^P$  is the  
 543 feature vector with  $P$  dimensions and  $y_i \in \{+1, -1\}$  is its label, it minimize the following  
 544 optimization function.

$$\min_w \left( \sum_{i=1}^n (x_i^T w - y_i)^2 + \lambda \|w\|_2^2 \right) \quad (2.5)$$

545 Where  $\|w\|_2^2 = \sum_{j=1}^p w_j^2$  is the  $L_2$  norm of the weight vector and  $\lambda > 0$  control the  
 546 penalty. We explain the equation in brief. There are two terms inside the bracket. The  
 547 first term is simply the sum of the residual, same as the one in the least squares method.  
 548 The second term is called the  $L_2$  penalty and is used to introduce bias in the fit to avoid  
 549 overfitting. Hence,  $\lambda$  serves as a regularization hyperparameter between the trade-off  
 550 between bias and variance.

551 Since the above optimization function in a ridge classifier has a closed-form solution,  
 552 it can be solved using linear algebra rather than iterative optimization, as in logistic  
 553 regression. Besides, the generated features by the random kernels in ROCKET and its  
 554 variants are highly correlated. Ridge regularization, also known as the  $L_2$  norm, can  
 555 handle this case. Ridge regression shrinks regression coefficients toward zero by adding  
 556 an L2 penalty. It reduces model complexity and helps with multicollinearity.

# Chapter 3

557

## MTSCCleav: a Multivariate Time Series Classification (MTSC)-based Method for Predicting Human Dicer Cleavage Sites

558

559

560

561

MicroRNAs (miRNAs) are small non-coding RNAs (ncRNAs) that regulate gene expression at the post-transcriptional level, thereby playing essential roles in diverse biological processes. The biogenesis of miRNAs requires dicer to cleave at specific sites on the precursor miRNAs (pre-miRNAs). Several machine learning approaches have been proposed to predict whether an input sequence contains a cleavage site. However, they rely heavily on complex feature engineering or opaque deep neural networks. It results in a lack of generalizability and a long running time. There is a need for an alternative modeling paradigm that is accurate, fast, and simple.

562

563

564

565

566

567

568

569

We proposed a novel approach to frame the task as a multivariate time series classification problem. Nine encoding methods have been proposed to convert the sequence and the predicted secondary structure into a time series. We also leveraged the probabilities of the base pairs in the predicted secondary structure. Computational experiments demonstrate that our proposed method can achieve better or comparable results in terms of using a simpler, more intuitive model and less computational time. It achieves 3.7X to 28.8X speedup. Through perturbation experiments, we found that regions close to the center of pre-miRNAs are essential for predicting human dicer cleavage sites.

570

571

572

573

574

575

576

577

By transforming the RNA sequence and its secondary structure information into a time series and utilizing simple, state-of-the-art time series classifiers, we achieved comparable or even superior performance in a simpler and faster manner.

578

579

580

Code is available at: <https://github.com/colemanyu/time-series-classification-cleavage>.

581

582

### 583 3.1 Background

584 One of the most important theories in molecular biology is the central dogma. It depicts  
585 the flow of genetic information [11, 12]. Proteins are the functional units. The information  
586 stored in DNA is used to create them. Genes (segments) in DNA are used as templates for  
587 messenger RNAs (mRNAs) synthesis. An mRNA acts as a set of instructions to assemble  
588 a chain of amino acids, which form a linear polypeptide. To become biologically active,  
589 this chain is folded into a specific 3D structure, a proper configuration that enables it to  
590 perform its desired functions. This folded polypeptide is called a functional protein, or  
591 simply a protein. This entire process closely resembles how a computer program runs on  
592 a machine. The source code does not function by itself. First, it is translated into an  
593 assembly code (a lower-level, less human-readable form) and then into an executable file  
594 that can actually perform the intended tasks [13].

595 These mRNAs are called “coding RNAs” because they code for proteins. There are  
596 other genes in which the final product is the RNA molecule itself. They are called  
597 non-coding RNAs (ncRNAs). Two types of small ncRNAs are particularly important.  
598 They are microRNAs (miRNAs) and small interfering RNAs (siRNAs). Their discovery  
599 was recognized with the 2006 Nobel Prize in Physiology or Medicine<sup>1</sup>, awarded for work  
600 completed only eight years prior [11].

601 In this study, we focus on miRNAs. An miRNA can regulate the expression of several  
602 proteins. Hence, understanding the biogenesis of miRNAs is of great value. It involves  
603 the processing of primary miRNAs (pri-miRNAs). RNAs are 3D molecules. However, it  
604 is hard to measure the 3D structure (tertiary structure) from the experiment and predict  
605 it from 1D sequence. We can understand their properties by analyzing their 1D sequence  
606 or 2D structure, known as secondary structure. RNA sequence is easily obtained through  
607 sequencing. The sequence and its predicted secondary structure of a pri-miRNA “hsa-  
608 let-7a-1” is shown in Figure 3.1.

609 Recall that a pri-miRNA contains a hairpin loop, also called a stem loop. A mi-  
610 croprocessor complex comprising Drosa and DCGR8 cleaves the pri-miRNA to form a  
611 precursor miRNA (pre-miRNA) inside the nucleus. The stem-loop is still preserved, but  
612 the two arms become shorter. After that, the pri-miRNA is transported by Exportin 5  
613 from the nucleus to the cytoplasm. It is further cleaved by an enzyme called dicer [14].  
614 Dicer cleaves the stem-loop from the two arms at the two cleavage sites, shown as the two  
615 scissors in Figure 3.1. The stem-loop is removed. It results in a short double-stranded  
616 miRNA molecule, known as an miRNA duplex, which consists of the 5p strand and the

---

<sup>1</sup>The Nobel Prize in Physiology or Medicine 2006 - NobelPrize.org:  
<https://www.nobelprize.org/prizes/medicine/2006/summary/> (Accessed on: 2025-06-13).

<sup>2</sup>Its miRBase entry: <https://mirbase.org/hairpin/MI0000060>. (Accessed on: 2025-06-12).

<sup>3</sup>RNAfold web server: <http://rna.tbi.univie.ac.at/cgi-bin/RNAWebSuite/RNAfold.cgi>. (Accessed on: 2025-06-12). The figure is viewed in “forna”. This view option can be chosen on the website.

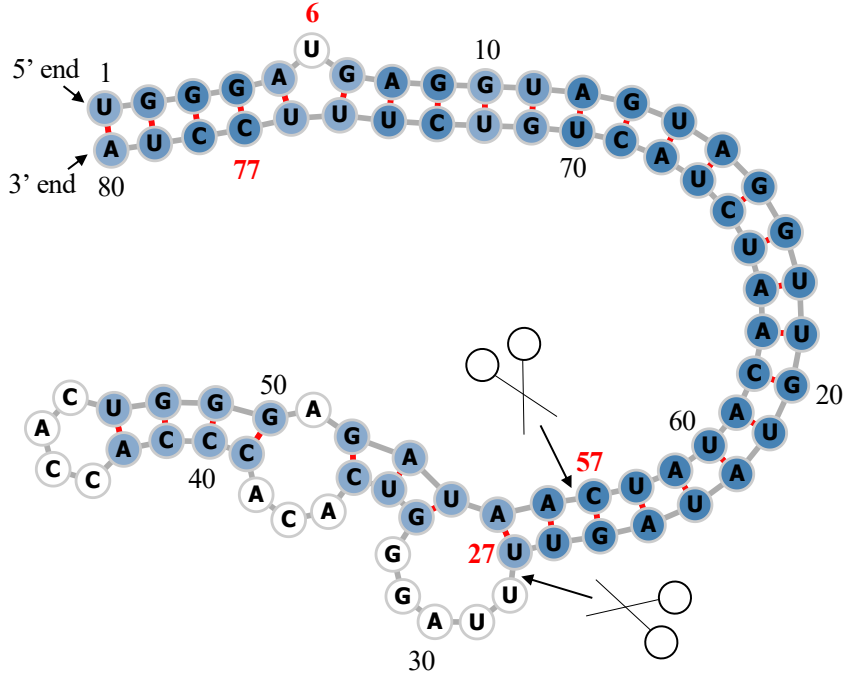


Figure 3.1: Predicted secondary structure of the sequence  $S$  of pri-miRNA “hsa-let-7a-1”<sup>2</sup>. Experimental evidence suggests that the two deviated mature miRNAs are  $UGA \cdots GUU$  and  $CUA \cdots UUC$ . They are  $S(6 : 27)$  and  $S(57 : 77)$  (Both ends are inclusive.). The ends are highlighted in **bold**. Since  $S(6 : 27)$  ( $S(57 : 77)$ ) is near the 5' (3') end, we call it “5p (3p) mature miRNA”. The two scissors indicate the two cleavage sites. The color intensity of the nodes reflects their base-pair probability in this predicted secondary structure. The deeper the color, the higher the probability. The unpaired nodes are uncolored. The raw figure is generated by RNAfold web server<sup>3</sup>.

3p strand<sup>4</sup>. These molecules may be subjected to additional trimming. The miRNA duplex is loaded into an RNA-induced silencing complex (RISC). RISC unwinds the duplex and tends to retain the strand with the less stable 5' end as the guide strand. The other strand is called the passenger strand. The retained strand guides the RISC to silence the target mRNA. Note that both strands can become the guide strand.

Dicer plays an important role in the biogenesis of miRNAs. It is reasonable to argue that the structure of the pre-miRNAs informs dicer about the cleavage process. It would be of great benefit to understand how dicer selects cleavage sites from the neighborhood information near the cleavage sites. Studies [15, 16, 17] revealed that the secondary structures are essential for cleavage site determination. Hence, to predict or classify whether a subsequence, extracted from the sequence of a pri-miRNA, contains a cleavage site, we can make use of both the sequence and secondary structure information. PHDcleav employed support vector machines (SVM), leveraging sequence and structure-based features for the classification [18]. LBSizeCleav improved upon it by considering the loop

<sup>4</sup>The 5p strand comes from the 5' arm while the 3p strand comes from the 3' arm. For the directionality, the 5p (3p) strand retains the original 5' (3') end of the pre-miRNA.

and bulge lengths [19]. [20] proposed an ensemble learning approach, using a gradient boosting machine for better accuracy. [21] developed a deep learning model, namely DiCleave. This model used an autoencoder to learn the secondary structure embeddings of pre-miRNAs from all the species in the miRBase database and leveraged this information. All these methods begin with curated pre-miRNA sequences from the miRBase database. Their secondary structures are predicted. Patterns are extracted from the sequence and the secondary structure. They create the positive cleavage patterns by setting the cleavage sites at the middle of the patterns. The follow-up work of [21], which created the cleavage pattern by allowing cleavage sites to appear at any position within the pattern, instead of the middle only [22]. It created a much larger dataset. This increased dataset facilitates the learning of the deep learning method at the cost of increased running time. We utilized the original dataset setting [18, 19, 20, 21]. DiCleave is the current state-of-the-art (SOTA) for this problem with the original dataset setting.

These models suffer several limitations. They rely heavily on complicated feature engineering or opaque deep learning models [20, 21, 22]. It results in a lack of generalizability and a long running time. There is a need to design a simpler model so that it can be easily extended to other prediction tasks on RNA data. One way to analyze sequence data is to transform it into time series data. In response to this, we proposed a multivariate time series classification-based method. Our contributions are shown as follows.

1. To the best of our knowledge, we are the first to frame the prediction of the cleavage sites as a multivariate time series classification problem.
2. We introduced several encoding methods to convert RNA data to time series.
3. We proposed utilizing the base-pair probabilities in the predicted secondary structure for the prediction. To our surprise, this information has been ignored in the existing studies.
4. For computational efficiency, our method achieves a 3.7X to 28.8X speedup compared to the state-of-the-art (SOTA).
5. We conducted perturbation-based experiments. It shows that regions close to the cleavage sites are important for this problem. It is consistent with the existing study [20].

## 3.2 Methods

The overall pipeline of this study is summarized in Figure 3.2.

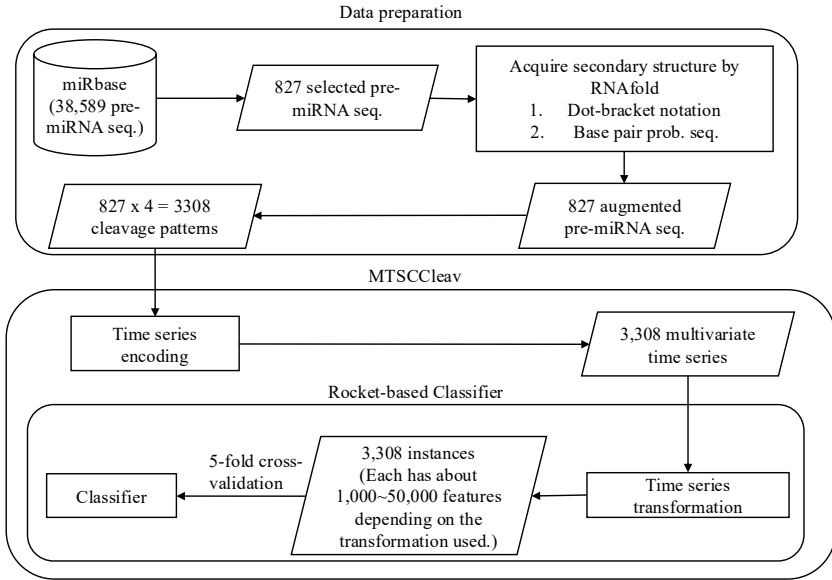


Figure 3.2: The overall pipeline of this study. Symbol notations: Cylinder - Dataset, Rectangle - Process, Parallelogram - Input / Output, Rounded Rectangle - Component.

### 3.2.1 Data Preparation

664

Accession	Name	Organism	Sequence	Mature miRNA 1	Mature miRNA 2
MI0000001	cel-let-7	<i>Caenorhabditis elegans</i>	<i>UACAC</i> ... <i>UUCGA</i>	cel-let-7-5p 17:38 experimental	cel-let-7-3p 60:81 experimental
<b>MI0000060</b>	hsa-let-7a-1	<i>Homo sapiens</i>	<i>UGGGA</i> ... <i>UCCUA</i>	hsa-let-7a-5p 6:27 experimental	hsa-let-7a-3p 57:77 experimental
MI0000114	hsa-mir-107	<i>Homo sapiens</i>	<i>CUCUC</i> ... <i>ACAGA</i>	hsa-miR-107 50:72 experimental	NA
MI0000238	hsa-mir-196a-1	<i>Homo sapiens</i>	<i>GUGAA</i> ... <i>UUCAC</i>	hsa-miR-196a-5p 7:28 experimental	hsa-miR-196a-1-3p 45:65 not experimental

Table 3.1: Selected representative records from miRBase. For the last two columns, the first line shows the name, the second line shows its location in the original sequence, and the third line indicates whether its existence has experimental evidence. The selected one is highlighted in **bold**.

We used miRBase database [23]<sup>5</sup>. The database comprises miRNA data from various organisms [24]. The database contains 38,589 miRNA records. Each record refers to an miRNA sequence, along with other properties such as name, accession, organism, and information on its derivative miRNA products. We are interested in pri-miRNA in humans. The derivative miRNA products are the mature miRNAs. The database also annotates the location of the mature miRNA within the original sequence and indicates whether its existence has experimental evidence.

665

666

667

668

669

670

671

<sup>5</sup>The website is [www.mirbase.org](http://www.mirbase.org), and the newest version of the database is Release 22.1 (Accessed on 2025-06-22).

672 Table 3.1 shows its four representative records. We first selected the records from  
 673 humans (*Homo sapiens*). It resulted in 1,917 records. To identify the actual locations of  
 674 the two cleavage sites in the pri-miRNA sequence supported by experimental evidence, we  
 675 selected records that have two mature miRNAs resulting from cleavage at the 5p arm and  
 676 the 3p arm, both of which have experimental support. Hence, only “MI0000060” (“hsa-  
 677 let-7a-1”) would be selected in the table. It would serve as our running example. Its whole  
 678 sequence is listed in Table 3.2. After the selection process, we selected 827 experimental  
 679 validated pre-miRNA sequences, each with its two mature miRNA products. This formed  
 680 our dataset.

Sequence	Secondary Structure (In Dot-bracket notation)
1 UGGGA <b>UGAGGUAGUAGGUUGUAUAGUU</b> 27 28 UUAGGGUCACACCCACCACUGGGAGAU 54 55 AA <b>CUAUACAAUCUACUGUCUUUC</b> CUA 80	1 (((((.((((((((((((( 27 28 UUAGGGUCACACCCACCACUGGGAGAU 54 55 ))))))))))))))))))))) 80
Base-pair probabilities sequence (the first 10 bases)	
1 (0.549, 0.946, 0.987, 0.987, 0.904) 5 6 ( <b>0.000</b> , 0.841, 0.974, 0.981, 0.890) 10	

Table 3.2: The whole sequence of “hsa-let-7a-1” and its predicted secondary structure by RNAfold. The corresponding positions of the two mature miRNAs and the probability of the unpaired “U” are highlighted in **bold**.

## 681 Augment the Dataset with Secondary Structure Information

682 We leveraged the predicted secondary structure of these sequences to enhance the ac-  
 683 curacy of the classification. Recall that a specific three-dimensional (3D) structure is  
 684 required for DNA, RNA, and protein to perform functions [25]. However, finding these  
 685 3D structures using experimental methods such as X-ray crystallography or nuclear mag-  
 686 netic resonance (NMR) is costly and time-consuming. Hence, prediction methods for such  
 687 3D structures are necessary and helpful for downstream analysis. However, predicting the  
 688 3D structures is challenging. One of the reasons is that there are some “nonconventional”  
 689 base-pair interactions (e.g., noncanonical and rare A-G) that allow an RNA sequence to  
 690 fold into a 3D structure, in addition to the (G, U) wobble pair, which is common and  
 691 functionally important in RNA secondary structures. It makes the search space for pre-  
 692 diction much larger than, in the 2D case, the secondary structure. The local structures  
 693 of the 3D structures, the secondary structures, only focus on the conventional base-pair  
 694 interactions [12]. Hence, predicting secondary structures is easier and faster. We em-  
 695 ployed RNAfold from the ViennaRNA Package<sup>6</sup> to predict the secondary structure for  
 696 a given pri-miRNA  $S$  [26]. RNAfold returns the secondary structure in the dot-bracket  
 697 notation and a matrix of base-pair probabilities. The matrix is a square matrix with the  
 698 side length  $|S|$ , where each entry  $m_{ij}$  is the probability of base  $s_i$  paired up with base  $s_j$ .

<sup>6</sup>The latest stable release is Version 2.7.0 (Accessed on 2025-06-22).

Dot-bracket notation is a way of representing the secondary structure of  $S$ . Open parentheses “(” (Close parentheses “)” ) indicates that the base is paired with a complementary base further (earlier) along in  $S$ . Dot “.” indicates that the base is unpaired. Equipped with the matrix, we can construct the base-pair probability sequence of  $S$ . The predicted secondary structure and the base-pair probability sequence of our running example are shown in Table 3.2.

## Extract Cleavage Patterns

The locations of the two mature miRNAs on the whole sequence indicate the probable locations of the two cleavage sites. The 5p cleavage site must be beyond and near the ending location of the 5p mature miRNA. We deemed the immediate bond next to the 5p mature miRNA’s ending position the 5p cleavage site, with the knowledge that the actual cleavage site may not be this immediate bond but rather the nearby bonds after it. The same applies to the 3p cleavage site. It is located at the immediate bond before the starting position of the 3p mature miRNA.

For each arm of each whole sequence, we extracted a 14-string<sup>7</sup> with the cleavage site located at the center of the string. The first 7 nt (nucleotide) before the center are highlighted in **bold**. In our running example, it would be “**UUAUAGUU**UUAGGU” for the 5p cleavage site and “**GAGAUAA**CUAUACA” for the 3p cleavage site. We refer to these 14-strings as cleavage patterns. We also generate non-cleavage patterns by selecting a 14-string with the center 6 nt away from the corresponding cleavage sites towards the corresponding mature miRNA [19, 20] for each arm of each whole sequence. So, in our running example, the 5p non-cleavage pattern would be “**AGGUUGU**AUAGUUU”. The 3p non-cleavage pattern would be “**ACUAUAC**AAUCUAC”.

In conclusion, for a given pri-miRNA sequence, we can generate two cleavage patterns and two non-cleavage patterns. We call these four patterns simply the “four strings” of a given pri-miRNA. We also call each string a strand. The “four strings” of our running example are listed in Table 3.3.

	5p cleav	5p non-cleav	3p cleav	3p non-cleav
Input strand	<b>UUAUAGUU</b> UUAGGU	<b>AGGUUGU</b> AUAGUUU	<b>GAGAUAA</b> CUAUACA	<b>ACUAUAC</b> AAUCUAC
Complementary strand	AUAUCAA_____UA	UCUAACAUAAUCAA_	C_CUGUUGAU AUGU	UGAUAUGUUGGAUG

Table 3.3: The first row shows the “four strings” of “hsa-let-7a-1”. Their complementary strands are shown in the second row. As a whole, they are referred to as the “eight strings”.

We can construct the complementary strand of each of the strands in the “four strings” by finding the corresponding paired base for each of the bases in the input strand by considering the secondary structure information. We use “\_” to denote the unpaired base

<sup>7</sup>String with length = 14.

in the complementary strand. For example, in Figure 3.1, “UUAGG” in the 5p cleavage pattern is unpaired, while other bases pair with some bases, the resulting complementary strand is “AUAUCAA\_\_\_\_UA”. There is a loop/budge there. We refer to the “four strings” and the four complementary strands together as the “eight strings” of the input pre-miRNA. It is also shown in Table 3.3.

### 3.2.2 Time Series Encoding

A *time series*  $T = t_1, t_2, \dots, t_n$  is a sequence of real-valued numbers<sup>8</sup>. A short contiguous region of  $T$  is called a subsequence. A *subsequence*  $T(i : j) = t_i, t_{i+1}, \dots, t_j$  of a time series  $T$  is a shorter time series that starts from position  $i$  and ends at position  $j$ , where  $i < j$ .

Strings and time series are temporal sequences. The difference between strings and time series lies in their behavioral attributes [27]. For strings, an entry is a letter from a predefined set called the *alphabet*. For example, the alphabet is  $\{A, C, G, T\}$  in the DNA string, while  $\{A, C, G, U\}$  in the RNA string. For time series, an entry is a real number. Unlike real numbers, there is no ordering in the alphabet unless some external domain knowledge is introduced.

The study of applying signal processing techniques to genomic data is called “Genomic Signal Processing” (GSP) [28, 29]. In the field of GSP, the time series representations of DNA strings are referred to as DNA numeric representations (DNR). Many DNRs have been proposed. We noted that DNA strings and RNA strings are equivalent from a computational standpoint. Many transformation methods designed for DNA can be applied to RNA by simply substituting  $T$  with  $U$ . We present nine encoding methods. The relationship among them is shown in Figure 3.3.

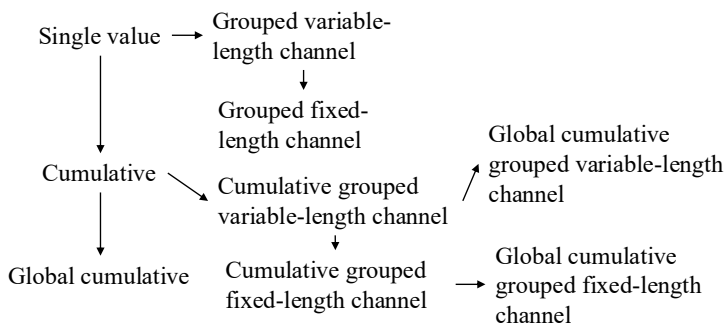


Figure 3.3: Relationship of the proposed encoding methods.

#### Single Value versus Cumulative

One of the simple, if not the simplest, encoding is to map the letters into numbers. Domain knowledge can be utilized. This approach is called the “Single value map-

<sup>8</sup>Unless otherwise specified, we denote entries of a time series (e.g.,  $T$ ) using the corresponding lowercase letter (e.g.,  $t$ ).

ping” [30, 31, 32, 33, 28]. One single value is assigned to each of the letters. [34] employed the atomic number of each nucleotide as the transformed values, where  $\{G = 78, A = 70, C = 58, T = 66\}$ . [35] used electron-ion interaction potential representation (EIIP) as such value, where  $\{G = 0.0806, A = 0.1260, C = 0.1340, T = 0.1335\}$ . Our goal is to transform the input strand and its complementary strand into time series, aiming to capture the information contained in these sequences and the secondary structure implied by them. We employed the following reasoning to assign the value:

1. We employ the complementary property [36, 32] during encoding. Recall that in the base-pairing rules,  $G$  pairs with  $C$  to form three hydrogen bonds while  $A$  pairs with  $U^9$  to form two hydrogen bonds.  $G-C$  pairs are more stable than  $A-U$  pairs.  $G$  ( $U$ ) can be regarded as the “inverse” of  $C$  ( $A$ ). We can preserve these base-pairing rules in the encoding by assigning  $G$  ( $A$ ) and  $C$  ( $U$ ) opposite values.
2.  $G$  and  $A$  have a two-ring structure. They are purines.  $C$  and  $U$  have a single-ring structure. They are pyrimidines. Hence, we put  $G$  and  $A$  ( $C$  and  $U$ ) on the same side of the number line with zero in the middle.
3. The lower stability of  $A-U$  pairs promotes strand separation, thereby facilitating the unwinding of the miRNA duplex during RISC loading. Regions rich in  $A$  and  $U$  are thus more likely to undergo strand selection and cleavage events. We assigned  $A$  ( $U$ ) with a larger absolute value than  $G$  ( $C$ ) to reflect this functional relevance. It aims to highlight sequence regions with higher cleavage potential.

It results in our baseline transformation method, namely “Single value mapping” as shown in row 1 of Table 3.4.  $S$  is the input strand. When we encode  $S$  without incorporating the corresponding base-pair probability sequence  $P$ , we set  $p_i = 1$  for all the entries of  $P$ . We use the first ten nucleotides of the complementary strand of the 3p cleav of “hsa-let-7a-1”, as shown in Table 3.3 as  $S$  in the examples in Table 3.4.

With the assigned value to each nucleotide defined in single-value mapping, we can compute a cumulative sum of those values over time. It captures the aggregated signal by accumulating past events, allowing us to focus on the trend [37, 38]. We named this method as “Cumulative mapping”, shown in row 4 of Table 3.4.

## Grouped Variable-Length Channel versus Grouped Local-Length Channel

We can transform the input strand into a multivariate time series with two channels using grouped binary encoding, where nucleotides are grouped into  $(A, U)$  and  $(G, C)$ . It releases our third assumption that  $A$  ( $U$ ) has a larger absolute value than  $G$  ( $C$ ). We proposed two variations. The first one allows the output to be variable-length sequences

<sup>9</sup>In DNA,  $A$  pairs with  $T$ .

	Encoding	Algorithm	Example
1	Single value mapping [30, 31, 32, 33, 28]	$\text{for } i = 1 \text{ to }  S :$ $t_i = \begin{cases} 2 \cdot p_i & \text{if } s_i = A \\ 1 \cdot p_i & \text{if } s_i = G \\ -1 \cdot p_i & \text{if } s_i = C \\ -2 \cdot p_i & \text{if } s_i = U \\ 0 & \text{otherwise} \end{cases}$ return $T$	$S = C, -, C, U, G, U, U, G, A, U$ $P = 0.843, 0.000, 0.807, 0.807, 0.793,$ $0.914, 0.982, 1.000, 0.999, 0.999$ Without base-pair probability sequence: $T = -1, 0, -1, -2, 1, -2, -2, 1, 2, -2$ With base-pair probability sequence: $T = -0.843, 0.000, -0.807, -1.614,$ $0.793, -1.829, -1.963,$ $1.000, 1.999, -1.998$
2	Grouped variable-length channel mapping	$j = 1, k = 1$ $\text{for } i = 1 \text{ to }  S :$ $t_j^1 = \begin{cases} 1 \cdot p_i & \text{if } s_i = A \\ -1 \cdot p_i & \text{if } s_i = U \\ 0 & \text{otherwise} \end{cases}$ $t_k^2 = \begin{cases} 1 \cdot p_i & \text{if } s_i = G \\ -1 \cdot p_i & \text{if } s_i = C \\ \text{if } (s_i = G) \text{ or } (s_i = C): \\ \quad \text{increment } k \text{ by 1} \\ \text{else:} \\ \quad \text{increment } j \text{ by 1} \end{cases}$ return $T^1, T^2$	Without base-pair probability sequence: $T^1 = 0, -1, -1, -1, 1, -1$ $T^2 = -1, -1, 1, 1$ With base-pair probability sequence: $T^1 = 0.000, -0.807, -0.914, -0.982, 0.999, -0.999$ $T^2 = -0.843, -0.807, 0.793, 1.000$
3	Grouped fixed-length channel mapping	$\text{for } i = 1 \text{ to }  S :$ $t_i^1 = \begin{cases} 1 \cdot p_i & \text{if } s_i = A \\ -1 \cdot p_i & \text{if } s_i = U \\ 0 & \text{otherwise} \end{cases}$ $t_i^2 = \begin{cases} 1 \cdot p_i & \text{if } s_i = G \\ -1 \cdot p_i & \text{if } s_i = C \\ 0 & \text{otherwise} \end{cases}$ return $T^1, T^2$	Without base-pair probability sequence: $T^1 = 0, 0, -1, 0, -1, -1, 0, 1, -1$ $T^2 = -1, 0, -1, 0, 1, 0, 0, 1, 0, 0$ With base-pair probability sequence: $T^1 = 0.000, 0.000, 0.000, -0.807,$ $0.000, -0.914, -0.982,$ $0.000, 0.999, -0.9999$ $T^2 = -0.843, 0.000, -0.807, 0.000,$ $0.793, 0.000, 0.000,$ $1.000, 0.000, 0.000$
4	Cumulative mapping [37, 38]	$t_1 = 0$ $\text{for } i = 1 \text{ to }  S :$ $t_{i+1} = \begin{cases} t_i + 2 \cdot p_i & \text{if } s_i = A \\ t_i + 1 \cdot p_i & \text{if } s_i = G \\ t_i - 1 \cdot p_i & \text{if } s_i = C \\ t_i - 2 \cdot p_i & \text{if } s_i = U \\ t_i & \text{otherwise} \end{cases}$ return $T //  T  =  S  + 1$	Without base-pair probability sequence: $T = 0, -1, -1, -2, -4, -3, -5, -7, -6, -4, -6$ With base-pair probability sequence: $T = 0.000, -0.843, -0.843, -1.650,$ $-3.265, -2.471, -4.300, -6.263,$ $-5.264, -3.265, -5.263$
5	Cumulative grouped variable-length channel mapping	$t_1^1 = 0, t_1^2 = 0$ $j = 1, k = 1$ $\text{for } i = 1 \text{ to }  S :$ $t_{j+1}^1 = \begin{cases} t_j^1 + 1 \cdot p_i & \text{if } s_i = A \\ t_j^1 - 1 \cdot p_i & \text{if } s_i = U \\ t_j^1 & \text{if } s_i = - \end{cases}$ $t_{k+1}^2 = \begin{cases} t_k^2 + 1 \cdot p_i & \text{if } s_i = G \\ t_k^2 - 1 \cdot p_i & \text{if } s_i = C \\ t_k^2 & \text{otherwise} \end{cases}$ $\text{if } (s_i = G) \text{ or } (s_i = C):$ $\quad \text{increment } k \text{ by 1}$ $\text{else:}$ $\quad \text{increment } j \text{ by 1}$ return $T^1, T^2$	Without base-pair probability sequence: $T^1 = 0, -1, -2, -3, -2, -3$ $T^2 = 0, -1, -2, -1, 0$ With base-pair probability sequence: $T^1 = 0.000, -0.807, -1.722,$ $-2.703, -1.704, -2.703$ $T^2 = 0.000, -0.843, -1.650,$ $-0.857, 0.143$
6	Cumulative grouped fixed-length channel mapping	$t_1^1 = 0, t_1^2 = 0$ $\text{for } i = 1 \text{ to }  S :$ $t_{i+1}^1 = \begin{cases} t_i^1 + 1 \cdot p_i & \text{if } s_i = A \\ t_i^1 - 1 \cdot p_i & \text{if } s_i = U \\ t_i^1 & \text{otherwise} \end{cases}$ $t_{i+1}^2 = \begin{cases} t_i^2 + 1 \cdot p_i & \text{if } s_i = G \\ t_i^2 - 1 \cdot p_i & \text{if } s_i = C \\ t_i^2 & \text{otherwise} \end{cases}$ return $T^1, T^2 //  T^1  =  T^2  =  S  + 1$	Without base-pair probability sequence: $T^1 = 0, 0, 0, -1, -1, -2, -3, -2, -3$ $T^2 = 0, -1, -1, -2, -2, -1, -1, 0, 0, 0$ With base-pair probability sequence: $T^1 = 0.000, 0.000, 0.000, 0.000,$ $-0.807, -0.807, -1.722, -2.703,$ $-2.703, -1.704, -2.703$ $T^2 = 0.000, -0.843, -0.843, -1.650,$ $-1.650, -0.857, -0.857, -0.857,$ $0.143, 0.143, 0.143$

Table 3.4: Time series encoding.  $P$  is the corresponding base-pair probability sequence of  $S$ .  $p_i = 1$  if we encode  $S$  without incorporating base-pair probability sequence.

per channel, depending on group-specific occurrences. The second one always returns two resulting sequences of a fixed length. Two variations extended from single value mapping are shown in rows 2 and 3, while those extended from cumulative mapping are shown in rows 5 and 6 in Table 3.4. 788  
789  
790  
791

## Global Cumulative versus Local Cumulative 792

In cumulative mapping and its variations, we can choose where to start the accumulation. 793  
For a given subsequence  $S'$  of the whole sequence  $S$ , accumulation can start from the 794  
beginning of  $S$  even if only  $S'$  is used downstream. It can also begin just at the start 795  
of the  $S'$ . The first one preserves the global context. It can be useful when previous 796  
nucleotides (those before  $S'$ ) influence later interpretation. The second one focuses solely 797  
on local history in  $S'$ , ignoring global history. It is helpful if the previous nucleotides do 798  
not affect the chemical property of  $S'$ . 799

Consider  $T = 0, -1, \dots, -6$  of the input string  $S$  in “Cumulative mapping” in Table 3.4, 800  
which accumulates from 0.  $S$  is the suffix with length = 10 of the constructed complemen- 801  
tary strand of  $S(1 : 63)$  in Figure 3.1. If we start the accumulation from the first entry 802  
of the constructed complementary strand instead, it will yield a different result. Suppose 803  
that the last entry of the time series encoded in the cumulative mapping of the con- 804  
structed complementary strand is -8, the time series encoded in the “Global cumulative 805  
mapping” for  $S$  would accumulate from -8 instead of 0. The result is  $T = -8, -9, \dots, -14$ . 806  
Note that it has the same trend as the original  $T$ . This “Global cumulative” concept can 807  
be applied to every cumulative-based method, as shown in Figure 3.3. 808

## Incorporating Base-Pair Probabilities 809

We can incorporate the base-pair probabilities  $P$  in the encoding by thinking of it as the 810  
weight or confidence  $p_i$  in the value assignment of each nucleotide  $s_i$ . It is implemented 811  
by multiplying the base-pair probability  $p_i$  of the nucleotide  $s_i$  with the assigned value of 812  
the kind of nucleotide of  $s_i$  during encoding, as shown in Table 3.4. 813

## Transforming the Secondary Structure into a Time Series 814

We can transform the secondary structure in the dot-bracket notation into a time series 815  
by “Single value mapping”, where “(” maps to 1, “.” maps to 0, and “)” maps to -1. 816

### 3.2.3 Time Series Classification 817

In univariate time series classification, an instance in the dataset consists of a time series 818  
 $x = x_1, x_2, \dots, x_m$  with  $m$  observations and a discrete class label  $y$ , which takes  $c$  possible 819

values [39, 40]. If  $c = 2$ , we refer to binary classification. If  $c > 2$ , we refer to multi-class classification. In multivariate time series classification, the time series is not a single sequence but a list of sequences. Each sequence is called a channel. There are many classifiers defined for time series data, including distance-based, feature-based, interval-based, shapelet-based, dictionary-based, convolution-based, and deep learning-based classifiers. Additionally, two or more of the above approaches can be combined, resulting in hybrid approaches [1, 40, 39]. We employed convolution-based classifiers due to their simplicity and accuracy.

## Convolution-Based Classifiers

Convolution-based classifiers first use randomly parameterized kernels to perform convolutions on the original time series  $T$ . A kernel is referred to as parameterized because its behavior is governed by a set of parameters, which will be discussed in detail later. Convolution is an operation to transform  $T$  to another time series  $M$ , where  $M$  is called the activation map. Its entry  $M_i$  is calculated by applying a kernel  $\omega$  with length  $l$  to  $T$  at position  $i$ , defined as follows:

$$M_i = T(i : i + l - 1) * \omega = \sum_{j=0}^{l-1} t_{i+j} \cdot \omega_{1+j}$$

To note,  $|T(i : i + l - 1)| = |\omega| = l$ . Entries  $M_i$ 's are calculated by sliding  $\omega$  across  $T$  and computing a dot product. Additionally, although the original paper [41] used the term “convolution” to refer to the above operation, “cross-correlation” may be a more suitable term for this operation. Recall  $T$  with length  $m$  has  $(m - l + 1)$  sliding windows of length  $l$ , given that the increment is  $1^{10}$ , which defines the length of  $M$ .

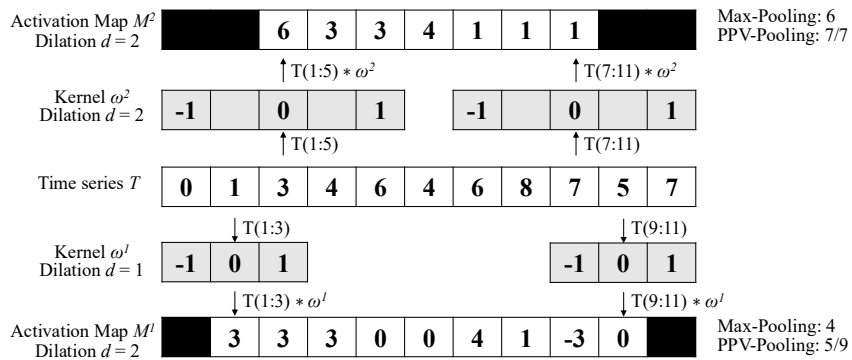


Figure 3.4: Features generation in the transformation

Figure 3.4 shows two kernels  $\omega^1$  and  $\omega^2$  with lengths 3 and 5, respectively. Each of which performs a convolution with  $T$  and returns two activation maps,  $M^1$  and  $M^2$ ,

<sup>10</sup>One step to the right per time.

respectively. For example,  $M_1^1 = T(1 : 3) * \omega^1 = 3$ . By sliding  $\omega^1$  one time stamp at a time, an activation map  $M^1$  with length  $= (m - l + 1) = 11 - 3 + 1 = 9$  is obtained. Then, pooling operations, such as the maximum (MAX) and proportion of positive values (PPV), are applied on  $M^1$  to derive the summary features. In Figure 3.4, MAX and PPV are applied on  $M^1$  and  $M^2$ . The summary features of  $M^1$  are 4 and  $5/9$ , which correspond to MAX and PPV, respectively. Dilation refers to a method that enables a kernel to cover a larger portion by creating empty spaces between entries in the kernel. The dilation  $d$  of  $\omega^2$  is 2. It introduces a gap of 1 in every two values of  $\omega^2$ .

The most popular convolution-based approach is the Random Convolutional Kernel Transform (ROCKET) [41]. It generates a large number of randomly parameterized kernels, ranging from thousands to tens of thousands. The kernel's parameters include length, weights (the entries inside the kernel), bias (the value added to the result of the convolution operation), and dilation. Additionally, padding can be applied to  $T$  at the start and end, ensuring  $M$  has the same length as the input. To note,  $T$ ,  $M_1$ , and  $M_2$  in Figure 3.4 have different lengths. The summary statistics of the activation map are obtained through two pooling operations: MAX and PPV. Hence, for  $k$  kernels, the transformed data has  $2k$  features. The default value of  $k$  is 10,000.

There are two extensions of ROCKET. They are MiniROCKET [42] and MultiROCKET [43]. MiniROCKET removes unnecessary operations and many of the random components in the definition of kernels used by ROCKET. It speeds up Rocket by over an order of magnitude with no significant difference in accuracy, making the classifier almost deterministic. For example, the kernel length is fixed, and only two weight values are used. Only PPV is used for the summary statistics. MultiROCKET is extended from MiniROCKET. The main improvement of it is to extract features from first-order differences as defined in Table 3.5 and add three new pooling operations [43]. The three added operations are mean of positive values (MPV), mean of indices of positive values (MIPV) and longest stretch of positive values (LSPV).

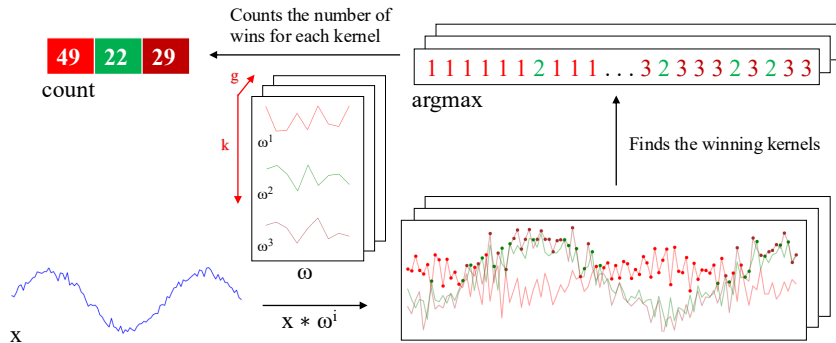


Figure 3.5: Convolutions of HYDRA for each input time series with a set of random kernels  $w$ , organized into  $g$  groups with  $k$  kernels each.

869 The HYbrid Dictionary-ROCKET Architecture (Hydra) combines dictionary-based  
870 and convolution-based models [44]. Similar to ROCKET-based classifiers, it uses random  
871 kernels to extract features from the input time series. But it groups the kernels into  $g$   
872 groups of  $k$  kernels each, as shown in Figure 3.5. Each time series is passed through  
873 all the groups. For each group of kernels, we slide them across  $T$  and compute the dot  
874 product at each timestamp. Recall that the dot product of two input vectors ( $x$  and  
875  $w_i$ ) has the maximum value when the two vectors align in the same direction and the  
876 minimum value when they are oriented in opposite directions. We record the kernel  
877 that best matches the subsequence of  $T$  at each timestamp in each group (i.e., argmax).  
878 We refer to these kernels as the winning kernels. This results in a  $k$ -dimensional count  
879 vector for each of the  $g$  groups, where  $k = 3$  in Figure 3.5. This results in a total of  
880  $g \times k$  features, with default values of  $g = 64$  and  $k = 8$ . It uses a total of  $k \times g = 512$   
881 kernels per dilation. In addition to recording the kernel with the maximum response,  
882 we can also record the kernel with the minimum response, knowing that this kernel will  
883 be the best match with the “inverted” subsequence of  $T$ . Hydra is applied to both the  
884 original time series and its first-order differences. Hydra generated approximately 1000  
885 features for each instance in our dataset. [44] found that it can improve the accuracy  
886 by concatenating features generated from Hydra with those from MultiRocket. This  
887 classifier is called MultiROCKET-Hydra.

888 These five classifiers share the same simple design pattern. It involves the overpro-  
889 duction of features followed by a selection strategy. A large number of features (1,000 ~  
890 50,000) are generated for each instance. The features are then fed into a simple linear  
891 classifier. It determines which features are most useful and returns the final classification  
892 result. A ridge classifier is used in this study. It is a linear classifier that extends ridge  
893 regression to classification tasks by applying a threshold to the predicted values. It uses  
894 L2 regularization to prevent overfitting. The regularization strength is selected by in-  
895 ternal cross-validation. A Ridge classifier is suggested for small datasets, as in our case,  
896 while a logistic regression classifier is suggested for large datasets [1].

897 While these five classifiers are often referred to as classifiers [1], they are technically  
898 time series transformation methods for generating features that are then fed to a down-  
899 stream classifier. The comparison of them is shown in Table 3.5. For MiniROCKET  
900 and MultiROCKET, the bias is determined from the convolution output, and the di-  
901 lation depends on the length of the input time series [42, 43]. The main differences  
902 among ROCKET-based classifiers lie in how the summary features are generated. The  
903 generation of the summary features depends on:

- 904 1. Kernels, which are defined based on the parameters, which consist of kernel length,  
905 kernel weights, bias, and dilation.

2. The way that padding applies to  $T$ , which leads to activation maps with different lengths. 906  
907
3. The pooling operations, which are used in extracting features on the activation map. 908  
909

	ROCKET	MiniROCKET	MultiROCKET	Hydra
kernel length	$\{7, 9, 11\}$	9	9	9
kernel weights	$\mathcal{N}(0, 1)$	$\{-1, 2\}$	$\{-1, 2\}$	$\mathcal{N}(0, 1)$
bias	$\mathcal{U}(0, 1)$	from output	from output	none
dilation	random	fixed (input-relative)	fixed (input-relative)	random
padding	random	fixed	fixed	always
pooling operations	MAX, PPV	PPV	PPV, MPV, MIPV, LSPV	Response per Kernel/Group
1 <sup>st</sup> order difference	no	no	yes	yes
feature vector size	20k	10k	50k	relative to input

Table 3.5: Comparison of rocket-based classifiers [1].  $\mathcal{N}(0, 1)$ : a standard normal distribution,  $\mathcal{U}(0, 1)$ : a uniform distribution between 0 and 1, 1<sup>st</sup> order difference:  $\Delta T = t_2 - t_1, t_3 - t_2, \dots, t_n - t_{n-1}$ .

### 3.2.4 Evaluation Metrics

To evaluate the performance of our time series-based classification (MTSC) model, we adopted five standard classification metrics. They are Accuracy (Acc), Specificity (Sp), Sensitivity (Sn), F1 score (F1), and Matthews Correlation Coefficient (MCC) [45]. 910  
911  
912  
913

$$Acc = \frac{TP + TN}{TP + TN + FP + FN}$$

$$Sp = \frac{TN}{TN + FP}$$

$$Sn = \frac{TP}{TP + FN}$$

$$F1 = \frac{2 \times TP}{2 \times TP + FP + FN}$$

$$MCC = \frac{TP \times TN - FP \times FN}{\sqrt{(TP + FP)(TP + FN)(TN + FP)(TN + FN)}}$$

where TP, TN, FP, and FN are the number of true positives, true negatives, false positives, and false negatives, respectively. 914  
915

To extend a binary metric to multi-class problems, we can treat the data as a collection of binary problems, one for each class. One class is treated as positive while the other classes are treated as negative. Then, the multi-class metrics can be obtained by averaging binary metric calculations across the set of classes. There are different ways of doing the averaging. Here, we adopted a macro-averaging approach. It treats each class equally and calculates the mean of the binary metrics. To use  $MCC$  in the multiclass case, it 916  
917  
918  
919  
920  
921

922 can be defined in terms of a confusion matrix  $C$  for  $K$  classes, where  $C_{i,j}$  is the number  
923 of observations that are actually in class  $i$  and predicted to be in class  $j$  [46].

$$MCC_{multi} = \frac{c \times s - \sum_k^K p_k \times t_k}{\sqrt{(s^2 - \sum_k^K p_k^2) \times (s^2 - \sum_k^K t_k^2)}}$$

924 where  $t_k = \sum_i^K C_{i,k}$  (denoting the number of times class  $k$  actually occurred),  $p_k =$   
925  $\sum_i^K C_{k,i}$  (denoting the number of times class  $k$  was predicted),  $c = \sum_k^K C_{k,k}$  (denoting  
926 the total number of samples correctly predicted) and  $s = \sum_i^K \sum_j^K C_{i,j}$  (denoting the total  
927 number of samples).

### 928 3.3 Results

929 The code implementing our method is available at <https://github.com/colemanyu/time-series-classification-cleavage>. The dataset of this study is available at  
930 <https://www.mirbase.org>.

932 In all experiments, the models were trained and tested using 5-fold cross-validation.  
933 We retrieved 827 empirically validated sequences of pre-miRNAs. There are 5p arm  
934 and 3p arm in each sequence. For each arm, we defined a cleavage pattern and a non-  
935 cleavage pattern. Three datasets, namely “5p arm”, “3p arm”, and “multi-class” were  
936 constructed by these patterns. We refer to the cleavage patterns as positive instances  
937 and the non-cleavage patterns as negative instances. The 5p arm dataset comprises 827  
938 positive instances and an equal number of negative instances. The 5p arm and 3p arm  
939 datasets are binary-class datasets. The multi-class dataset comprises all patterns from  
940 both the 5p arm and the 3p arm. There are 827 “5p” instances<sup>11</sup>, 827 “3p” instances,  
941 and 1,654 negative instances.

942 For every fold in 5-fold cross-validation, the dataset was divided into a training set  
943 and a test set with sizes of 80% and 20% of the whole dataset, respectively. We kept the  
944 class distribution approximately the same in each fold, since it is in the original dataset.  
945 In each fold derived from the 5p arm and 3p arm datasets, the training set has a size of  
946 1,323, and the test set has a size of 331. In each fold derived from the multi-class dataset,  
947 the training set has a size of 2,262, and the test set has a size of 662. We reported the  
948 average of the five classification metrics.

949 The ROCKET-based classifiers require all channels in the multivariate time series to  
950 have equal length. We applied padding to the shorter channels using the constant value  
951 100, which does not appear in the original time series. It ensures the padding does not  
952 introduce ambiguity or interfere with the semantic meaning of the encoded nucleotide  
953 signals.

---

<sup>11</sup>Cleavage patterns from the 5p arm.

### 3.3.1 Channel Ablation Study

We utilized three types of data as the input features for each instance. They are (1) the RNA sequence, which consists of the primary strand and its complementary strand, (2) the secondary structure information, and (3) the base-pair probability sequence. To input the data into our time series-based classifiers, we converted them into multivariate time series. The primary strand and its complementary strand are each encoded into one or two channels, using the encoding methods in Table 3.4. For example, single value mapping encodes a strand in one channel, while grouped variable-length channel mapping encodes in two channels. The secondary structure information is converted into a univariate time series. The base-pair probability sequence is already in numerical form and does not require further transformation. It can be used either as a standalone channel or incorporated into the encoding of the complementary strand. We performed a channel ablation study to determine the most informative combination of the above channels.

We referred to the multivariate time series that consists of the channels from the RNA sequence only as the baseline setting. We added the other channels to this baseline. It leads to the following configurations (cfgs):

1. (cfg 1) Baseline: Time series derived only from the RNA sequence.
2. (cfg 2) Baseline + Secondary structure: Baseline + time series representation of the secondary structure.
3. (cfg 3) Baseline + Base-pair probability (Standalone): Baseline + the base-pair probability sequence as a standalone channel.
4. (cfg 4) Baseline + Base-Pair probability (Incorporated): Baseline with the base-pair probability sequence incorporated into the encoding of the complementary strand.

Classifier	5p arm					3p arm					multi-class					
	Acc	Sp	Sn	F1	MCC	Acc	Sp	Sn	F1	MCC	Acc	Sp	Sn	F1	MCC	
Baseline (cfg 1)	ROCKET	0.781	0.743	0.819	0.789	0.563	0.790	0.773	0.807	0.793	0.580	0.717	0.838	0.685	0.700	0.538
	MiniROCKET	0.755	0.728	0.782	0.762	0.512	0.788	0.781	0.794	0.789	0.576	0.685	0.823	0.653	0.662	0.486
	MultiROCKET	0.784	0.767	0.801	0.787	0.569	0.803	0.792	0.814	0.805	0.606	0.691	0.830	0.667	0.672	0.501
	Hydra	0.830	0.800	0.860	0.835	0.663	0.808	0.797	0.820	0.810	0.617	0.731	0.844	0.696	0.712	0.560
	MultiROCKET-Hydra	0.796	0.778	0.815	0.800	0.594	0.807	0.767	0.816	0.808	0.614	0.701	0.836	0.681	0.686	0.520
Baseline + Secondary Structure (cfg 2)	ROCKET	<b>0.847</b>	<b>0.832</b>	0.862	<b>0.849</b>	<b>0.695</b>	<b>0.855</b>	0.842	0.868	<b>0.857</b>	<b>0.711</b>	<b>0.836</b>	<b>0.907</b>	<b>0.828</b>	<b>0.833</b>	0.736
	MiniROCKET	0.825	0.807	0.843	0.827	0.652	0.822	0.802	0.843	0.826	0.646	0.823	0.900	0.812	0.818	0.715
	MultiROCKET	0.812	0.803	0.822	0.814	0.626	0.824	0.809	0.839	0.826	0.649	0.796	0.888	0.791	0.792	0.673
	Hydra	0.845	0.816	<b>0.873</b>	<b>0.849</b>	0.691	0.846	0.817	<b>0.874</b>	0.850	0.693	0.830	0.901	0.814	0.826	0.724
	MultiROCKET-Hydra	0.817	0.809	0.826	0.819	0.635	0.825	0.816	0.834	0.826	0.652	0.803	0.891	0.798	0.800	0.684
Baseline + Base-pair probability (Standalone) (cfg 3)	ROCKET	0.842	0.828	0.855	0.844	0.684	<b>0.855</b>	<b>0.856</b>	0.854	0.855	0.710	0.795	0.885	0.783	0.789	0.670
	MiniROCKET	0.817	0.820	0.814	0.816	0.634	0.836	0.834	0.838	0.836	0.673	0.772	0.872	0.757	0.764	0.632
	MultiROCKET	0.822	0.813	0.832	0.824	0.645	0.825	0.831	0.820	0.824	0.651	0.758	0.866	0.747	0.750	0.612
	Hydra	0.846	0.827	0.865	<b>0.849</b>	0.693	0.851	0.840	0.861	0.852	0.702	0.789	0.879	0.769	0.780	0.658
	MultiROCKET-Hydra	0.822	0.809	0.834	0.824	0.644	0.835	0.840	0.830	0.834	0.670	0.759	0.866	0.746	0.750	0.611
Baseline + Base-pair probability (Incorporated) (cfg 4)	ROCKET	0.799	0.771	0.827	0.805	0.600	0.809	0.786	0.832	0.813	0.619	0.737	0.850	0.712	0.724	0.573
	MiniROCKET	0.776	0.756	0.797	0.781	0.554	0.801	0.808	0.794	0.799	0.603	0.705	0.835	0.675	0.684	0.521
	MultiROCKET	0.814	0.801	0.828	0.817	0.630	0.816	0.812	0.820	0.816	0.634	0.726	0.848	0.706	0.712	0.556
	Hydra	0.822	0.787	0.857	0.828	0.647	0.834	0.828	0.840	0.835	0.669	0.759	0.862	0.734	0.746	0.608
	MultiROCKET-Hydra	0.814	0.802	0.820	0.817	0.629	0.820	0.825	0.816	0.819	0.642	0.736	0.853	0.717	0.723	<b>0.874</b>

Table 3.6: Channel ablation study. The best results are highlighted in **bold**.

977 We used single value mapping as the encoding method. Table 3.6 shows the result.  
 978 From the table, we can see that the addition of secondary structure, base-pair probability  
 979 as a standalone channel, and base-pair probability incorporated in the encoding of the  
 980 complementary strand can improve the performance. We plotted the critical difference  
 981 (CD) diagram as shown in Figure 3.6 to visualize Table 3.6 to make the performances  
 982 of different combinations more obvious. In CD diagrams, lower-ranked methods (toward  
 983 the right) are better. A horizontal bar connecting combinations indicates no statistically  
 984 significant difference.

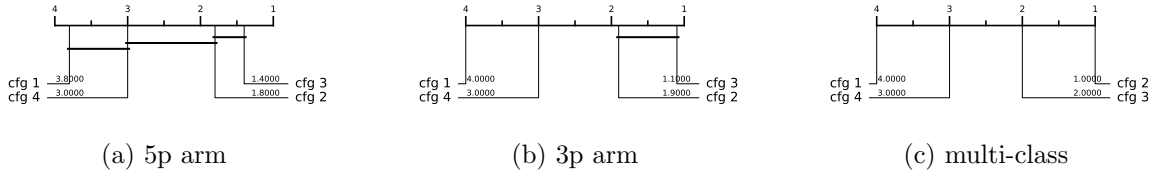


Figure 3.6: CD diagrams of channel ablation study.

985 From Figure 3.6, we can see that including time series derived from secondary struc-  
 986 ture information and base-pair probability as a separate channel can significantly improve  
 987 the performance of the classifiers. Incorporating the base-pair probability sequence in the  
 988 time series encoding of the complementary strand can also improve the classifier, but to  
 989 a minor degree compared to serving as a standalone channel. In our downstream analy-  
 990 sis, we adopted the combination of RNA sequence time series, secondary structure time  
 991 series, and base-pair probability time series as our multivariate time series input, with 4  
 992 to 6 channels, depending on the encoding used.

### 993 3.3.2 Predictive Performance

994 The experiment was conducted on three datasets: the 5p arm, the 3p arm, and the  
 995 multi-class datasets. Recall that we have nine encoding methods and five ROCKET-  
 996 based classifiers. It results in 45 combinations of encoding methods and classifiers.

997 The result is shown in Table 3.7. The best combination of encoding method and  
 998 classifier is shown in Table 3.8. For the 5p arm dataset, the best combination is “Global  
 999 Cumulative grouped fixed-length channel mapping + ROCKET”. For all five classifica-  
 1000 tion metrics, it outperforms the state-of-the-art (SOTA) method, DiCleave. For the 3p  
 1001 arm dataset, the best combination is “Global Cumulative grouped fixed-length channel  
 1002 mapping + ROCKET”. Out of the five classification metrics, it outperforms DiCleave,  
 1003 except in specificity. For the multi-class dataset, the best combination is “Global Cu-  
 1004 mulative grouped fixed-length channel mapping + ROCKET”. For all five classification  
 1005 metrics, it outperforms DiCleave. Note that for the 3p arm and the multi-class datasets,

	Classifier	5p arm					3p arm					multi-class				
		Acc	Sp	Sn	F1	MCC	Acc	Sp	Sn	F1	MCC	Acc	Sp	Sn	F1	MCC
Single value mapping (enc 1)	ROCKET	0.849	0.842	0.857	0.851	0.699	0.863	0.854	0.873	0.865	0.727	0.853	0.917	0.847	0.851	0.764
	MiniROCKET	0.823	0.809	0.837	0.825	0.647	0.823	0.828	0.817	0.822	0.647	0.835	0.906	0.828	0.833	0.735
	MultiROCKET	0.821	0.802	0.840	0.824	0.643	0.839	0.826	0.852	0.841	0.679	0.811	0.894	0.806	0.809	0.697
	Hydra	0.843	0.820	0.867	0.847	0.688	0.838	0.819	0.857	0.841	0.677	0.831	0.901	0.815	0.827	0.727
	MultiROCKET-Hydra	0.820	0.803	0.837	0.823	0.640	0.840	0.830	0.850	0.841	0.680	0.816	0.896	0.810	0.814	0.704
Grouped variable-length channel mapping (enc 2)	ROCKET	0.835	0.826	0.844	0.836	0.670	0.855	0.849	0.861	0.856	0.710	0.846	0.913	0.839	0.844	0.752
	MiniROCKET	0.843	0.833	0.853	0.844	0.686	0.831	0.821	0.842	0.833	0.663	0.837	0.907	0.828	0.834	0.737
	MultiROCKET	0.819	0.809	0.828	0.820	0.638	0.817	0.814	0.820	0.818	0.634	0.890	0.894	0.806	0.808	0.695
	Hydra	0.825	0.780	0.869	0.832	0.653	0.811	0.769	0.854	0.819	0.626	0.818	0.892	0.765	0.812	0.705
	MultiROCKET-Hydra	0.818	0.814	0.822	0.819	0.636	0.831	0.825	0.837	0.832	0.662	0.820	0.900	0.815	0.818	0.710
Grouped fixed-length channel mapping (enc 3)	ROCKET	0.851	0.843	0.859	0.852	0.702	0.863	0.850	0.875	0.864	0.726	0.849	0.915	0.843	0.847	0.757
	MiniROCKET	0.844	0.836	0.853	0.845	0.689	0.840	0.826	0.855	0.843	0.682	0.851	0.915	0.844	0.849	0.760
	MultiROCKET	0.831	0.815	0.848	0.834	0.663	0.824	0.813	0.836	0.826	0.649	0.811	0.896	0.808	0.808	0.698
	Hydra	0.848	0.816	0.880	0.853	0.699	0.862	0.839	0.884	0.864	0.724	0.843	0.908	0.837	0.839	0.746
	MultiROCKET-Hydra	0.836	0.813	0.859	0.839	0.672	0.833	0.820	0.845	0.835	0.665	0.828	0.905	0.824	0.826	0.725
Cumulative mapping (enc 4)	ROCKET	0.850	0.834	0.866	0.852	0.701	0.863	0.855	0.871	0.864	0.726	0.852	0.915	0.842	0.850	0.762
	MiniROCKET	0.840	0.821	0.860	0.843	0.682	0.840	0.837	0.844	0.841	0.682	0.843	0.911	0.835	0.840	0.747
	MultiROCKET	0.822	0.809	0.834	0.824	0.644	0.832	0.830	0.834	0.832	0.665	0.820	0.898	0.810	0.816	0.709
	Hydra	0.848	0.819	0.878	0.853	0.698	0.853	0.856	0.869	0.855	0.705	0.845	0.910	0.830	0.841	0.749
	MultiROCKET-Hydra	0.824	0.811	0.856	0.825	0.647	0.838	0.833	0.843	0.839	0.677	0.821	0.898	0.810	0.817	0.711
Cumulative grouped variable-length channel mapping (enc 5)	ROCKET	0.843	0.821	0.866	0.847	0.688	0.856	0.840	0.871	0.857	0.712	0.855	0.916	0.843	0.851	0.766
	MiniROCKET	0.845	0.826	0.865	0.848	0.691	0.836	0.833	0.838	0.836	0.672	0.840	0.909	0.833	0.838	0.742
	MultiROCKET	0.826	0.814	0.838	0.828	0.653	0.815	0.820	0.810	0.814	0.631	0.826	0.902	0.820	0.824	0.721
	Hydra	0.850	0.819	0.880	0.854	0.701	0.834	0.807	0.861	0.838	0.669	0.833	0.903	0.818	0.829	0.731
	MultiROCKET-Hydra	0.824	0.810	0.838	0.826	0.649	0.833	0.833	0.833	0.833	0.666	0.830	0.903	0.821	0.827	0.726
Cumulative grouped fixed-length channel mapping (enc 6)	ROCKET	0.856	0.836	0.876	0.858	0.712	0.870	0.861	0.879	0.871	0.741	0.863	0.921	0.852	0.860	0.780
	MiniROCKET	0.856	0.837	0.874	0.858	0.712	0.842	0.839	0.845	0.843	0.685	0.845	0.912	0.837	0.843	0.751
	MultiROCKET	0.820	0.802	0.839	0.824	0.642	0.798	0.798	0.798	0.798	0.597	0.809	0.894	0.806	0.807	0.694
	Hydra	0.850	0.814	0.885	0.855	0.701	0.855	0.840	0.869	0.857	0.711	0.847	0.910	0.831	0.843	0.752
	MultiROCKET-Hydra	0.820	0.801	0.839	0.823	0.641	0.807	0.813	0.802	0.806	0.615	0.821	0.900	0.817	0.819	0.713
Global Cumulative mapping (enc 7)	ROCKET	0.850	0.834	0.866	0.852	0.701	0.863	0.855	0.871	0.864	0.726	0.852	0.915	0.842	0.850	0.762
	MiniROCKET	0.847	0.832	0.862	0.849	0.695	0.848	0.839	0.857	0.850	0.697	0.845	0.911	0.836	0.843	0.750
	MultiROCKET	0.827	0.819	0.834	0.828	0.653	0.847	0.842	0.853	0.848	0.695	0.825	0.901	0.817	0.822	0.718
	Hydra	0.851	0.821	0.880	0.855	0.703	0.861	0.848	0.874	0.863	0.722	0.847	0.911	0.834	0.844	0.753
	MultiROCKET-Hydra	0.829	0.823	0.834	0.830	0.658	0.843	0.838	0.849	0.844	0.688	0.832	0.905	0.823	0.829	0.730
Global Cumulative grouped variable-length channel mapping (enc 8)	ROCKET	0.840	0.814	0.867	0.844	0.682	0.853	0.838	0.867	0.854	0.706	0.856	0.917	0.845	0.853	0.768
	MiniROCKET	0.848	0.834	0.862	0.850	0.697	0.841	0.824	0.859	0.844	0.683	0.844	0.911	0.856	0.842	0.748
	MultiROCKET	0.834	0.828	0.839	0.834	0.668	0.831	0.821	0.842	0.833	0.663	0.828	0.904	0.823	0.826	0.724
	Hydra	0.857	0.821	0.894	0.862	0.717	0.822	0.786	0.857	0.828	0.645	0.826	0.898	0.806	0.820	0.717
	MultiROCKET-Hydra	0.837	0.834	0.839	0.837	0.674	0.834	0.827	0.840	0.835	0.668	0.835	0.907	0.828	0.832	0.734
Global Cumulative grouped fixed-length channel mapping (enc 9)	ROCKET	0.856	0.836	0.876	0.858	0.712	0.870	0.861	0.879	0.871	0.741	0.863	0.921	0.852	0.860	0.780
	MiniROCKET	0.857	0.845	0.870	0.859	0.715	0.840	0.821	0.859	0.843	0.681	0.844	0.911	0.837	0.842	0.749
	MultiROCKET	0.829	0.825	0.833	0.830	0.658	0.820	0.816	0.823	0.820	0.640	0.819	0.900	0.816	0.817	0.710
	Hydra	0.856	0.817	0.894	0.861	0.713	0.859	0.838	0.880	0.862	0.719	0.846	0.911	0.832	0.843	0.752
	MultiROCKET-Hydra	0.829	0.824	0.834	0.830	0.658	0.822	0.825	0.819	0.821	0.644	0.827	0.904	0.823	0.824	0.722

Table 3.7: Performance on the 45 combinations between encoding methods and the ROCKET-based classifiers. The best results are highlighted in **bold**.

the combination of “Cumulative grouped fixed-length channel mapping + ROKCET” 1006 also attains the best result. 1007



Figure 3.7: CD diagrams to compare different classifiers.

To summarize Table 3.7, we plot the CD diagrams for finding the best classifier, as shown in Figure 3.7, and the best encoding method, as shown in Figure 3.8. 1008 1009

Dataset	Methods	Acc	Sp	Sn	F1	MCC	Time (s)
5p arm	enc 9 + MiniROCKET	<b>0.857</b>	<b>0.845</b>	<b>0.870</b>	<b>0.859</b>	<b>0.715</b>	<b>0.787</b>
	DiCleave	0.818	0.790	0.846	0.822	0.653	21.249
3p arm	enc 9 + ROCKET	<b>0.870</b>	0.861	<b>0.879</b>	<b>0.871</b>	<b>0.741</b>	4.311
	enc 7 + MiniROCKET	0.848	0.839	0.857	0.850	0.697	<b>0.989</b>
	DiCleave	0.854	<b>0.891</b>	0.817	0.847	0.715	15.919
multi-class	enc 9 + ROCKET	<b>0.863</b>	<b>0.921</b>	<b>0.852</b>	<b>0.860</b>	<b>0.780</b>	12.208
	enc 3 + MiniROCKET	0.851	0.915	0.844	0.849	0.760	<b>4.550</b>
	DiCleave	0.820	0.895	0.804	0.815	0.710	131.151

Table 3.8: Comparative analysis between MTSCCleav with the best combination of the encoding method and classifier, with the SOTA, DiCleave, on the three datasets. The best results of using MiniROCKET have also been shown to compare the computational efficiency. The best results are highlighted in **bold**.

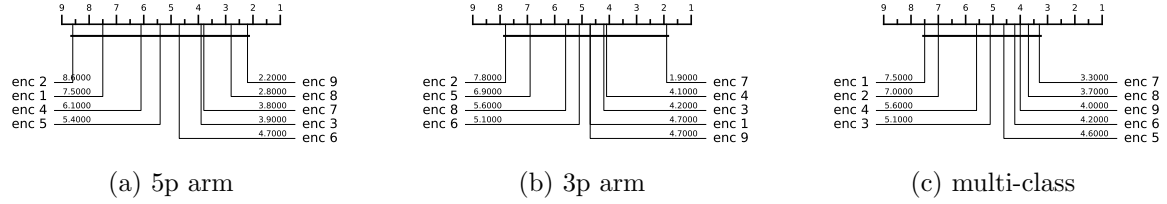


Figure 3.8: CD diagrams to compare different encoding methods.

### 3.3.3 Running Time Analysis

To compare the computational efficiency of MTSCCleav and DiCleave, we conducted a comparative analysis of their running times. For DiCleave, we employed the code from its supporting website<sup>12</sup>, without any modifications. All experiments were conducted on the same machine (a personal laptop equipped with an Apple M1 Pro chip and 16 GB of memory) and using the same splits of the training and test datasets under 5-fold cross-validation to ensure fairness. The reported running times are the averages of the five runs. The timing results were measured from the training phase to the return of the five classification metrics. The result is shown in Table 3.8. MiniROCKET is the most computationally efficient of the five rocket-based classifiers. We also included its best result, along with the corresponding encoding method, even though this combination may not be the best overall.

MTSCCleav demonstrated a significant advantage in computational efficiency, achieving an average 27.0X, 3.7X, and 10.7X speedup over DiCleave, for the 5p arm, 3p arm, and multi-class datasets, respectively. If we consider using the MiniROCKET in the case of 3p arm and multi-class datasets, it achieves 16.1X and 28.8X speedup. To note, in the

<sup>12</sup>

<https://github.com/MGuard0303/DiCleave> (Accessed on: 2025-07-13).

case of the 3p arm dataset, the performance of MiniROCKET is only slightly worse than 1026  
DiCleave. In the case of the multi-class dataset, even the performance of MiniROCKET 1027  
is better than DiCleave. DiCleave is a deep learning-based method that requires sub- 1028  
stantial time for model inference, while MTSCleav leverages efficient ROCKET-based 1029  
classifiers. This significant reduction in runtime makes MTSCcleav more suitable for 1030  
large-scale data and real-time applications. 1031

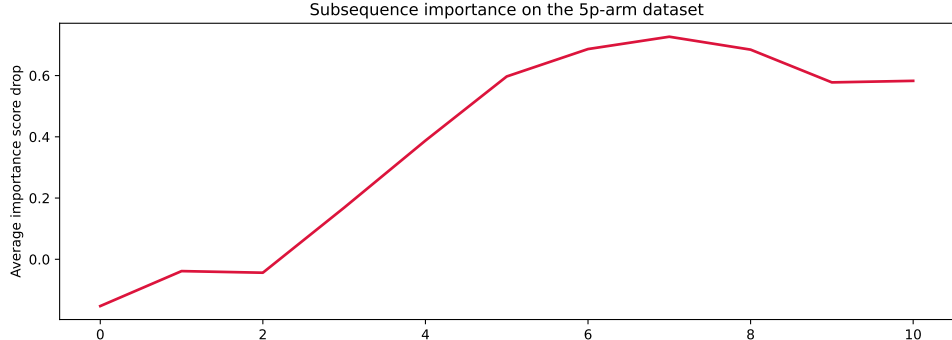
### 3.3.4 Subsequence Importance

To evaluate the sensitivity of MTSCcleav to subsequences of the input, we conducted a 1033  
perturbation experiment to evaluate the importance of subsequences based on masking 1034  
windows. The goal of this experiment is to identify which subsequences of the entire 1035  
time series are critical for classification. We examine how various modifications to the 1036  
original input impact model performance. It suggests which features are essential for 1037  
classification. 1038

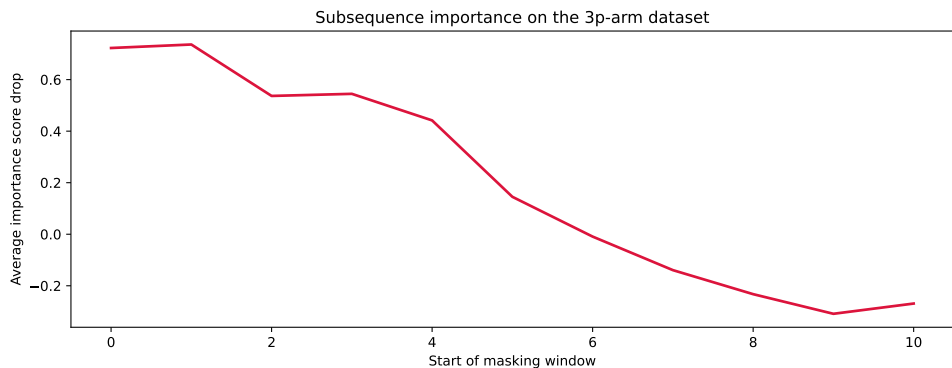
The model was trained on the original training dataset. For each instance in the test 1039  
dataset, we measure its original score and the masked score. We slid a masking window 1040  
 $w$  with a fixed length over the input time series  $T$ .  $|w|$  was set to 4. For each window 1041  
position  $i \in \{1, 2, \dots, |T| - |w| + 1\}$ , we masked all entries across all the channels of  $T$  1042  
within the window. Hence, we removed or hid that portion of information from the model 1043  
during inference. The changes in classification performance in terms of accuracy relative 1044  
to the unmasked original score of each  $i$  are recorded. Intuitively, if the information of a 1045  
subsequence is critical for the classification, the masking of this subsequence would lead 1046  
to a great drop in classification performance. We aggregated the importance score across 1047  
the test dataset. 1048

The result is shown in Figure 3.9. For the encoding methods, we cannot use the 1049  
methods derived from the cumulative mapping because the accumulation would leak in- 1050  
formation from the masked region. We adopted “Grouped fixed-length channel mapping” 1051  
as the encoding method and ROCKET as the classifier. “Grouped fixed-length channel 1052  
mapping” is the best encoding, other than the methods derived from the cumulative map- 1053  
ping, in all datasets, as shown in Figure 3.8. ROCKET is the best classifier, as shown in 1054  
Figure 3.7. 1055

In the 5p arm dataset, we found that masking subsequences at the tailing part caused 1056  
a significant drop in the importance score, as shown in Figure 3.9 (a). In the 3p arm 1057  
dataset, we found that masking subsequences at the leading part caused a significant 1058  
drop in the importance score, as shown in Figure 3.9 (b). 1059



(a) 5p arm



(b) 3p arm

Figure 3.9: Results of the perturbation experiment.

### 3.3.5 Summary

Our method achieves better or comparable predictive results and a 3.7X to 28.8X speedup compared to the state-of-the-art (SOTA).

## 3.4 Discussion

The channel ablation study reveals that the involvement of the time series derived from the secondary structure can improve accuracy. It suggests the importance of RNA folding in dicer processing. Furthermore, we found that the base-pair probability sequence of the secondary structure can also enhance accuracy. To the best of our knowledge, it is a novel application of the base-pair probability sequence. Experiments show that using the probability sequence as an additional channel can enhance accuracy more than incorporating it in the encoding. It is likely because keeping it as an additional channel can preserve more information, of both the probability sequence itself and the complementary strand.

Out of the three datasets, the best classifier is ROCKET. The ranking of the five classifiers by performance, starting from the best, is as follows: ROCKET, Hydra, MiniROCKET, MultiROCKET-Hydra, and MultiROCKET. It indicates that the fea-

tures created from the pooling operations that are only in MultiROCKET but not in MiniROCKET, confuse the final classifier. They are mean of positive values (MPV), mean of indices of positive values (MIPV) and longest stretch of positive values (LSPV) [43]. In contrast, the pooling operator that is only present in ROCKET but not in MiniROCKET, enhances the classification performance. It is maximum (MAX). 1075  
1076  
1077  
1078  
1079

For the encoding methods, we have the following observations. Fixed-length grouped channel mappings outperform variable-length counterparts with one exception in the multi-class dataset, likely because fixed-length schemes better preserve the original positional information of nucleotides within the sequence. Global cumulative methods consistently yield better performance than local cumulative methods. It suggests that the upstream information of the cleavage pattern plays a critical role in identifying cleavage sites. Cumulative-based encodings perform better than single-value mappings, with one exception in the 3p dataset, suggesting that the accumulated nucleotide signal is more informative for cleavage site prediction than the local or isolated presence of nucleotides. In the 5p arm dataset, encoding RNA sequence in two channels appears to worsen the result. This suggests that the 5p arm dataset and the 3p arm dataset need different nucleotide grouping methods for the encoding. 1080  
1081  
1082  
1083  
1084  
1085  
1086  
1087  
1088  
1089  
1090  
1091

One limitation of DiCleave is overfitting during training because of the relatively small size of the dataset [21]. DiCleave is a deep learning-based method. Deep learning models typically require a large amount of training data to generalize effectively. They are data-hungry. In contrast, MTSCCleav leverages ROCKET-based methods for the classification. They rely on random convolutional feature extraction followed by a simple linear classifier. The Ridge classifier used in this study is less data-hungry compared to deep learning methods due to its use of L2 regularization and the simplicity of its linear model nature. It allows ROCKET-based classifiers, and hence MTSCCleav, to maintain strong predictive performance even in settings with a relatively small dataset size. 1092  
1093  
1094  
1095  
1096  
1097  
1098  
1099  
1100

The subsequence importance reveals some connections between RNA secondary structure and human dicer cleavage site prediction. The perturbation experiment shows that the leading part of 5p arm and the tailing part of 3p arm are important for the classification. These parts are close to the center of the RNA secondary structure of pre-miRNA. It indicates that the center region is more crucial for human dicer cleavage site prediction. It is consistent with the previous study [20]. 1101  
1102  
1103  
1104  
1105  
1106

### 3.5 Concluding Remarks

1107

We proposed an accurate, fast, and simple multivariate time series classification (MTSC)-based method, termed MTSCCleav, for predicting human dicer cleavage sites. Base-pair probability sequences of the secondary structures have also been leveraged in the classification. MTSCCleav consists of three parts: time series encoding, time series 1108  
1109  
1110  
1111

transformation, and classification. ROCKET-based methods were used for time series transformation. Ridge Classifier was used for classification. For the computational experiments, we evaluated nine time series encoding methods in conjunction with five time series transformation methods. MTSCCleav outperformed the SOTA method in all five evaluation metrics for the 5p-arm and multi-class datasets, and four of the metrics for the 3p-arm dataset. In terms of computational efficiency, MTSCCleav with the optimal setting achieved an average 3.7X to 27.0X speedup over the SOTA method on the three datasets. With the use of a less accurate but faster time series classification method, MTSCCleav achieved an average speedup of 16.1X to 28.8X, respectively. We analyzed the subsequence importance of the input multivariate time series. The results show that subsequences near the center of the pre-miRNA sequences are more important. This aligns with the findings from previous work. This study demonstrates that time series analysis provides a powerful alternative to conventional modeling in the context of RNA processing. This framework may be extended to other RNA-processing tasks. Notably, the encoding of RNA sequence into time series enables us to utilize any well-established tools from the time series community.

# Chapter 4

1128

## Scaling with Multiple Scaling

1129

## Factors in Time Series Searching

1130

Time series data are ubiquitous across many different fields. Many data mining tasks, such as classification, clustering, and motif finding, have been defined for time series data. They utilize similarity search as a core subroutine, making it crucial to design similarity measures that align with our intuitions. To facilitate efficient computation, speedup techniques are essential. Dynamic Time Warping (DTW) is arguably the most prevailing distance measure for time series data. However, studies have shown that for certain data, another distance measure, namely Uniform Scaling (US), is equally crucial as DTW. DTW handles the local distortion, while US handles the global scaling. In addition, studies have demonstrated that combining DTW and US is necessary to obtain meaningful results in some cases. Surprisingly, all existing studies employ only a single scaling factor for the entire time series. A time series could consist of phases. Since each phase of a time series expresses at its own rate, using a single scaling factor is insufficient when comparing two time series that share similar phases but differ in their expression rates. We introduce the first framework that accounts for multiple scaling factors, Piecewise Scaling Distance (PSD). PSD employs other existing distance measures as subroutines. Because the naive implementation of PSD is slow, we propose a constrained version of PSD that enforces constraints based on the allowed segment lengths derived from the given scaling factor bound. It also prevents pathological results. In addition, two other speedup techniques have been proposed, which achieve 10.10X to 191.46X speedup. We also demonstrate the usage of a lower bound when DTW is used as the subroutine of PSD. Moreover, we show that the segmentation results returned by PSD can improve the accuracy of other distance measures.

1152

1153 **4.1 Background**

1154 To study the mechanism of a process, we take measurements. Measurements are usually  
1155 taken continuously by the sensors. Measurements of processes always yield continuous  
1156 values at discrete timestamps. They are time series data. For example, smartphones  
1157 collect users' GPS data. ECG monitors measure patients' heart rate. The continuous  
1158 measurements compose a time series. It is not hard to see why time series data are  
1159 ubiquitous across many different fields. In GPS data, each time series data point consists  
1160 of the user's latitude and longitude information. They are multivariate time series. In  
1161 ECG data, each data point represents the amplitude of the patient's cardiac electrical  
1162 activity. They are univariate time series. In this study, we focus on univariate time series.

1163 Many data mining tasks can be defined on time series data. For example, given a  
1164 time series database, we can perform clustering based on the pairwise similarity of the  
1165 time series instances. A classifier can be trained when categorical labels are available.  
1166 Alternatively, given a long time series, for motif finding, we identify recurring patterns.  
1167 In contrast, for anomaly detection, we identify abnormal subsequences. Almost all time  
1168 series data mining tasks can be reduced to arguing the similarity between two time series.  
1169 A good distance measure, also known as a similarity measure, can determine the success  
1170 or failure of the algorithms built on it. The choice of an appropriate distance measure is  
1171 particularly evident in classification. Studies show that simple nearest-neighbor classifi-  
1172 cation (1-NN) is difficult to beat and can compete with more complex methods [39].

1173 A time series is treated as a whole rather than as a collection of individual values.  
1174 The relationships between values are important. They constitute trends and shapes.  
1175 Hence, similarity search in time series data is approximate-based rather than exact match-  
1176 based [47]. Besides, different invariances should be allowed during the comparison.

1177 Dynamic Time Warping (DTW) is one of, if not the most common, similarity mea-  
1178 sures. DTW provides invariance to time distortion by aligning and measuring the sim-  
1179 ilarity between two series that may be misaligned in time. However, it assumes that  
1180 the time series are expressed on a similar global expression rate. This assumption limits  
1181 its performance when comparing two time series expressed at different global expression  
1182 rates. We often see this behavior in domains such as speech recognition, motion analysis,  
1183 patient biomedical signals, and sensor data in the manufacturing industry.

1184 Uniform Scaling (US) can achieve global scaling invariance by scaling the two time  
1185 series to the same length via interpolation, such as nearest-neighbor interpolation, before  
1186 comparison, as shown in Figures 4.1. It is reported that in some domains, such as  
1187 gestures [48, 49] and music performance [50], the scaling is about 10-15% (i.e., scaling  
1188 factors: 1.1 to 1.15). The scaling factors are relatively small, since the nature of the  
1189 music and the gait will change with significant scaling factors. However, in some other  
1190 domains, we may encounter larger scaling factors. In bioinformatics, gene expression time

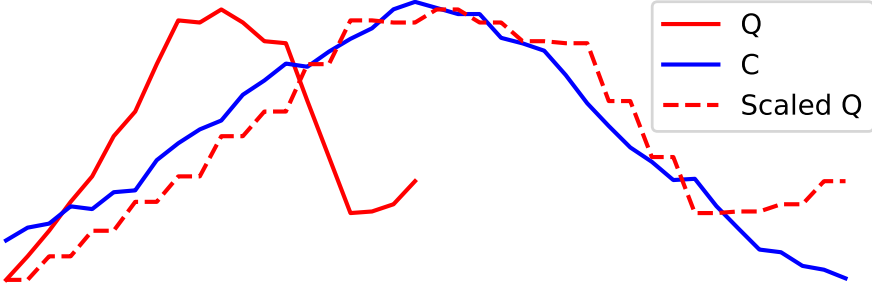


Figure 4.1: Applying nearest neighbor interpolation on  $Q$ , which result in Scaled  $Q$ , that can better reflect its similarity with  $C$ .

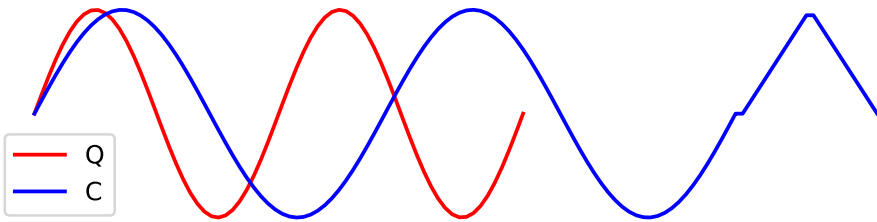


Figure 4.2:  $Q$  and  $C$  are in different rates. A stretching version of  $Q$  is similar to a prefix of  $C$ , but not the whole  $C$ .

series data could differ by a factor of 1.41 [51, 52]. In Figure 4.2,  $Q$  and a prefix of  $C$  1191  
are similar, but at different rates. In searching, we typically have a query  $Q$  and a longer 1192  
candidate  $C$ . We seek a prefix of  $C$  that is close to  $Q$ . For better comparison, we need 1193  
to eliminate the scaling effect. These observations demonstrate the necessity of uniform 1194  
scaling. 1195

DTW and US are used to achieve different kinds of invariance. DTW handles local 1196  
distortion, while US handles global scaling. Furthermore, some studies show that the 1197  
combination of US and DTW, namely USDTW, better reflects similarity [53, 54, 55]. US 1198  
is first applied to transform the two time series into the same length to eliminate the effect 1199  
resulting from the different rates. Then, DTW, rather than ED, is applied to address 1200  
local misalignment. USDTW is computationally more expensive than DTW because it 1201  
involves the calculation of the DTW between  $Q$  and different lengths of each prefix of  $C$ . 1202  
The different lengths of the prefixes correspond to different scaling factors. 1203

It is not uncommon for the data sampling strategy to change over time [56]. There are 1204  
different phases, each with its own rate. To achieve invariance for this kind of scaling effect 1205  
resulting from multiple rates, rather than using a single scaling factor, it is beneficial to 1206  
identify these different phases and use the appropriate scaling factors for these segments, 1207  
also known as pieces. We refer to this as piecewise scaling (PS). Figure 4.3 shows the 1208  
intuition of PS. The prefix of  $C$  (i.e.,  $C(1 : k)$ ) and  $Q$  share the same set of segments, 1209  
but each has a different scaling. Multiple scaling factors must be used. It motivates us 1210

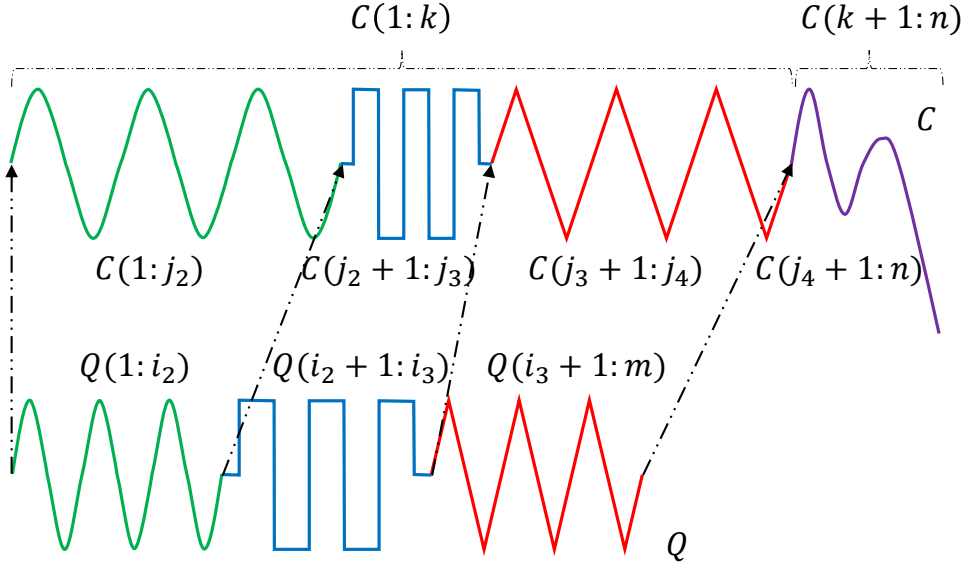


Figure 4.3: Intuition of piecewise scaling (PS).

1211 to design a new distance measure or framework that considers applying a scaling factor  
 1212 on each of the phases as defined by dashed lines in Figure 4.3, during the comparison of  
 1213 two time series.

1214 Our contributions are as follows:

- 1215 • We propose the first framework to achieve piecewise scaling (PS) invariance. In  
 1216 particular, we focus on two instantiations of PSD, namely PSED (i.e., ED with PS  
 1217 invariance) and PSDTW (i.e., DTW with PS invariance).
- 1218 • We design a dynamic programming method to compute PSD.
- 1219 • We propose a constrained version of PSD (cPSD) based on the allowed segment  
 1220 lengths. Besides, two other speedup techniques have been proposed. For a partic-  
 1221 ular instantiation of PSD, PDTW, we demonstrate the usage of a lower bound to  
 1222 further speed it up.
- 1223 • We demonstrate that the segmentation results returned by PSD can improve the  
 1224 accuracy of other distance measures.

1225 The rest of this paper is structured as follows. We present related work in Section 5.2  
 1226 and preliminaries in Section 4.3. Section 5.3 introduces our new distance measure frame-  
 1227 work, its constrained version, and speedup techniques. It is experimentally demonstrated  
 1228 in Section 4.5 for the problem of querying. In Section 5.5, we conclude this study with  
 1229 some future work.

## 4.2 Related Work

1230

This study focuses on distance measures of time series. For the overall review of time 1231 series, we direct the readers to [47, 57] for a more comprehensive understanding of this 1232 field. 1233

For many tasks, having appropriate distance measures that align with our intuition 1234 for the domains we work with is essential. One well-known distance measure is Dynamic 1235 Time Warping (DTW). It is initially designed for speech analysis [2]. However, DTW 1236 is computationally expensive. Lower bounds are used to speed up time series similarity 1237 search by admissibly pruning the unpromising candidates. One of the popular exact 1238 lower bounds of DTW is  $LB_{Keogh}$ . [58] improves the scalability of DTW by introducing a 1239 subsequence search suite of their four novel ideas, namely the UCR suite. For an overall 1240 review of lower bounds, we refer readers to [59, 60]. There is an approximate algorithm 1241 that approximates DTW with high accuracy while drastically cutting down the time and 1242 space requirements [61]. 1243

While ED is sensitive to distortions in the time axis, uniform scaling (US) has been 1244 shown to be a critical invariance in domains such as motion capture. [62] demonstrated 1245 that DTW is insufficient for handling global scaling effects, and that identifying DTW is 1246 not the solution to achieve this kind of invariance. There is a need for US. [63] extends 1247 the importance of uniform scaling to motif discovery. The authors show that meaningful 1248 motifs often suffer from a global scaling effect, causing standard motif finding algorithms 1249 to miss them completely. 1250

To the best of our knowledge, three studies analyze the combination of US and DTW, 1251 namely USDTW. It was first proposed by [53]. It extended  $LB_{Keogh}$  to bound the US- 1252 DTW. However, the extended  $LB_{Keogh}$  is still too loose with invariance to large amounts 1253 of uniform scaling. [54] and its follow-up study [55] proposed a new lower bound, namely 1254  $LB_{Shen}$ <sup>1</sup>, which has been shown to be tighter than  $LB_{Keogh}$  on USDTW. 1255

To our surprise, despite a fruitful discussion of DTW, US, and USDTW, no study has 1256 proposed a distance measure capable of handling scaling effects across multiple scaling 1257 factors. This is precisely what we will address in this study. 1258

## 4.3 Preliminaries

1259

We refer to time as the contextual attribute because it provides the context for the mea- 1260 surements to be made. We refer to the measurements as the behavioral attributes. Time 1261 series are multivariate when more than one behavioral attribute is present. Otherwise, it 1262 is called univariate. We focus on the univariate case. 1263

---

<sup>1</sup>It is denoted as  $LB_{New}$  in the original study. We rename it to prevent any confusion.

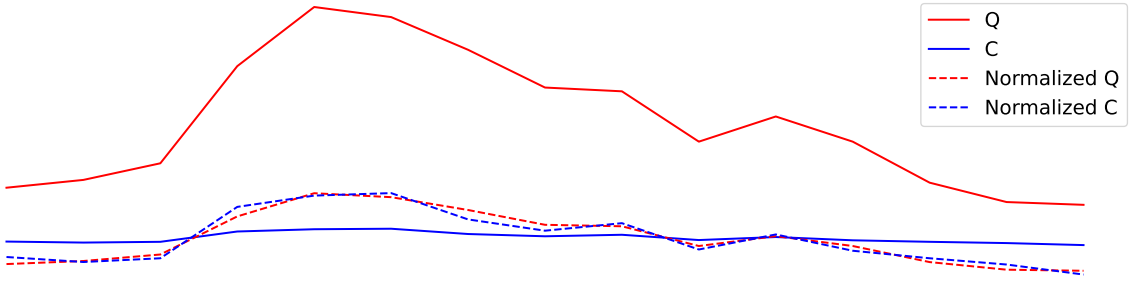


Figure 4.4: Z-normalization. Resulting time series have mean = 0 and std = 1.

1264 **Definition 1** (Time Series). A time series  $T = t_1, t_2, \dots, t_n$  is a sequence of real-valued  
1265 numbers with length =  $n$ .

1266 When two time series are involved in the discussion, we denote them as  $Q$  (Query)  
1267 and  $C$  (Candidate), with lengths  $m$  and  $n$ , respectively. Since  $Q$  is the query sequence,  
1268 it is not longer than  $C$  (i.e.,  $m \leq n$ ). The requirement of “ $m \leq n$ ” is a natural setting.  
1269 In “Query by Content”, a user is going to search for a candidate in the database from a  
1270 user-input query in which the query may only contain partial information of the target  
1271 candidate. For example, a user often wants to find a song or tune that is lingering in  
1272 their head by humming a part but not whole of the tune [64]. We are also interested in  
1273 a segment or subsequence of a time series.

1274 **Definition 2** (Subsequence). A subsequence  $T(i : j)$  of a time series  $T$  is a shorter time  
1275 series that starts from position  $i$  and ends at position  $j$  with length =  $j - i + 1$ . Both  
1276 ends are inclusive. Formally,  $T(i : j) = t_i, t_{i+1}, \dots, t_j$ ,  $1 \leq i \leq j \leq n$ .

1277 We call  $T(1 : j)$  the prefix of  $T$  of length  $j$ .

1278 Before comparison, we need to standardize or normalize them. A common way is  
1279 Z-Normalization, which is  $T = (T - \text{mean}(T)) / \text{std}(T)$ , as shown in Figure 4.4. The most  
1280 fundamental distance measure is the Euclidean Distance (ED).

### 1281 4.3.1 Euclidean Distance (ED)

1282 Given two points on a plane, it is intuitive to define the distance between them as the  
1283 length of the line segment between them. This idea extends to the case of  $n$ -dimensions  
1284 in time series with length  $n$ .

1285 **Definition 3** (Euclidean Distance (ED)). Given two series  $Q$  and  $C$  both with length  $n$ ,  
1286 the Euclidean Distance between them is defined as:

$$\text{ED}(Q, C) = \sqrt{\sum_{i=1}^n (q_i - c_i)^2} \quad (4.1)$$

A square root is usually involved in the computation of distance measures. It is a <sub>1287</sub> monotonic function. Since it does not change the relative ranking of the results, we can <sub>1288</sub> omit the square root operation for simplicity and optimization. ED aligns the entries <sub>1289</sub> between two series in a one-to-one manner. Two similar series will have a large distance <sub>1290</sub> under ED if they are not aligned well in the time dimension. ED cannot handle local <sub>1291</sub> distortion along the time axis because warping in the alignment is not allowed. A stan- <sub>1292</sub> dard distance measure that provides warping invariance is called Dynamic Time Warping <sub>1293</sub> (DTW). <sub>1294</sub>

### 4.3.2 Dynamic Time Warping (DTW)

Dynamic Time Warping (DTW) is an algorithm that measures similarity between two <sub>1296</sub> time series while accounting for local distortions. DTW aligns the two series by nonlin- <sub>1297</sub> early warping the time axis to minimize the final cumulative distance. <sub>1298</sub>

Given two time series,  $Q$  and  $C$ , we first construct an  $m$  by  $n$  distance matrix  $M$ . <sub>1299</sub> The origin  $(1, 1)$  is set at the bottom-left element of  $M$ . The  $(i, j)$  element of  $M$  <sub>1300</sub> contains the distance  $d(q_i, c_j)$  between points  $q_i$  and  $c_j$ . This local distance  $d(\cdot, \cdot)$  is <sub>1301</sub> usually calculated by  $(q_i - c_j)^2$ . Each  $(i, j)$  element refers to an alignment or mapping <sub>1302</sub> of the two points. A contiguous set of such elements forms a warping path  $W$ .  $W$  <sub>1303</sub> represents the non-linear alignment of  $Q$  and  $C$ .  $W = w_1, w_2, \dots, w_K$  in which  $w_k = (i, j)_k$  <sub>1304</sub> represents the mapping between  $q_i$  in  $Q$  and  $c_j$  in  $C$ , where  $\max(m, n) \leq K \leq m + n - 1$ . <sub>1305</sub> “ $\max(m, n) \leq K$ ” because the alignment of two series must include every point in both  $Q$  <sub>1306</sub> and  $C$ . “ $K \leq m + n - 1$ ” because the longest warping path is either the “concatenation of <sub>1307</sub> the bottom row and the rightmost column” (with the bottom-right cell being overlapped) <sub>1308</sub> or the “concatenation of the leftmost column and the top row” (with the top-left cell being <sub>1309</sub> overlapped). <sub>1310</sub>

The warping path  $W$  is typically subject to the following three constraints. <sub>1311</sub>

- Boundary conditions:  $w_1 = (1, 1)$  and  $w_K = (m, n)$ . The first (last) point of  $Q$  <sub>1312</sub> must map to that of  $C$ . <sub>1313</sub>
- Continuity: Given  $w_k = (i, j)$  and  $w_{k-1} = (i', j')$ ,  $i - i' \leq 1$  and  $j - j' \leq 1$ . An <sub>1314</sub> entry in the warping path  $W$  is adjacent to its one-step previous entry. <sub>1315</sub>
- Monotonicity: Given  $w_k = (i, j)$  and  $w_{k-1} = (i', j')$ ,  $i - i' \geq 0$  and  $j - j' \geq 0$ . The <sub>1316</sub> warping path  $W$  does not go back. <sub>1317</sub>

We denote  $W^*$  as a set of all allowed possible paths. <sub>1318</sub>

**Definition 4** (Dynamic Time Warping (DTW) [2]). DTW returns the minimum warping <sub>1319</sub> cost: <sub>1320</sub>

$$\text{DTW}(Q, C) = \min_{W \in W^*} \sum_{k=1}^{|W|} w_k \quad (4.2)$$

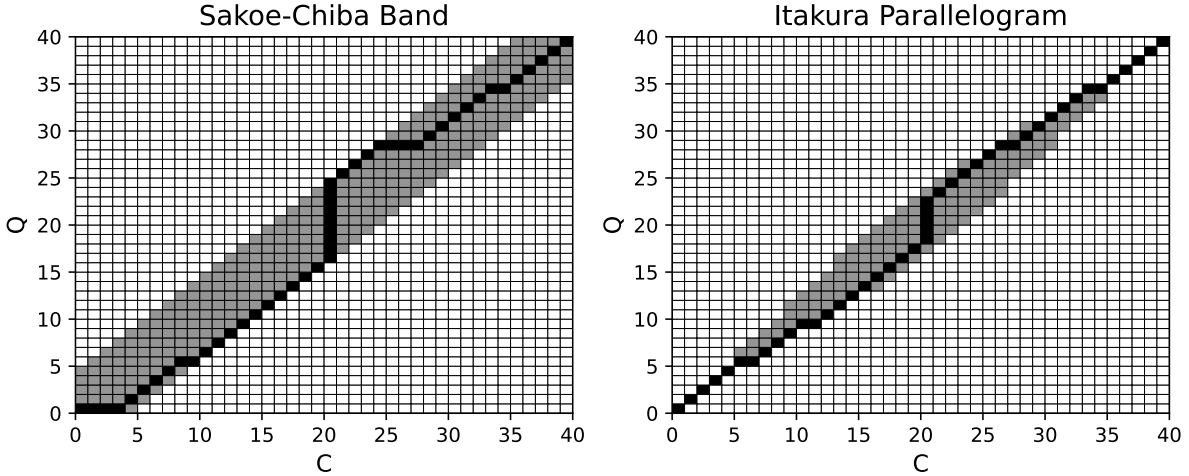


Figure 4.5: Visualization of  $D$  with local constraints. The black cells form the warping path.

To find the minimum warping cost and its corresponding warping path, we can use dynamic programming (DP) to evaluate the following recurrence.

$$D(i, j) = d(q_i, c_j) + \min \begin{cases} D(i - 1, j - 1), \\ D(i - 1, j), \\ D(i, j - 1) \end{cases} \quad (4.3)$$

It can be solved by building the accumulated cost matrix  $D$ , where the y-axis refers to  $Q$ , and the x-axis refers to  $C$ . The base cases, which are the first row and the first column, are defined as  $D(1, j) = \sum_{k=1}^j d(q_1, c_k), j \in [1, n]$  and  $D(i, 1) = \sum_{k=1}^i d(q_k, c_1), i \in [1, m]$ . After we have initialized the base cases, we can fill up  $D$  starting from the bottom up. There are  $m \times n$  entries in  $D$ . It takes  $\mathcal{O}(mn)$  to fill it up. Once  $D$  is built, we can find the path corresponding to this minimum cost by simple backtracking from the end cell  $D(m, n)$  to the origin cell  $D(1, 1)$ .

Some constraints have been proposed to prevent pathological warping paths with the aim of accuracy and efficiency. Two of the most popular are Sakoe-Chiba Band [2] and Itakura Parallelogram [3]. They only allow the warping paths to pass through the allowed region, as shown in Figure 4.5, by setting the cells outside this region in  $D$  to have  $\infty$  accumulated distance cost. [65] suggested that these constraints can be viewed as constraints on the warping path entry  $w_k = (i, j)_k$ . It represents these constraints as inequalities applying to the indices  $i$  and  $j$  locally, without depending on the main diagonal in  $D$ . In the Sakoe-Chiba Band, the constraints can be represented as  $j - r \leq$

$i \leq j + r$ , where  $r$  is an integer. It is sometimes specified as a fraction (or percentage) 1338 of the longer time series length to ensure length invariance. For clarity, we assume  $r$  is 1339 an integer unless specified otherwise. This means that  $q_i$  can only align with  $c_j$  if their 1340 indices differ by at most  $r$ . Since  $r$  defines the maximum allowed difference between the 1341 mapping indices,  $|n - m| \leq r$ , to ensure that the end points of  $Q$  and  $C$  can map. In 1342 the Itakura Parallelogram,  $r$  is a function of  $i$  rather than a constant value. ED can 1343 be seen as a special case of DTW where the warping path is fixed to be diagonal.  $q_i$  1344 aligns to  $c_i$  for every  $i$  (i.e.,  $r = 0$ ). DTW minimizes over all possible warping paths, 1345 and the warping path of ED is one of them. Because of the band, we only need to fill 1346 up the cells within the band. The complexity is  $\mathcal{O}(\#\text{of\_cells\_inside})$ . In the case of the 1347 Sakoe-Chiba Band, the band has a constant width  $w = 2r + 1$ . The complexity becomes 1348  $\mathcal{O}(w \times \text{length\_of\_diagonal}) = \mathcal{O}(rn)$ . The constrained DTW is denoted as  $\text{DTW}_r$ . 1349

### 4.3.3 Uniform Scaling (US)

In US, we compare the whole sequence of  $Q$  to a prefix of  $C$ , as shown in Figure 4.2. 1351 The two compared sequences are scaled to the same length via interpolation before ED 1352 is applied. A common interpolation method is nearest neighbor interpolation. 1353

**Definition 5** (Nearest Neighbor Interpolation). Given a time series  $T$  of length  $n$  and 1354 an integer  $L$ , Nearest Neighbor Interpolation scales  $T$  into  $T^L$  as follows: 1355

$$T_j^L = T_{\lceil n(j/L) \rceil} \quad \text{where } 1 \leq j \leq L \quad (4.4)$$

We can scale up or down a given series using Equation 4.4, as shown in Example 1. 1356

**Example 1.** Given a series  $T = 1, 2, \dots, 6$  with length  $n = 6$ . Let  $T(1 : 4)$  be the prefix 1357 of  $T$  of length  $k = 4$  (i.e.,  $T(1 : 4) = 1, 2, 3, 4$ ). Given an integer  $L = 8$ , we compute 1358  $T(1 : 4)^8$  as follows. 1359

$$\begin{aligned} T(1 : 4)^8 &= T_{\lceil 4(1/8) \rceil}, T_{\lceil 4(2/8) \rceil}, T_{\lceil 4(3/8) \rceil}, \dots, T_{\lceil 4(8/8) \rceil} \\ &= T_1, T_1, T_2, \dots, T_4 \\ &= 1, 1, 2, \dots, 4. \end{aligned}$$

When  $L > k$ ,  $T$  is said to be stretched. When  $L < k$ ,  $T$  is said to be shrunk. 1360

**Definition 6** (Uniform Scaling (US) [62]). Given two series  $Q$  and  $C$ , of length  $m$  and 1361  $n$  respectively, and a scaling factor bound  $l$ , where  $l \geq 1$ . Let  $C(1 : k)$  be the prefix of 1362  $C$ , where  $\lceil m/l \rceil \leq k \leq \min(\lfloor lm \rfloor, n)$ , and  $C(1 : k)^L$  be a rescaled version of  $C(1 : k)$  with 1363 length  $L$ , where  $L = \min(\lfloor lm \rfloor, n)$ .  $L$  is called the alignment factor.  $\min(\lfloor lm \rfloor, n)$  is the 1364

1365 largest alignment factor.

$$\text{US}(Q, C, l, L) = \min_{k=\lceil m/l \rceil}^{\min(\lfloor lm \rfloor, n)} \text{ED}(Q^L, C(1:k)^L) \quad (4.5)$$

1366  $L$  is set as the largest alignment factor [55] to ensure all the points in  $Q$  and  $C(1:k)$  are  
 1367 preserved during interpolation because of up-sampling, and the scaled version of all the  
 1368 prefixes is going to have the same length (i.e.,  $L$ ), for fair comparison, since comparison  
 1369 between two longer time series generally results in a larger distance measure. Through  
 1370 Equation 4.5, we find the minimum value and the corresponding argument (i.e.,  $k$ ) by  
 1371 checking the minimum value of the ED function from  $\lceil m/l \rceil$  to  $\min(\lfloor lm \rfloor, n)$ . The scaling  
 1372 factor is defined by the argument minimum value of  $k$ . The smaller  $k$  is, the more we  
 1373 need to “stretch”  $C$  for  $Q$  to compare with  $C(1:k)$ , which is  $m/k$  times.

1374 Consider a time series database  $D$  comprising a set of candidate instances, and a  
 1375 single query series  $Q$ . The search task aims to retrieve the most similar instance (or  
 1376 top- $k$  instances) from  $D$  to  $Q$ . We maintain  $Q$  as a fixed reference and extract only the  
 1377 prefixes from each instance in  $D$  for comparison. Furthermore, to simplify notation, we  
 1378 apply scaling exclusively to the instances in  $D$ , leaving  $Q$  unscaled.

#### 1379 4.3.4 Uniform Scaling & Dynamic Time Warping (USDTW)

1380 Uniform Scaling & Dynamic Time Warping (USDTW) measures the similarity by apply-  
 1381 ing scaling with an appropriate scaling factor on  $C$  and then applying DTW. The tail  
 1382 part of  $C$  can be ignored, as shown in Figure 4.2.

1383 **Definition 7** (Uniform Scaling & Dynamic Time Warping (USDTW) [55]). With the  
 1384 same notations defined in Definition 6,

$$\text{USDTW}_r(Q, C, l, L) = \min_{k=\lceil m/l \rceil}^{\min(\lfloor lm \rfloor, n)} \text{DTW}_r(Q^L, C(1:k)^L) \quad (4.6)$$

1385 where  $r$  is the DTW constraint parameter.

1386 We replace the ED function in Equation 4.5 by DTW function to form Equation 4.6.  
 1387 As mentioned in Section 5.1, there may exist more than one scaling factor. Hence,  
 1388 both the existing distance measures, US and USDTW, which are designed to handle  
 1389 only one scaling factor, are insufficient. This motivates us to design a new framework of  
 1390 distance measures.

### 4.3.5 Lower Bounds for DTW and USDTW

1391

We first introduce the concept of lower bounds and explain how they can benefit search. 1392  
 DTW is computationally more expensive than ED. They compute an accumulated cost 1393  
 matrix of size  $m \times n$ , where  $m$  and  $n$  denote the lengths of the two time series. It 1394  
 results in quadratic complexity. This complexity poses a challenge for similarity search. 1395  
 The most common approach is to compute a lower bound of the real value, which is 1396  
 computationally cheap and tight. We can use this lower bound to filter out unpromising 1397  
 candidates and perform the expensive distance computation only on the small set of 1398  
 promising candidates. In searching, we would keep track of the best\_so\_far distance bsf 1399  
 between the query  $Q$  and the testing candidates. When testing a new candidate  $C$ , we 1400  
 first compute the  $\text{LB}(Q, C)$ . We only compute the actual DTW when  $\text{LB}(Q, C) \leq \text{bsf}$ . 1401

We then introduce some common lower bounds. 1402

**Kim Lower Bound [66]:**  $\text{LB}_{\text{Kim}}$  is a simple and fast lower bound of DTW. The 1403  
 complexity is  $O(1)$ . It uses the four features in  $Q$  and  $C$ . We denote  $t_{-1}$  as the last point 1404  
 and  $t_{\max}$  ( $t_{\min}$ ) as the maximum (minimum) point in time series  $T$ . 1405

$$\text{LB}_{\text{Kim}} = \max \begin{cases} d(q_1, c_1) \\ d(q_{-1}, c_{-1}) \\ d(q_{\max}, c_{\max}) \\ d(q_{\min}, c_{\min}) \end{cases} \quad (4.7)$$

$d(\cdot, \cdot)$  refers to the local distance used in the point alignment. The first two lines come 1406  
 from the boundary condition in DTW. The alignment between the first pair of points and 1407  
 the last pair of points must contribute to the accumulated sum of DTW. Each point in 1408  
 $Q$  must align with some point in  $C$ , and vice versa. Each alignment contributes a local 1409  
 distance to the final sum. The minimum possible local distance for the alignment of  $q_{\max}$  1410  
 would be the one aligned with  $c_{\max}$ . The same applies to the last line in the equation. 1411

There is a simplification of  $\text{LB}_{\text{Kim}}$ . Only the first and last pair are used in the lower 1412  
 bound computation. In the normalized time series, the third and fourth rows in Equa- 1413  
 tion 4.7 should have small values [58]. Ignoring them can improve the complexity from 1414  
 $\mathcal{O}(n)$  to  $\mathcal{O}(1)$ . The simplified lower bound is  $\text{LB}_{\text{KimFL}} = d(q_1, c_1) + d(q_{-1}, c_{-1})$ . 1415

**Keogh Lower Bound [65]:**  $\text{LB}_{\text{Keogh}}$  builds the upper  $U$  and lower envelopes  $L$  of 1416  
 one of the time series out of the two compared sequences. Usually, the envelopes are 1417  
 constructed for  $Q$  instead of  $C$  as we will compare one  $Q$  against many  $C$ 's. Otherwise, 1418  
 we need to build the envelopes for each candidate instead [58]. 1419

To the best of our knowledge, they are the first to interpret the constraint as a 1420  
 restriction on the indices of the warping path  $w_k = (i, j)_k$  such that  $j - r \leq i \leq j + r$ , 1421  
 where  $r$  defines the allowable deviation of alignment between  $q_i$  and  $c_j$ . For ease of 1422

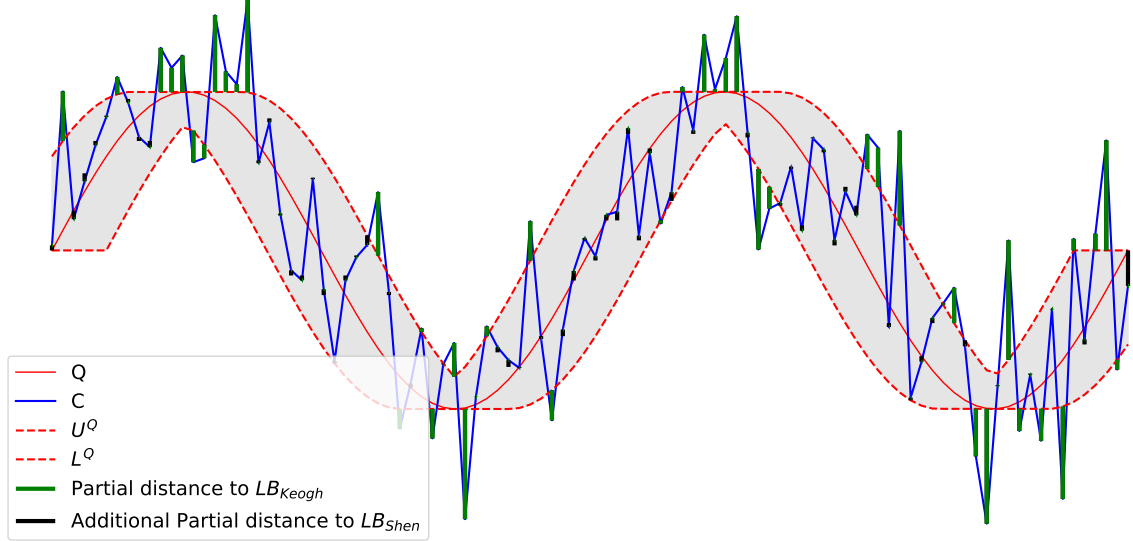


Figure 4.6: Visualization of LB<sub>Keogh</sub> and LB<sub>Shen</sub>

exposition, we focus on the most used constraint in the literature, which is the Sakoe-Chiba Band [67]. Two sequences are constructed for  $Q$ , namely the upper  $U^Q$  and lower envelopes  $L^Q$  of  $Q$  as shown in Figure 4.6. For each  $q_i$ , we would assign a window of  $q_i$  based on its index  $i$  as follows.

$$\begin{aligned} U_i^Q &= \max(q_{\max(1,i-r)} : q_{\min(i+r,m)}) \\ L_i^Q &= \min(q_{\max(1,i-r)} : q_{\min(i+r,m)}) \end{aligned} \quad (4.8)$$

$\max(1, \cdot)$  and  $\min(\cdot, m)$  are used for handling the boundary cases.  $U^Q$  and  $L^Q$  together form a bounding envelope that encloses the original  $Q$ , it is the grey region in the figure. For each  $c_j$ , either  $(c_j, U_j^Q)$  or  $(c_j, L_j^Q)$  corresponds to the possible alignment that contributes the minimum distances if  $c_j$  falls outside the envelope. Herein, the lower bound is the sum of these distances, as shown in the following equation.

$$\text{LB}_{\text{Keogh}}(Q, C) = \sum_{j=1}^n \begin{cases} d(c_j, U_j^Q) & \text{if } c_j > U_j^Q \\ d(c_j, L_j^Q) & \text{if } c_j < L_j^Q \\ 0 & \text{otherwise} \end{cases} \quad (4.9)$$

Visually, these distances are the distances between  $c_j$  outside the envelope and the vertically corresponding points on the envelope. The distances are the green bars in the figure. Equation 4.9 returns the sum of the green bars.

**Shen Lower Bound [54, 55]:** It leverages the boundary and continuity conditions to create a lower bound of DTW. It can be used to lower-bound the USDTW with slight modification. The intuition is to find the minimum possible alignment of each  $c_j$  with

points in  $Q$ , subject to the local constraint  $r$  from DTW and the global constraint  $l$  from US. 1438  
1439

We will first introduce  $\text{LB}_{\text{Shen}}$  for DTW. Given the candidate sequence  $C$  with length  $n$ , for each  $c_j$ , we create its possible reach  $\mathbf{q}_j$  in  $Q$  under DTW as in Equation 4.10. The elements  $\mathbf{q}_j$  form an indexed collection  $\mathbb{Q} = (\mathbf{q}_1, \mathbf{q}_2, \dots, \mathbf{q}_{\min(\lfloor lm \rfloor, n)})$ . 1440  
1441  
1442

$$\mathbf{q}_j = (q_{\max(1, j-r)}, \dots, q_{\min(j+r, m)}) \quad (4.10)$$

We define  $\delta(x, Y) = \min_{y \in Y} d(x, y)$ . The possible minimum cost contributed by the alignment of  $c_j$  and some point in  $Q$  to the accumulated sum would be  $\delta(c_j, \mathbf{q}_j)$ . The lower bound  $\text{LB}_{\text{Shen}}$  is defined as: 1443  
1444  
1445

$$\text{LB}_{\text{Shen}}(Q, C) = d(c_1, q_1) + \sum_{j=2}^{n-1} \delta(c_j, \mathbf{q}_j) + d(c_n, q_m) \quad (4.11)$$

We direct the reader to [54] for the formal proof, while an intuition of the proof is presented here. There are three items on the right-hand side of Equation 4.11. The continuity requirement ensures that each  $c_i$  is involved in at least one alignment. The first and the last items are from the boundary condition. The middle item returns the possible minimum distances contributed by each  $c_j$ 's, where  $2 \leq j \leq n - 1$ . It is obvious that  $\text{LB}_{\text{Shen}}$  in Equation 4.11 is tighter when we use the first pair of points and the last pair of points instead of doing the middle summation all from  $j = 1$  to  $n$ . It is because the distance contributed by the first pair (last pair) must be greater than  $\delta(c_1, \mathbf{q}_1)$  ( $\delta(c_n, \mathbf{q}_n)$ ). 1446  
1447  
1448  
1449  
1450  
1451  
1452  
1453

It is proven that it is tighter than  $\text{LB}_{\text{Keogh}}$  [54]. It is shown in Figure 4.6 visually. The black bars refer to the additional lower bound distance sum on top of  $\text{LB}_{\text{Keogh}}$ . We will give an intuitive proof here. Both  $\text{LB}_{\text{Keogh}}$  and  $\text{LB}_{\text{Shen}}$  compute the lower bounds by summing the local distance resulting from the alignment of each  $c_j$  with some points in  $Q$ , which is guaranteed to be not greater than the partial distance contributed by the real alignment, which we only know until we compute the exact distance measure. In  $\text{LB}_{\text{Keogh}}$ , if this  $c_j$  falls outside the envelope, this local distance is the vertical distance between  $c_j$  and the envelope. If  $c_j$  falls inside, this local distance would be 0. For those points outside the envelope, the local distances for  $c_j$  of  $\text{LB}_{\text{Keogh}}$  and  $\text{LB}_{\text{Shen}}$  are the same. But  $\text{LB}_{\text{Shen}}$  aims to return the minimum possible partial distance for each  $c_j$ , even within the envelope. Hence,  $\text{LB}_{\text{Keogh}} \leq \text{LB}_{\text{Shen}}$ . 1454  
1455  
1456  
1457  
1458  
1459  
1460  
1461  
1462  
1463  
1464

In order to compute Equation 4.11 efficiently, we first sort sequences  $\mathbf{q}_j$  and the resulting sorted sequences are denoted as  $\tilde{\mathbf{q}}_j$ . The sorted sequences allow us to do a binary search when we are calculating  $\delta(c_j, \tilde{\mathbf{q}}_j)$  in contrast to  $\delta(c_j, \mathbf{q}_j)$ . The sorting only needs to be done once because we are testing the same  $Q$  with different candidates. 1465  
1466  
1467  
1468

It can be extended to the USDTW case [54, 55]. The possible reach now is not only defined by  $r$ , but also by the scaling factor bound  $l$ . 1469  
1470

$$\mathbf{q}_j = (q_{\max(1, \lceil j/l \rceil - r)}, \dots, q_{\min(\lfloor j/l \rfloor + r, m)}) \quad (4.12)$$

[54] proves the following theorem to allow us to consider the lower bound between each prefix of  $C$  and  $Q$  without the scaling up of each prefix of  $C$  (i.e.,  $C(1 : k)^L$ ) and the scaling up of  $Q$  (i.e.,  $Q^L$ ).

**Theorem 8.** For any  $\lceil m/l \rceil \leq k \leq \min(\lfloor lm \rfloor, n)$ ,  $\text{DTW}_r(Q^{\min(\lfloor lm \rfloor, n)}, C(1 : k)^{\min(\lfloor lm \rfloor, n)})$  is always lower bounded by  $\sum_{j=1}^k \delta(c_j, \mathbf{q}_j)$ .

Recall that USDTW calculates DTW distances between each rescaled prefix of  $C$  to the rescaled  $Q$ , and outputs the minimum DTW distance, as in Equation 4.6. The incremental nature of the lower bound frees us to calculate the lower bound of each DTW distance from scratch. This theorem allows us to first calculate the lower bound of the shortest prefix  $C(1 : \lceil m/l \rceil)$  of  $C$  and  $Q$ , and then incrementally calculate the lower bound of the longer prefix with length from  $\lceil m/l \rceil + 1$  to  $\min(\lfloor lm \rfloor, n)$  by adding on each  $\delta(c_j, \mathbf{q}_j)$ . To note, it also means that if  $\text{LB}_{\text{Shen}}(Q, C(1 : k))$  is larger than a value, namely bsf,  $\text{LB}_{\text{Shen}}(Q, C(1 : k'))$ , where  $k' > k$ , would also be larger than bsf. To note, we can tighten  $\text{LB}_{\text{Shen}}$  by using  $d(c_1, q_1)$  instead of  $\delta(c_1, \mathbf{q}_1)$ .

The above analysis can also apply to the case of US distance. We only need to define the corresponding reaches as follows:

$$\mathbf{q}_j = (q_{\max(1, \lceil j/l \rceil)}, \dots, q_{\min(\lfloor j/l \rfloor, m)}) \quad (4.13)$$

## 4.4 Piecewise Scaling Distance

The motivation stems from the limitations of US and USDTW. They assume that the relationship between  $Q$  and  $C$  is governed by only a single, global scaling factor. This assumption fails when applied to multi-rate data, where different phases of the time series express at different rates.

Note that existing studies [62, 58] can find all scaling factors, defined by the chosen prefix of  $C$ , ranging from  $\lceil m/l \rceil$  to  $\min(\lfloor lm \rfloor, n)$ . However, they can use only one of them in the scaling. Consider the following illustrative example in ASCII text [58], where character repetition represents the duration of spoken phonemes, and space indicates a pause:

- “time series 20 25” and “time series 20 25”. Here, the Hamming distance (the discrete analogue of ED) fails due to misalignment in the underlined locations, but the string edit distance (the discrete analogue of DTW) can resolve it.
- “time sseerriiss 222000222555”. This sequence exhibits three distinct phases with scaling factors of 1, 2, and 3, respectively. The corresponding invariance cannot be

achieved by DTW or US (which is restricted to a single global scalar). US would 1502  
enforce a single compromised global scale instead. 1503

In Query-by-Content scenarios, such as query-by-humming or gesture retrieval, the 1504  
query is generated by a human. Humans do not maintain a consistent rate for each 1505  
phase. For example, humans rush through a familiar sequence but slow down for a 1506  
new or complex sequence. It is commonly observed in a piece of music performed by a 1507  
beginner. The piece's tempo is not uniform. 1508

We introduce a novel distance measure framework, termed Piecewise Scaling Distance 1509  
(PSD). It addresses the local scaling effect within each phase by employing a scaling factor 1510  
to each phase, instead of using a single scaling factor for the whole time series. It releases 1511  
the basic constraint or assumption made in US and USDTW. PSD employs an existing 1512  
distance metric, such as ED or DTW, to quantify the similarity of aligned segment pairs. 1513  
While the PSD framework is agnostic to the underlying metric, this study focuses on its 1514  
two fundamental instantiations: 1515

- PSED, which employs ED to compute the similarity of aligned segment pairs. 1516
- PSDTW, which employs DTW to compute the similarity of aligned segment pairs. 1517

In the formulation that follows, we utilize PSDTW as the running example. PSDTW 1518  
generalizes PSED. The PSED formulation can be trivially derived from it. 1519

#### 4.4.1 Piecewise Scaling & Dynamic Time Warping (PSDTW) 1520

**Problem formulation:** To simplify the discussion, we focus on the comparison between 1521  
 $Q$  and the entire sequence  $C$ , rather than a prefix of  $C$ . Note that this formulation can 1522  
be generalized to prefix matching as in Definition 6 and Definition 7. 1523

Given two sequences  $Q$  and  $C$ , where  $Q$  is not longer than  $C$ ,  $|Q| = m \leq |C| = n$ , and 1524  
the number of segments or pieces  $P$  allowed, our goal is to segmentalize both  $Q$  and  $C$  1525  
into  $P$  contiguous segments automatically in a way that minimize the total sum of DTW 1526  
distance of aligned segment pairs with interpolation. 1527

**Definition 9** (Piecewise Scaling & Dynamic Time Warping (PSDTW)). With the same 1528  
notations defined in Definition 7, 1529

$$\begin{aligned} \text{PSDTW}_r(Q, C, l, L, P) = \\ \min_{\substack{i_1 < i_2 < \dots < i_{P+1} \\ j_1 < j_2 < \dots < j_{P+1}}} \sum_{p=1}^P \text{DTW}_r(Q(i_p + 1 : i_{p+1})^L, \\ C(j_p + 1 : j_{p+1})^L) \end{aligned} \quad (4.14)$$

, where  $i_1 = 0$ ,  $i_{P+1} = m$ ,  $j_1 = 0$ ,  $j_{P+1} = n$  and the setting of  $L$  will be discussed later. 1530

---

**Algorithm 1** Naive PSDTW

---

**Input:** Query series  $Q$ , Candidate series  $C$ , DTW constraint parameter  $r$  (in fraction),

Number of pieces  $P$ , Scaling parameter  $L$

**Output:** Distance Matrix  $D$  of size  $(m + 1) \times (n + 1) \times (P + 1)$

```
1: Initialize  $D$  with  $\infty$ 
2:  $D[0, 0, 0] \leftarrow 0$ 
3: for  $p \leftarrow 1$  to  $P$  do
4:   for  $i \leftarrow 1$  to  $m$  do
5:     for  $j \leftarrow 1$  to  $n$  do
6:        $D[i, j, p] \leftarrow \min_{i' < i, j' < j} \{D[i', j', p - 1]$ 
          $+ \text{DTW}_r(Q(i' + 1 : i)^L, C(j' + 1 : j)^L)\}$ 
7: return  $D[m, n, P]$ 
```

---

**Algorithm 2** Line 6 in Algorithm 1

---

```
1: for  $i' \leftarrow 0$  to  $i - 1$  do
2:   for  $j' \leftarrow 0$  to  $j - 1$  do
3:      $dist_{\text{prev}} \leftarrow D[i', j', p - 1]$ 
4:      $dist_{\text{seg}} \leftarrow \text{DTW}_r(Q(i' + 1 : i)^L, C(j' + 1 : j)^L)$ 
5:      $D[i, j, p] \leftarrow \min(D[i, j, p], dist_{\text{prev}} + dist_{\text{seg}})$ 
```

---

1531     Essentially,  $L$  needs to be at least the length of all segments to preserve all the points  
1532     by up-sampling.

1533     We refer to Figure 4.3 to clarify Equation 4.14. Given two sequences  $Q$  and  $C$ , with the  
1534     aid of different colors and the dashed lines, we observe that  $Q$  consists of three segments  
1535     while  $C$  consists of four segments, with the first three segments of  $C$  similar to those  
1536     of  $Q$ . They form three segment pairs. The scaling factor used in each segment pair is  
1537     determined from the length of the two subsequences involved, i.e.,  $(i_{p+1} - i_p)/(j_{p+1} - j_p)$ .  
1538     These three parts have different scaling factors. For example, the first part in  $C$  is the  
1539     stretched version of that in  $Q$ . The second part in  $C$  is the compressed version of that in  
1540      $Q$ .

1541     Equation 4.14 can be formulated in a recurrence relation as follows. Let  $D[i, j, p]$  be  
1542     the minimum cost to align the first  $i$  points in  $Q$  (i.e.,  $Q(1 : i)$ ) with the first  $j$  points in  
1543      $C$  (i.e.,  $C(1 : j)$ ) using exactly  $p$  segments:

$$D[i, j, p] = \min_{\substack{i' < i \\ j' < j}} \left\{ D[i', j', p - 1] + \text{DTW}_r(Q(i' + 1 : i)^L, C(j' + 1 : j)^L) \right\} \quad (4.15)$$

1544 **Naive PSDTW:**

---

**Algorithm 3** Initialization of PSDTW

---

- 1:  $L_{\text{gmin}}^Q \leftarrow \lceil (m/P)/\sqrt{l} \rceil, \quad L_{\text{gmax}}^Q \leftarrow \lfloor (m/P)\sqrt{l} \rfloor$  ▷ “g” refers to “global”.
  - 2:  $L_{\text{gmin}}^C \leftarrow \lceil (n/P)/\sqrt{l} \rceil, \quad L_{\text{gmax}}^C \leftarrow \lfloor (n/P)\sqrt{l} \rfloor$
  - 3:  $L = \max(L_{\text{gmax}}^Q, L_{\text{gmin}}^C)$
  - 4: Initialize  $D$  of size  $(m+1) \times (n+1) \times (P+1)$  with  $\infty$
  - 5:  $D[0, 0, 0] \leftarrow 0$
- 

Our goal is  $D[m, n, P]$ . Equation 4.15 can be solved exactly by dynamic programming 1545 (DP). The base case is  $D[0, 0, 0] = 0$ . It refers to the zero cost to align the first 0 point 1546 (i.e., the empty prefix) of  $Q$  with that of  $C$ . Other cells in  $D$  are first initialized with  $\infty$ . 1547 They are calculated using a bottom-up approach via Equation 4.15. A straightforward 1548 implementation in DP is shown in Algorithm 1. Line 6 is achieved by looping all the 1549 previous indices of the current  $i$  and  $j$  as in Algorithm 2. 1550

We explain the lines in Algorithm 2. Line 3 retrieves the accumulated distance cost 1551 from the beginning up to the endpoints  $(i', j')$ , and saves it as  $dist_{\text{prev}}$ . Line 4 considers 1552 the current aligned segment pair, which consists of  $Q(i'+1 : i)$  and  $C(j'+1, j)$ , and they 1553 are interpolated to the length  $L$ . The DTW distance of this pair is calculated and saved 1554 as  $dist_{\text{seg}}$ . 1555

We now analyze the time complexity of Algorithm 1. There are  $Pmn$  entries in  $D$ . 1556 The  $\min$  operator in line 6 takes  $\mathcal{O}(mn)$ . Hence, the time complexity of Algorithm 1 1557 is  $\mathcal{O}(Pm^2n^2) = \mathcal{O}(Pn^4)$ , multiplied by the running time of the DTW. It is slow, which 1558 prevents us from using it in practice. To note, we use  $r$  in a fraction instead of a fixed 1559 integer here. This allows the deviation tolerance to scale adaptively with pieces of varying 1560 lengths. 1561

#### 4.4.2 Speedup Techniques

---

**Length constraints of the segment:** A way to reduce complexity and to prevent 1563 pathological segment pairs is to limit the possible segment lengths that are considered by 1564 constraining the minimum and maximum lengths of segments. It is similar to constrained 1565 DTW, in which we limit the search space of the warping path as in Figure 4.5. The 1566 version of PSDTW that considers the segment constraint is termed constrained PSDTW 1567 (cPSDTW). It is shown in Algorithm 4. The uncolored part shows the main logic, while 1568 the colored part shows the speedup techniques, which will be explained later. 1569

We initialize in Algorithm 3. For a given number of segments  $P$ , the expected length 1570 of each segment in  $Q$  and  $C$  would be  $m/P$  and  $n/P$ , respectively. For  $Q$ , we set the 1571 minimum possible segment length  $L_{\text{gmin}}^Q$  to be  $\lceil (m/P)/\sqrt{l} \rceil$  and the maximum possible 1572 length  $L_{\text{gmax}}^Q$  to be  $\lfloor (m/P)\sqrt{l} \rfloor$  in line 1 such that the scaling ratio of any two segments 1573 in  $Q$  would be bounded by  $l$ . It allows some deviation in the length of the segments from 1574 their expected length. Similarly, we compute the segment constraints for  $C$  in line 2. We 1575

---

**Algorithm 4** Constrained PSDTW (cPSDTW) with early abandoning and lower bounding

---

**Input:** Query series  $Q$ , Candidate series  $C$ , DTW constraint parameter  $r$  (in fraction), Number of pieces  $P$ , best\_so\_far bsf

**Output:** The final distance  $D[m, n, P]$  if  $D[m, n, P] \leq \text{bsf}$ , otherwise  $\infty$

- 1: Execute Algorithm 3 for initialization
- 2: **for**  $p \leftarrow 1$  **to**  $P$  **do**
- 3:   **for**  $i \leftarrow (p \cdot L_{\text{gmin}}^Q)$  **to**  $\min(p \cdot L_{\text{gmax}}^Q, m)$  **do** ▷ The iterations can be parallelized.
- 4:     **for**  $L^Q \leftarrow L_{\text{gmin}}^Q$  **to**  $L_{\text{gmax}}^Q$  **do**
- 5:        $i' \leftarrow i - L^Q$  ▷  $i'$ : End point of previous segment on  $Q$ .
- 6:        $Q' \leftarrow \text{rev}(Q(i' + 1 : i))$  ▷  $\text{rev}(T)$ : Reverse the input series  $T$ .
- 7:        $L_{\text{min}}^C \leftarrow \max(L_{\text{gmin}}^C, \lceil L^Q/l \rceil)$
- 8:        $L_{\text{max}}^C \leftarrow \min(\lfloor L^Q/l \rfloor, L_{\text{gmax}}^C)$
- 9:        $r' \leftarrow r \times \max(L^Q, L_{\text{max}}^C)$  ▷ Compute the integer value of  $r$ .
- 10:      **for**  $k \leftarrow 1$  **to**  $L_{\text{max}}^C$  **do**
- 11:        $\mathbf{q}_k \leftarrow (q'_{\max(1, \lceil k/l \rceil - r')}, \dots, q'_{\min(\lfloor k/l \rfloor + r', L^Q)})$  ▷ Construct indexed collection  $\mathbb{Q}$ .
- 12:        $\tilde{\mathbf{q}}_k \leftarrow \text{sort}(\mathbf{q}_k)$
- 13:       **for**  $j \leftarrow (p \cdot L_{\text{gmin}}^C)$  **to**  $\min(p \cdot L_{\text{gmax}}^C, n)$  **do**
- 14:         **for**  $L^C \leftarrow L_{\text{min}}^C$  **to**  $L_{\text{max}}^C$  **do**
- 15:            $j' \leftarrow j - L^C$
- 16:            $C' \leftarrow \text{rev}(C(j' + 1 : j))$
- 17:            $dist_{\text{prev}} \leftarrow D[i', j', p - 1]$
- 18:           **if**  $dist_{\text{prev}} = \infty$  **then**
- 19:             **continue**
- 20:           **if**  $dist_{\text{prev}} > \text{bsf}$  **then**
- 21:             **continue**
- 22:           **if**  $dist_{\text{prev}} > D[i, j, p]$  **then** ▷  $D[i, j, p]$  stores the best so far.
- 23:             **continue**
- 24:           **if**  $L^C = L_{\text{min}}^C$  **then** ▷ Compute the lower bound from sketch.
- 25:              $lb = (c'_1 - q'_1)^2$  ▷ Partial distance contributed by the first alignment.
- 26:             **for**  $k \leftarrow 2$  **to**  $L^C$  **do**
- 27:                $lb = lb + \delta(c'_k, \tilde{\mathbf{q}}_k)$
- 28:           **else**
- 29:              $lb = lb + \delta(c'_{L^C}, \tilde{\mathbf{q}}_{L^C})$  ▷ Compute the lower bound incrementally.
- 30:              $lb_{\text{check}} = lb - \delta(c'_{L^C}, \tilde{\mathbf{q}}_{L^C}) + (c'_{-1} - q'_{-1})^2$  ▷ Tighten the lower bound by using the last alignment.
- 31:           **if**  $dist_{\text{prev}} + lb_{\text{check}} > D[i, j, p]$  **then**
- 32:             **continue**
- 33:            $dist_{\text{seg}} \leftarrow \text{DTW}_r(Q'^L, C'^L)$
- 34:           **if**  $dist_{\text{prev}} + dist_{\text{seg}} < D[i, j, p]$  **then**
- 35:              $D[i, j, p] \leftarrow dist_{\text{prev}} + dist_{\text{seg}}$  ▷ Also save pointer  $(i', j')$  for the cut.
- 36: **return**  $D[m, n, P]$

---

1576 set the maximum segment length be the alignment factor  $L$  in line 3. We set the base  
 1577 case in line 5.

1578 We fill the table  $D$  in Algorithm 4. In line 3, given  $p$  pieces in  $Q$ , the ending index  
 1579 of the last piece (i.e., the  $p^{\text{th}}$  piece) will range from  $(p \cdot L_{\text{gmin}}^Q)$ , given all the  $p$  pieces are  
 1580 in minimum length  $L_{\text{gmin}}^Q$ , to  $\min(p \cdot L_{\text{gmax}}^Q, m)$ , given all the  $p$  pieces are in maximum  
 1581 length  $L_{\text{gmax}}^Q$ .

1582 In line 4, we enumerate for all the allowed lengths  $L^Q$ . For the segment with length  
 1583  $L^Q$  in  $Q$ , the length  $L^C$  of the corresponding aligned segment in  $C$  will have a range from

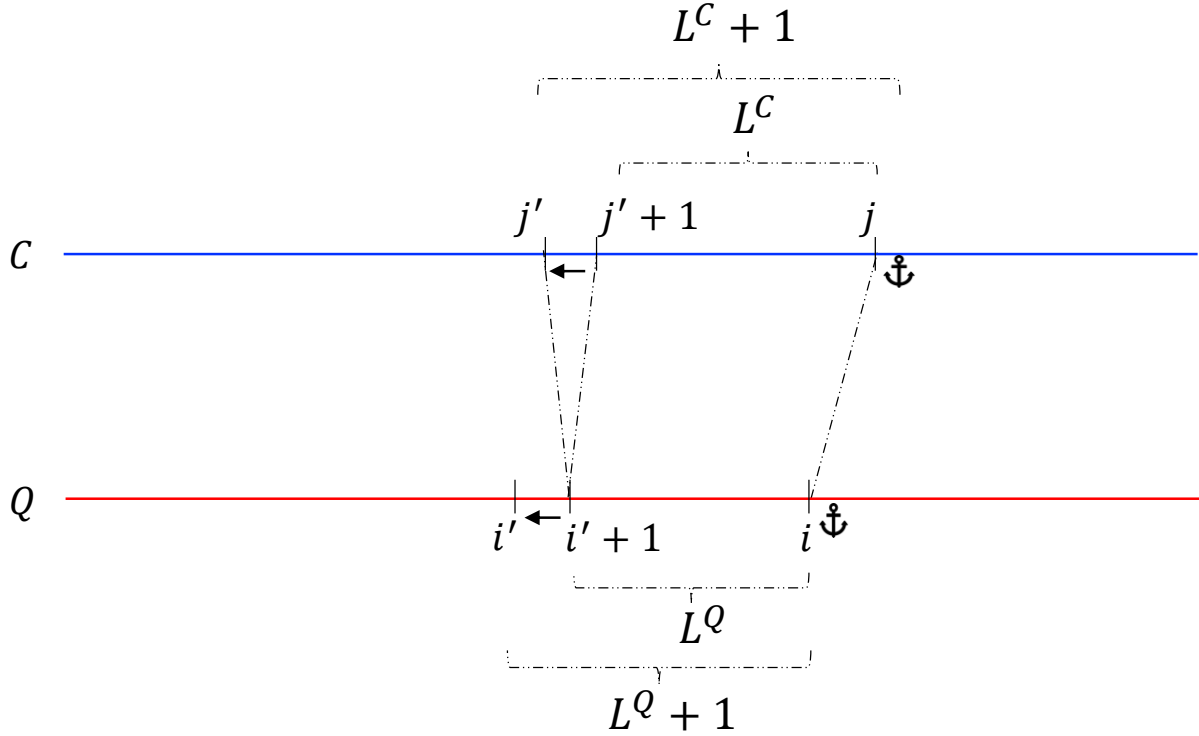


Figure 4.7: Relationship of  $L_Q$  and  $L_C$ .

$L_{\min}^C$  to  $L_{\max}^C$ , as defined in lines 7–8, such that the ratio of  $L^Q$  and  $L^C$  would be bounded by  $l$ . Because  $L^Q$  and  $L^C$  increase in line 4 and line 14, and the  $i$  and  $j$  are fixed by the outer loop, in line 3 and line 13, respectively, the  $i'$  and  $j'$  decrease correspondingly. It is visualized in Figure 4.7. A segment in  $Q$  with ending index  $i$  and starting index  $i' + 1$  would be compared to a set of segments in  $C$ , all of which have a fixed end at  $j$  and a decreasing starting index, starting at  $j' + 1$ . For example, the starting index of the first segment with being compared is  $j' + 1$ , which has length  $L^C$ , and that of the second segment is  $j'$ , which has length  $L^C + 1$ , as in Figure 4.7.

In line 18, we terminate the current iteration if there are no previously valid segment pairs (i.e.,  $dist_{\text{prev}} = \infty$ ).

In line 22, if the accumulated cost  $dist_{\text{prev}}$  exceeds the current best so far, we stop the current iteration as the resulting ( $dist_{\text{prev}} + dist_{\text{seg}}$ ) is guaranteed to be greater than the current best so far, which is stored in  $D[i, j, p]$ .

To be consistent with the result of using the lower bound speedup technique, which will be introduced later, we compute the DTW in the reverse manner in line 33. Due to the nearest neighbor interpolation,  $\text{DTW}_r(Q'^L, C'^L)$  may not equal to  $\text{DTW}_r(\text{rev}(Q')^L, \text{rev}(C')^L)$ .

In line 35, we also save the pairs  $(i', j')$  that serve as cutting points between segments to obtain the segmentation result.

**Parallel computing:** We observe that the recurrence relation for the state  $D[i, j, p]$  at stage  $p$  depends exclusively on the states computed at stage  $p - 1$ , as shown in Equa-

1604 tion 4.15. There are no stage dependencies over indices  $i$  and  $j$ . It allows us to parallelize  
 1605 the loops over indices  $i$  and  $j$  on lines 3 and 13. In the following experimental section, we  
 1606 distribute the i-loop iterations (i.e., line 3 in Algorithm 4, which is colored in blue) across  
 1607 available threads only because there are already sufficient iterations from the i-loop to  
 1608 fill the available threads. There are  $\left(\min(p \cdot L_{\text{gmax}}^Q, m) - (p \cdot L_{\text{gmin}}^Q) + 1\right)$  iterations from  
 1609 the i-loop. The parallel execution of the  $i$ -loop is implemented by `prange` in Numba in  
 1610 Python.

1611 **Early Abandoning in nearest neighbor search:** To accelerate the nearest neighbor  
 1612 search (or top- $k$  search) for a query  $Q$  on a candidate set, we employ an early abandoning  
 1613 strategy. It prunes the search branch within the PSD computation of a specific candidate  
 1614  $C$  as soon as the result corresponding to this search branch is determined to be sub-  
 1615 optimal. We maintain a variable,  $\text{bsf}$  (best-so-far), which represents the minimum final  
 1616 distance among the candidates processed with  $Q$  so far.  $\text{bsf}$  serves as an upper-bound  
 1617 threshold. During the evaluation of a new candidate  $C$ , we monitor the accumulated  
 1618 partial distance,  $\text{dist}_{\text{prev}}$ . If  $\text{dist}_{\text{prev}}$  exceeds  $\text{bsf}$ , the corresponding final distance is guar-  
 1619 anteed to exceed  $\text{bsf}$ . In such cases, the current search branch is immediately terminated.  
 1620 The implementation of this pruning mechanism is detailed in lines 20–21 in Algorithm 4,  
 1621 which are colored in orange. In the case of top- $k$  search, we must maintain the top- $k$   
 1622 final distances and use the  $k$ -th distance as the threshold.

### 1623 Lower bound:

1624 When we use DTW as a routine in PSD, the computation of the DTW of the interpo-  
 1625 lated segment can be sped up by computing  $\text{LB}_{\text{Shen}}$  for the lower bound. From Figure 4.7,  
 1626 we observe that a segment of  $Q$ , with length  $L^Q$ , is compared to a set of growing seg-  
 1627 ments of  $C$ , with a fixed end at  $j$ . The length of these segments is from  $L_{\text{min}}^C$  to  $L_{\text{max}}^C$ ,  
 1628 as indicated in line 14 in Algorithm 4. They share the same suffix with length  $L_{\text{min}}^C$ . It  
 1629 encourages us to view both  $Q$  and  $C$  reversely. The reversed segments are denoted as  $Q'$   
 1630 and  $C'$ , as in lines 6 and 16 in Algorithm 4. In this reversed view, they share the same  
 1631 prefix with length  $L_{\text{min}}^C$ . Hence, we construct an indexed collection  $\tilde{\mathbb{Q}}$  for  $Q'$  with the  
 1632 maximum length of the segments being compared in  $C$ , which is  $L_{\text{max}}^C$ , as in lines 10–12.

1633 In lines 24–27, we first compute the lower bound between  $Q'$  and the shortest segment  
 1634 of  $C$ . We add the minimum possible contribution of each  $c'$  to the distance contributed  
 1635 by the first alignment, which is  $lb = (c'_1 - q'_1)$ . For the lower bound of the subsequent  
 1636 segments, we compute them incrementally in line 29. Because the last point of segment  
 1637  $C'$  must map to the last point of  $Q'$ , we further tighten the lower bound by using the last  
 1638 alignment in line 30 instead.

1639 Furthermore, we can reduce the computational overhead of constructing the sorted  
 1640 reaches  $\tilde{\mathbb{q}}_k$  (lines 9–12). As illustrated in Figure 4.7, the segment of  $Q$  involved in the  
 1641 comparison grows incrementally. Since the reversed versions of these segments share a  
 1642 common prefix, the sorted reaches  $\tilde{\mathbb{q}}_k$  computed for a segment  $Q'$  of length  $L^Q$  can be

---

**Algorithm 5** Replace lines 3 to 9 in Algorithm 5 to reuse the computed sorted reaches  $\tilde{q}_k$ .

---

```

1:  $r'_{\text{cache}} \leftarrow -1$ 
2: for  $i \leftarrow (p \cdot L_{\text{gmin}}^Q)$  to  $\min(p \cdot L_{\text{gmax}}^Q, m)$  do
3:   for  $L^Q \leftarrow L_{\text{gmin}}^Q$  to  $L_{\text{gmax}}^Q$  do
4:      $i' \leftarrow i - L^Q$ 
5:      $Q' \leftarrow \text{rev}(Q(i' + 1 : i))$ 
6:      $L_{\text{min}}^C \leftarrow \max(L_{\text{gmin}}^C, \lceil L^Q/l \rceil)$ 
7:      $L_{\text{max}}^C \leftarrow \min(\lfloor L^Q/l \rfloor, L_{\text{gmax}}^C)$ 
8:      $r' \leftarrow r \times \max(L^Q, L_{\text{max}}^C)$ 
9:     if  $r'_{\text{cache}} = r'$  then
10:      for  $k \leftarrow 1$  to  $L_{\text{max}}^C$  do
11:        if  $k \leq |Q'|$  then
12:           $e_{\text{prev}} \leftarrow \min(\lfloor kl \rfloor + r', L^Q - 1)$ 
13:           $e_{\text{new}} \leftarrow \min(\lfloor kl \rfloor + r', L^Q)$ 
14:          if  $e_{\text{new}} > e_{\text{prev}}$  then
15:             $\tilde{q}_k \leftarrow \tilde{q}_k \cup q'_{e_{\text{new}}}$ 
16:        else
17:           $q_k \leftarrow (q'_{\max(1, \lceil k/l \rceil - r')}, \dots,$ 
18:           $q'_{\min(\lfloor kl \rfloor + r', L^Q)})$  ▷  $L^Q$  equals to  $|Q'|$ .
19:        else
20:          for  $k \leftarrow 1$  to  $L_{\text{max}}^C$  do
21:             $q_k \leftarrow (q'_{\max(1, \lceil k/l \rceil - r')}, \dots,$ 
22:             $q'_{\min(\lfloor kl \rfloor + r', L^Q)})$ 
23:             $\tilde{q}_k \leftarrow \text{sort}(\tilde{q}_k)$ 
 $r_{\text{cache}} \leftarrow r'$ 

```

---

reused to compute those for the subsequent segments. This optimization is detailed in 1643  
Algorithm 5, with the new components highlighted in blue. It is important to note that 1644  
because  $r'$  is a function of  $L^Q$ , and the construction of  $\tilde{q}_k$  depends on  $r$ , reuse is limited 1645  
to cases where  $r'$  remains constant. We construct reaches  $\tilde{q}_k$  from the sketch in lines 1646  
20–22 and keep track of the  $r'$  used for construction in line 23. If  $r'$  remains constant, 1647  
we can use previously computed reaches  $\tilde{q}_k$  to compute the new set of reaches  $\tilde{q}_k$ . Since 1648  
the ending index of reaches depends on  $\min(\lfloor kl \rfloor + r', L^Q)$ , we need to check whether we 1649  
have a new ending index when  $L^Q$  increases. If the ending index has been changed, we 1650  
need to add the new data points  $q'_{e_{\text{new}}}$  to the sorted sequence  $\tilde{q}_k$ , as in line 15. 1651

$L_{\text{max}}^C$  depends of  $L^Q$ . If  $L_{\text{max}}^C$  increase because  $L^Q$  increase, we construct the new reach 1652  
 $\tilde{q}_k$  and sort it in lines 16–18. 1653

### **1654 4.4.3 Guided Distance**

1655 For faster computation, one would want to use a distance measure with linear complexity,  
1656 such as ED, as the base measure for PSD. While PSED is effective for identifying phase-  
1657 scaling changes, certain applications require capturing complex properties within those  
1658 segments that ED cannot handle. There are two ways to address it. One approach is  
1659 to use an alternative distance measure that captures these complex properties as the  
1660 base distance for computing the PSD, such as DTW. But PSDTW is slower than PSED.  
1661 The other approach is to use the segmentation result returned by PSED. To address  
1662 this, we propose a two-stage framework in which PSED-derived segmentation guides the  
1663 application of advanced distance metrics  $M$ . Let  $\mathcal{P}^* = \{(i_1, j_1), (i_2, j_2), \dots, (i_{P+1}, j_{P+1})\}$   
1664 be the set of optimal cut points on  $Q$  and  $C$  obtained by minimizing the PSED. We  
1665 utilize  $\mathcal{P}^*$  to partition both series into  $P$  aligned pairs of segments. The final distance,  
1666 denoted as  $M^{\text{PSED}}$ , is calculated by summing the distances of these pairs using a target  
1667 metric  $M$ :

$$M^{\text{PSED}}(Q, C) = \sum_{p=1}^P M(Q_p^L, C_p^L) \quad (4.16)$$

1668 , where  $Q_p = Q(i_p + 1 : i_{p+1})$  and  $C_p = C(j_p + 1 : j_{p+1})$ .

## **1669 4.5 Experiments**

1670 We evaluate the performance of our proposed distance measure framework, PSD, via its  
1671 two instantiations: PSED and PSDTW. Specifically, we focus on a query retrieval task  
1672 in which the query exhibits piecewise-scaled distortion, that is, distinct phases of the  
1673 query exhibit different expression rates relative to the target in the candidate dataset.  
1674 Our objective is to verify whether PSD achieves invariance to these multiple scaling  
1675 distortions, thereby allowing it to correctly retrieve the most similar candidate. We detail  
1676 the experimental setup in Section 4.5.1 and present the results in Section 4.5.2. The code  
1677 and data are available at <https://github.com/colemanyu/k-scaling-factor-dtw>.

### **1678 4.5.1 Experimental Setup**

1679 We utilize the GunPoint dataset, originally released in 2003 [68], as the running example.  
1680 Widely regarded as the “iris” dataset of the time series community [69], it has appeared  
1681 in over one thousand publications. Beyond its ubiquity, the dataset addresses a critical  
1682 distinction: misinterpreting the act of aiming a gun as merely pointing a finger could  
1683 have life-threatening consequences.

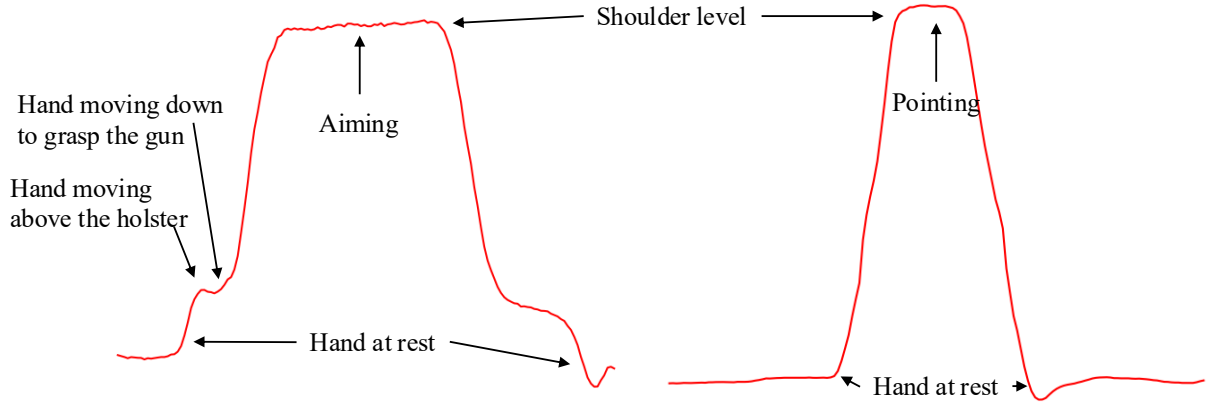


Figure 4.8: Visualization of the GunPoint dataset. Left (Right): A time series of the “Gun” (“Point”) scenario. Critical periods, such as “Aiming”, are annotated.

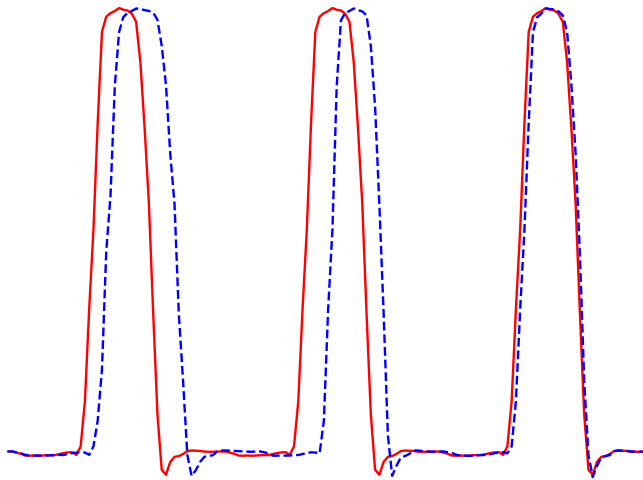


Figure 4.9: The red solid time series shows an instant in the target set. The blue dashed time series shows an instant in the query set.

The dataset contains two classes: “Gun” and Point”. Actors aim at an eye-level target 1684 using either a replica gun or their index finger, as illustrated in Figure 4.8. The resulting 1685 time series represent the X-axis centroid of the actor’s right hand. Each action lasts 1686 for 5 seconds, with the pointing/aiming phase occurring for approximately one second. 1687 Recorded at 30 fps, each sample consists of 150 data points. The dataset comprises 50 1688 training and 150 test series, all of length 150. 1689

A key limitation of the original dataset is the assumption that every action lasts 1690 exactly 5 seconds. In reality, actors perform actions at varying speeds. If an actor is 1691 asked to perform the action three times continuously in a row, we are likely to observe a 1692 time series containing three phases, each with a unique rate. The first phase should take 1693 longer than subsequent phases because it is the first time the action is performed. This 1694 phenomenon is depicted in Figure 4.9, where the red curve represents an ideal case that 1695 consists of three identical phases (i.e., identical rate), while the blue curve represents a 1696

1697 realistic scenario with varying rates. The first action is slower than the second action.  
1698 Consequently, retrieving such patterns requires assigning different scaling factors to each  
1699 phase to accommodate the phase-specific rates.

1700 We now describe the procedure for generating the target and query sets for the re-  
1701 trieval task. To construct the target set, we concatenate  $P$  repetitions of each time series  
1702 instance from the source dataset. To ensure a fair comparison, we constrain the resulting  
1703 time series to match the original length  $n$ . This is achieved by rescaling each phase to a  
1704 length of  $n/P$  prior to concatenation. Note that we must handle remainders to ensure  
1705 that the final time series length is exactly  $n$ . An example of such a target (where  $P = 3$ )  
1706 is depicted by the red solid line in Figure 4.9.

1707 To construct the query set, we first determine the specific lengths for the  $P$  segments.  
1708 Starting with an expected mean length of  $n/P$ , we define the minimum segment length  
1709 as  $L_{\min} = (n/P)\sqrt{l}$  and the maximum as  $L_{\max} = (n/P)\sqrt{l}$ . This formulation ensures  
1710 that the ratio of the lengths of any two segments is bounded by  $l$ . We then generate  $P$   
1711 random integers within  $[L_{\min}, L_{\max}]$  subject to the constraint that their sum is exactly  $n$ .  
1712 Finally, we construct the query by rescaling  $P$  copies of the source time series to these  
1713 generated random lengths and concatenating them. The resulting time series maintains  
1714 the original length  $n$ . An example of such a query (where  $P = 3$ ) is depicted by the blue  
1715 dashed line in Figure 4.9.

1716 Both the query and target sets are derived from the same source dataset. Conse-  
1717 quently, the ground truth target for a given query is defined as the instance in the target  
1718 set that is generated from the same underlying source time series.

Table 4.1: Details of the ten datasets for the experiments

Name	Type	Train/Test?	Size	Class	Length
SonyAIBORobotSurface1	Sensor	Test	601	2	70
ECG200	ECG	Train	100	2	96
MedicalImages	Image	Train	381	10	99
CBF	Simulated	Train	30	3	128
SwedishLeaf	HAR	Train	500	15	128
Plane	Sensor	Train	105	7	144
PowerCons	Device	Train	180	2	144
GunPoint	HAR	Train	50	2	150
Adiac	Image	Train	390	37	176
Epilepsy	HAR	Train	137	4	207

1719 Table 4.1 details the additional datasets used in this study. The column labeled  
1720 “Train/Test?” specifies which split was employed as the source dataset.

1721 In our experiments, we set the warping window parameter  $r = 0.1$ , as suggested in  
1722 the literature. The algorithms were implemented in Python. We utilized the `aeon` [70]

library to obtain the baseline distance measures. All experiments were conducted on a 1723  
workstation equipped with an Intel Xeon Gold 6326 CPU and 256GB of RAM. 1724

### 4.5.2 Experimental Results

1725

We employ Top- $k$  Accuracy (often referred to as Precision@ $k$  [71]) as the primary evaluation metric. For a single query  $Q$ , this metric indicates whether the correct match is successfully retrieved within the top  $k$  candidates: 1726  
1727  
1728

$$P@k(Q) = \begin{cases} 1 & \text{if the ground truth is in the top-}k \text{ results} \\ 0 & \text{otherwise} \end{cases} \quad (4.17)$$

To determine the top- $k$  results, we compute the distance between  $Q$  and every time series in the target set, generating a distance profile of length equal to the dataset size. 1729  
1730  
1731  
1732  
1733 The top- $k$  results correspond to the  $k$  instances with the smallest distances in this profile. Finally, we evaluate the overall performance by computing the mean Top- $k$  Accuracy across the entire query set  $\mathcal{D}$ : 1732

$$\overline{P@k} = \frac{\sum_{Q \in \mathcal{D}} P@k(Q)}{|\mathcal{D}|} \quad (4.18)$$

We choose  $k \in \{1, 3\}$ .  $k = 1$  refers to the exact retrieval.  $k = 3$  give some tolerance for the retrieval. 1734  
1735

Table 4.2: The accuracy comparison for eight distance measures of the GunPoint dataset

$P$	$l$	ED		DTW [2]		ADTW [10]		DDTW [4]		shapeDTW [6]		WDDTW [5]		WDTW [5]		PSED		PSDTW	
		$P@1$	$P@3$	$P@1$	$P@3$	$P@1$	$P@3$	$P@1$	$P@3$	$P@1$	$P@3$	$P@1$	$P@3$	$P@1$	$P@3$	$P@1$	$P@3$	$P@1$	$P@3$
2	1.25	0.30	0.56	0.82	1.00	0.54	0.84	0.84	0.92	<u>0.96</u>	1.00	0.88	0.96	0.82	0.98	<b>0.98</b>	1.00	0.86	1.00
	1.50	0.14	0.36	0.88	1.00	0.38	0.64	0.78	0.94	<b>1.00</b>	1.00	0.80	0.92	0.88	0.96	<b>1.00</b>	1.00	<u>0.96</u>	1.00
	1.75	0.16	0.34	0.82	1.00	0.38	0.66	0.64	0.80	0.90	1.00	0.66	0.80	0.82	0.96	<b>1.00</b>	1.00	<u>0.94</u>	1.00
	2.00	0.12	0.24	0.84	0.98	0.34	0.66	0.72	0.88	<u>0.96</u>	1.00	0.68	0.86	0.82	0.98	<b>1.00</b>	1.00	<u>0.96</u>	1.00
3	1.25	0.30	0.50	0.84	0.92	0.70	0.88	0.80	0.92	<b>0.96</b>	0.98	0.84	0.94	0.86	0.98	<u>0.94</u>	1.00	0.88	0.96
	1.50	0.10	0.28	0.84	0.96	0.60	0.78	0.66	0.86	<u>0.90</u>	1.00	0.72	0.86	0.84	0.98	<b>0.96</b>	1.00	0.86	0.96
	1.75	0.10	0.28	<u>0.88</u>	1.00	0.42	0.78	0.72	0.88	0.76	0.94	0.74	0.88	<u>0.88</u>	1.00	<b>1.00</b>	1.00	<u>0.88</u>	0.98
	2.00	0.02	0.12	<u>0.86</u>	0.94	0.38	0.52	0.60	0.78	0.70	0.94	0.60	0.80	0.82	0.92	<b>0.98</b>	1.00	<u>0.86</u>	0.98
4	1.25	0.34	0.50	0.70	0.86	0.68	0.88	0.60	0.78	0.70	0.90	0.64	0.80	0.70	0.86	<b>0.86</b>	0.94	<u>0.72</u>	0.88
	1.50	0.22	0.38	0.64	0.80	0.60	0.92	0.52	0.64	0.68	0.90	0.52	0.66	0.64	0.82	<b>0.86</b>	0.98	<u>0.72</u>	0.82
	1.75	0.16	0.30	0.72	0.92	0.56	0.80	0.60	0.78	0.56	0.80	0.56	0.80	0.70	0.88	<b>0.92</b>	1.00	<u>0.80</u>	0.94
	2.00	0.06	0.12	0.58	0.78	0.50	0.72	0.46	0.64	0.50	0.82	0.50	0.64	0.56	0.82	<b>0.88</b>	0.98	<u>0.64</u>	0.88

**Results of GunPoint dataset:** We utilize the GunPoint dataset to evaluate how the parameters  $P$  and  $l$  affect the ability of PSD to achieve invariance under piecewise scaling. 1736  
1737  
1738  
1739  
1740  
1741  
1742 The results are presented in Table 4.2, where the best performance of  $\overline{P@1}$  is highlighted in bold, and the second-best is underlined. We benchmark our method against several state-of-the-art distance measures, including ADTW [10], DDTW [4], shapeDTW [6], WDDTW [5], and WDTW [5]. PSED achieves the highest accuracy, followed closely by PSDTW. We attribute PSED’s superior performance over PSDTW to the specific nature

of the distortions in the query set, that is, the “pure” piecewise scaling distortions. Since  
 the query set exhibits only piecewise scaling distortions, the corresponding segments of the  
 query and target time series differ solely in length (scale). Consequently, the additional  
 flexibility provided by DTW in PSDTW is unnecessary and may inadvertently increase  
 the similarity of incorrect matches, thereby reducing discriminative power relative to the  
 stricter PSED measure. However, PSDTW remains theoretically essential for handling  
 local distortions within the phase. PSDTW applies DTW within the scaled segment,  
 enabling robust alignment across local nonlinearities.

Table 4.3: The accuracy comparison for six PSED-guided distance measures of the Gun-Point dataset

$P$	$l$	DTW <sup>PSED</sup>		ADTW <sup>PSED</sup>		DDTW <sup>PSED</sup>		shapeDTW <sup>PSED</sup>		WDDTW <sup>PSED</sup>		WDTW <sup>PSED</sup>	
		$\overline{P@1}$	$\overline{P@3}$	$\overline{P@1}$	$\overline{P@3}$	$\overline{P@1}$	$\overline{P@3}$	$\overline{P@1}$	$\overline{P@3}$	$\overline{P@1}$	$\overline{P@3}$	$\overline{P@1}$	$\overline{P@3}$
2	1.25	0.86	1.00	0.98	1.00	<b>0.72</b>	0.92	0.98	1.00	<b>0.74</b>	0.96	0.86	1.00
	1.50	0.88	1.00	1.00	1.00	<b>0.60</b>	0.90	<b>0.98</b>	1.00	<b>0.64</b>	0.90	0.92	1.00
	1.75	0.94	1.00	1.00	1.00	0.84	0.94	1.00	1.00	0.86	0.96	0.94	1.00
	2.00	0.98	1.00	1.00	1.00	<b>0.60</b>	0.78	0.98	1.00	<b>0.66</b>	0.80	0.98	1.00
3	1.25	<b>0.82</b>	0.96	0.94	1.00	<b>0.74</b>	0.90	<b>0.92</b>	0.98	<b>0.76</b>	0.90	<b>0.82</b>	0.96
	1.50	0.86	1.00	0.96	1.00	0.72	0.90	0.94	1.00	0.80	0.90	0.88	1.00
	1.75	0.88	1.00	1.00	1.00	<b>0.68</b>	0.90	1.00	1.00	<b>0.70</b>	0.94	0.90	1.00
	2.00	0.86	0.96	0.98	1.00	<b>0.54</b>	0.86	0.96	1.00	0.62	0.86	0.88	0.96
4	1.25	0.74	0.88	0.86	0.94	0.78	0.80	0.80	0.92	0.78	0.82	0.74	0.88
	1.50	0.72	0.84	0.86	0.98	0.68	0.84	0.84	0.96	0.66	0.84	0.72	0.86
	1.75	0.74	0.96	0.92	1.00	<b>0.54</b>	0.90	0.90	1.00	0.56	0.88	0.74	0.96
	2.00	0.66	0.90	0.88	0.98	0.58	0.82	0.88	0.98	0.62	0.80	0.66	0.90

We further investigate whether the segmentation results returned by PSED can serve  
 as a guide to enhance other distance measures. As shown in Table 4.3, this approach  
 generally improves accuracy. The exceptions are highlighted in bold, indicating cases  
 where the segmentation led to worse performance. Notably, in most cases, only DDTW  
 and WDDTW failed to benefit from PSED-guided segmentation. We argue that the  
 performance degradation of DDTW and WDDTW stems from their derivative-based  
 nature. They rely on matching slope or shape features. Consequently, they are highly  
 sensitive to segmentation boundaries. A non-perfect cut that falls within a shape feature  
 segmentizes it, and these features are then destroyed. When the algorithm subsequently  
 attempts to map these features, it fails to find correct correspondences, resulting in high  
 distances.

Figure 4.10 illustrates the runtime performance across varying parameters  $P$  and  $l$ .  
 We evaluate two variants of PSD, PSED and PSDTW, each implemented with three  
 levels of

- 1. `vanilla` (i.e., Basic implementation)
- 2. `parallel_bsf` (i.e., With parallelization with Best-So-Far early abandoning)

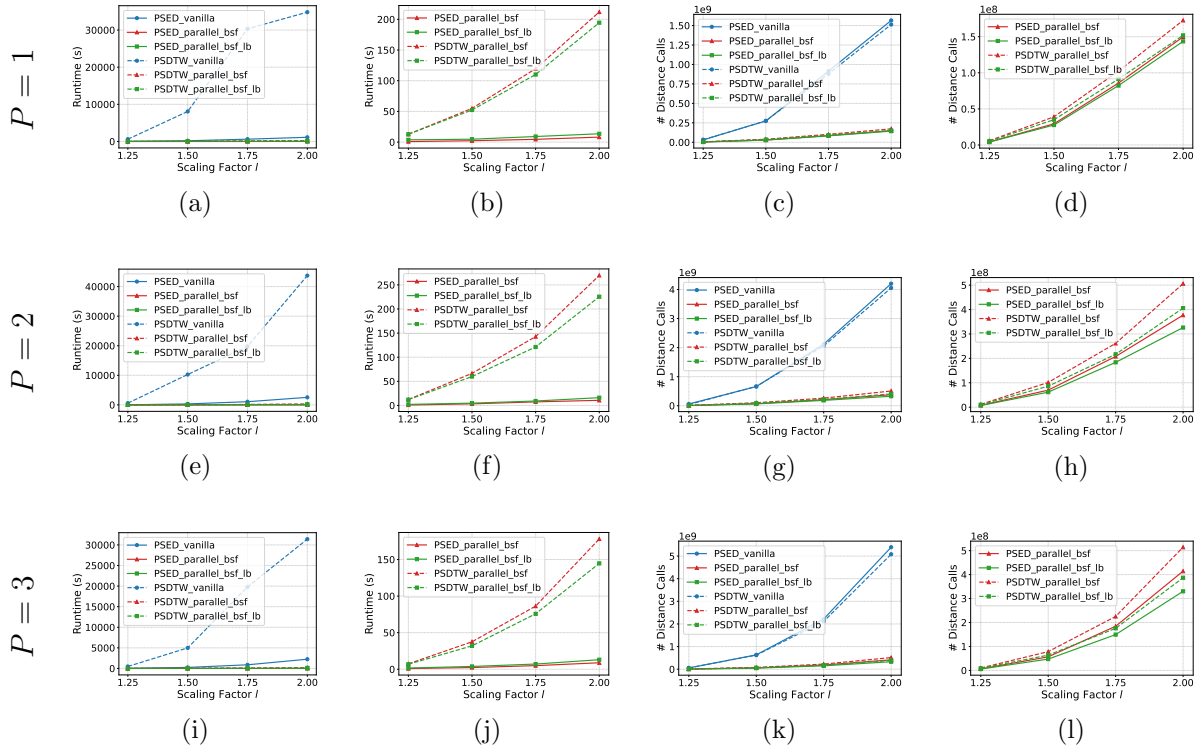


Figure 4.10: Runtime and number of distance calls comparison of GunPoint dataset. (a)-(d)  $P = 1$ , (e)-(h)  $P = 2$ , (i)-(l)  $P = 3$ .

### 3. parallel\_bsf\_lb (i.e., Incorporating lower bound pruning)

1767

This yields a total of six methods. The figure is organized into four columns plotted against the scaling factor  $l$ . The rows refer to the number of pieces  $P$ . The first and third columns display the running time and the number of distance calculations, respectively, for all six methods. To better visualize the performance differences among the efficient implementations, the second and fourth columns omit the `vanilla` baselines and focus exclusively on the four optimized variants. 1769  
1770  
1771  
1772  
1773

The results indicate that `vanilla_PSDTW` is orders of magnitude slower than the other approaches, whereas the optimized methods operate within a similar performance range. 1774  
1775 As anticipated, the computation time for all methods increases with the scaling factor 1776  $l$ . The fourth column confirms that the lower bounding strategy effectively reduces the 1777 number of distance calculations (pruning power). However, the second column reveals 1778 a critical trade-off in actual runtime. While the lower bound successfully accelerates 1779 PSDTW, it actually slows down PSED. This suggests that for the computationally lighter 1780 ED, the overhead of calculating the lower bound outweighs the time saved by pruning. 1781 Overall, the results demonstrate that PSED is significantly faster than PSDTW. 1782

### Results of the ten datasets:

For the remaining nine datasets, we fix the parameters at  $P = 3$  and  $l = 1.5$ . We 1784 have the following findings from the previous experiment: 1785

Table 4.4: The accuracy comparison for eight distance measures of the ten datasets

Dataset	ED		DTW		ADTW		DDTW		shapeDTW		WDDTW		WDTW		PSED	
	P@1	P@3	P@1	P@3	P@1	P@3	P@1	P@3	P@1	P@3	P@1	P@3	P@1	P@3	P@1	P@3
SonyAIBORobotSurface1	0.04	0.08	0.51	0.63	<u>0.60</u>	0.74	0.45	0.57	0.20	0.29	0.45	0.58	0.51	0.64	<b>0.67</b>	0.77
ECG200	0.12	0.20	0.70	0.81	<u>0.78</u>	0.83	0.60	0.74	0.59	0.76	0.59	0.73	0.70	0.80	<b>0.81</b>	0.88
MedicalImages	0.08	0.19	0.63	0.78	0.69	0.85	0.52	0.68	0.57	0.75	0.51	0.68	0.62	0.78	<b>0.76</b>	0.88
CBF	0.53	0.67	0.83	1.00	<u>0.90</u>	1.00	0.73	0.87	0.73	0.90	0.77	0.90	<u>0.90</u>	1.00	<b>1.00</b>	1.00
SwedishLeaf	0.07	0.12	0.82	0.92	<u>0.84</u>	0.93	0.70	0.83	0.78	0.91	0.69	0.83	0.83	0.92	<b>0.97</b>	0.99
Plane	0.09	0.14	0.50	0.74	<u>0.59</u>	0.78	0.38	0.64	0.53	0.79	0.37	0.61	0.49	0.75	<b>0.75</b>	0.93
PowerCons	0.26	0.43	0.77	0.98	<b>0.80</b>	1.00	0.77	0.98	0.77	0.99	0.77	0.99	0.77	0.99	<b>0.80</b>	1.00
GunPoint	0.10	0.28	<u>0.84</u>	0.96	0.60	0.78	0.66	0.86	0.90	1.00	0.72	0.86	<u>0.84</u>	0.98	<b>0.96</b>	1.00
Adiac	0.01	0.02	<u>0.37</u>	0.50	0.12	0.21	0.32	0.42	0.27	0.41	0.31	0.41	0.36	0.50	<b>0.57</b>	0.71
Epilepsy	0.18	0.26	0.74	0.88	<u>0.80</u>	0.91	0.65	0.82	0.38	0.47	0.58	0.79	0.70	0.83	<b>0.83</b>	0.91

Table 4.5: The accuracy comparison for six PSED-guided distance measures of the ten datasets

Dataset	DTW <sup>PSED</sup>		ADTW <sup>PSED</sup>		DDTW <sup>PSED</sup>		shapeDTW <sup>PSED</sup>		WDDTW <sup>PSED</sup>		WDTW <sup>PSED</sup>	
	P@1	P@3	P@1	P@3	P@1	P@3	P@1	P@3	P@1	P@3	P@1	P@3
SonyAIBORobotSurface1	0.53	0.64	0.64	0.76	<b>0.37</b>	0.53	0.65	0.76	<b>0.38</b>	0.53	0.53	0.65
ECG200	0.73	0.84	0.80	0.88	<b>0.54</b>	0.68	0.81	0.88	<b>0.53</b>	0.69	0.73	0.84
MedicalImages	0.66	0.78	0.76	0.88	0.51	0.69	0.74	0.88	0.51	0.70	0.66	0.79
CBF	0.90	1.00	0.93	1.00	0.73	0.93	0.93	0.97	<b>0.70</b>	0.93	0.90	1.00
SwedishLeaf	0.82	0.92	0.97	0.99	0.72	0.87	0.97	0.99	0.73	0.88	<b>0.82</b>	0.92
Plane	0.60	0.80	0.75	0.94	0.50	0.67	0.74	0.90	0.50	0.69	0.59	0.80
GunPoint	0.86	1.00	0.96	1.00	0.72	0.90	0.94	1.00	0.80	0.90	0.88	1.00
PowerCons	0.78	0.99	0.79	1.00	0.79	1.00	0.79	1.00	0.79	1.00	0.78	1.00
Adiac	<b>0.33</b>	0.45	0.57	0.71	<b>0.21</b>	0.34	0.53	0.70	<b>0.20</b>	0.33	<b>0.34</b>	0.45
Epilepsy	0.77	0.88	<b>0.78</b>	0.88	0.66	0.79	0.74	0.89	0.66	0.82	0.80	0.89

1786 1. From Table 4.3, PSED outperformed PSDTW in handling piecewise scaling distortions.

1787 2. From Figure 4.10, the lower bound offered no efficiency gain for PSED.

1789 Hence, we select PSED\_parallel\_bsfs as the representative method for this evaluation.

1790 The accuracy results are presented in Table 4.4, while the results for the PSED-guided  
1791 distance measures are detailed in Table 4.5. Finally, the runtime efficiency for all datasets  
1792 is summarized in Table 4.6. It shows a significant speedup, ranging from 10.10X to  
1793 191.46X.

## 1794 4.6 Concluding Remarks

1795 In this paper, we proposed a novel distance measure framework, Piecewise Scaling Dis-  
1796 tance (PSD), which relaxes the strict assumption of a single uniform scaling factor across  
1797 the entire time series. We presented an exact dynamic programming (DP) algorithm to  
1798 solve this problem. To enhance efficiency and prevent pathological segment alignments,  
1799 we introduced a constraint version, which limits the search space of segment lengths  
1800 based on given scaling factors. To enhance computational efficiency, we integrated two

Table 4.6: The number of distance calls and runtime on PSED\_vanilla and PSED\_parallel\_bsf of the ten datasets

Name	Size	Length	PSED_vanilla	PSED_parallel_bsf	% distance calls pruned	Speed Up
			Time (s)	Time (s)		
SonyAIBORobotSurface1	601	70	697	69	90.40%	10.10X
ECG200	100	96	91	3	91.08%	30.33X
MedicalImages	381	99	2082	40	96.03%	52.05X
CBF	30	128	43	2	75.31%	21.50X
SwedishLeaf	500	128	16601	107	96.24%	155.15X
Plane	105	144	621	6	96.05%	103.50X
PowerCons	180	144	3629	49	82.32%	74.06X
GunPoint	50	150	159	3	89.42%	53.00X
Adiac	390	175	23550	123	96.71%	191.46X
Epilepsy	137	206	13131	336	39.88%	39.08X

optimization techniques for the general PSD framework. In addition, we propose incorporating a lower-bounding strategy to accelerate PSDTW. Our experimental results demonstrate the necessity and effectiveness of PSD when identifying matches between a query  $Q$  and a candidate  $C$  under piecewise scaling distortions.

We outline several directions for future research. First, we aim to develop a lower bound specifically optimized for PSED that can improve actual runtime. Second, while the current PSDTW algorithm requires the number of segments  $P$  to be specified as a hyperparameter, it is preferable for the algorithm to determine this value adaptively. A simple heuristic is to test a range of  $P$  values and select the configuration that yields the minimum distance. Finally, we plan to investigate efficiency improvements for PSDTW. Currently, PSDTW computes dynamic time warping on two growing subsequences after scaling. While techniques for Incremental DTW [72] allow for the reuse of the accumulating cost matrix  $D$  to avoid redundant calculations, applying this to PSDTW is non-trivial. The interpolation performed before DTW fundamentally alters the sequence structure, preventing the straightforward extension of  $D$  (e.g., by appending rows or columns) to reuse the computed  $D$  that is possible in standard DTW.



# Chapter 5

1817

## Leveraging Nearest Neighbors for Time Series Forecasting with Matrix Profile

1818

1819

1820

### 5.1 Introduction

1821

Humans have made predictions since ancient times. In ancient societies, accurate predictions were important to the success of subsistence activities such as hunting, planting, and harvesting. There was a need to predict weather dynamics, such as rainfall and temperature. For example, it is crucial to plant during the period with sufficient rainfall and appropriate temperatures. Our ancestors used divination tools such as turtle shells, wooden blocks (moon blocks), or bones to make predictions. Without doubt, the accuracy was not guaranteed. Even in modern societies, prediction is still essential. Predicting traffic-jam patterns only a few hours ahead can save time by enabling the selection of an alternative route [73]. A wealth could be created by forecasting stock market trends. Predicting the future, also known as time series forecasting, is crucial.

1831

With advances in hardware technologies, we collect enormous amounts of data from diverse sources, such as smart sensors and social media platforms, continuously in the form of time series data. A time series is an ordered sequence of measures, represented in real-valued numbers, at discrete equal-interval timestamps [74]. The vast data collections have created the era of “Big Data”, which provides a wealth of datasets for developing and deploying reliable, robust, data-driven forecasting techniques to discover patterns and extract valuable information [75]. Applications can be found in the financial sector, such as predicting business cycles and stock market movements [76, 73, 77, 78] and the medical field, such as the status of critical patients according to their vital signs [79, 80] and the propagation of diseases such as influenza [78, 81] and COVID-19 [79, 82].

1841

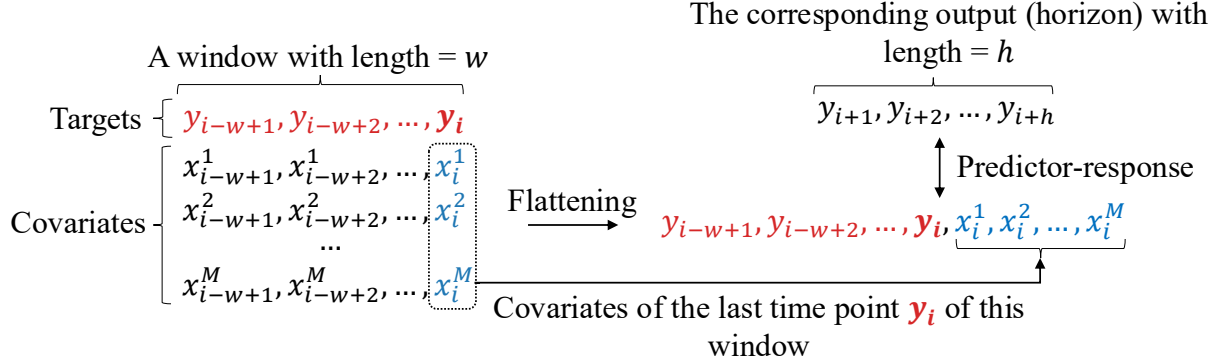


Figure 5.1: Flattening a 2D window of size  $(1+M) \times w$  to a 1D vector of length  $w+M$ . The resulting vector serves as the *predictor* for the regressor. Its expected *response* is the vector of length  $h$ . The regressor learns from this predictor-response pair.

1842     A recent study [1] shows that, in time series classification, a non-parametric, instance-  
 1843     based method, namely nearest-neighbor classifiers (1-NN) and its generalized form  $k$ -NN,  
 1844     with appropriate distance measures, such as Dynamic Time Warping (DTW), despite  
 1845     their simplicity, perform well and are therefore commonly used as benchmarks. In de-  
 1846     tail, when a new instance is to be classified,  $k$ -NN finds its  $k$  nearest neighbors in the  
 1847     training set and returns their majority label among them.  $k$ -NN is considered a lazy  
 1848     learner because the training steps involve only memorizing all the instances verbatim; no  
 1849     higher-level concepts have been learned. In addition, in time series forecasting, a recent  
 1850     study demonstrates that a well-known machine learning baseline, Gradient Boosting Re-  
 1851     gression Tree (GBRT), such as XGBoost, equipped with an appropriate data engineering  
 1852     of the data, can achieve competitive or even superior performance than the deep learning  
 1853     method. In detail, they transform the time series forecasting task into a window-based  
 1854     regression problem, as shown in Figure 5.1. For each training window of length  $w$  with  
 1855     the last time point  $\mathbf{y}_i$ , and its lagged values  $\mathbf{y}_{i-1}, \mathbf{y}_{i-2}, \dots, \mathbf{y}_{i-w+1}$  are concatenated with  
 1856     covariates  $x_i^1, x_i^2, \dots, x_i^M$  to form a *predictor* for a multi-output GBRT. This transfor-  
 1857     mation is called flattening. The corresponding response is the following  $h$  points of  $\mathbf{y}_i$ . It  
 1858     provides a simple, more efficient yet accurate method for time series forecasting.

1859     Moreover,  $k$ -NN has also shown to be a promising method for time series forecast-  
 1860     ing [83]. The  $k$ -NN uses the lagged values of the last time point to form a query  $Q$ .  
 1861     It identifies the  $k$  previous similar subsequences to  $Q$  and uses their immediate subse-  
 1862     quences to predict the immediate subsequence, which is the forecasting window, of  $Q$ .  
 1863     The intuition is that history repeats itself. The previous (historical) subsequences that  
 1864     are similar to  $Q$  can provide a hint about the future of  $Q$ . They are similar, and so are  
 1865     their immediate subsequences. Figure 5.2 depicts this idea. Observe that the immediate  
 1866     subsequence of the right gray box is similar to that of the left gray box. The left gray  
 1867     box is the nearest neighbor of the right gray in the “past”.

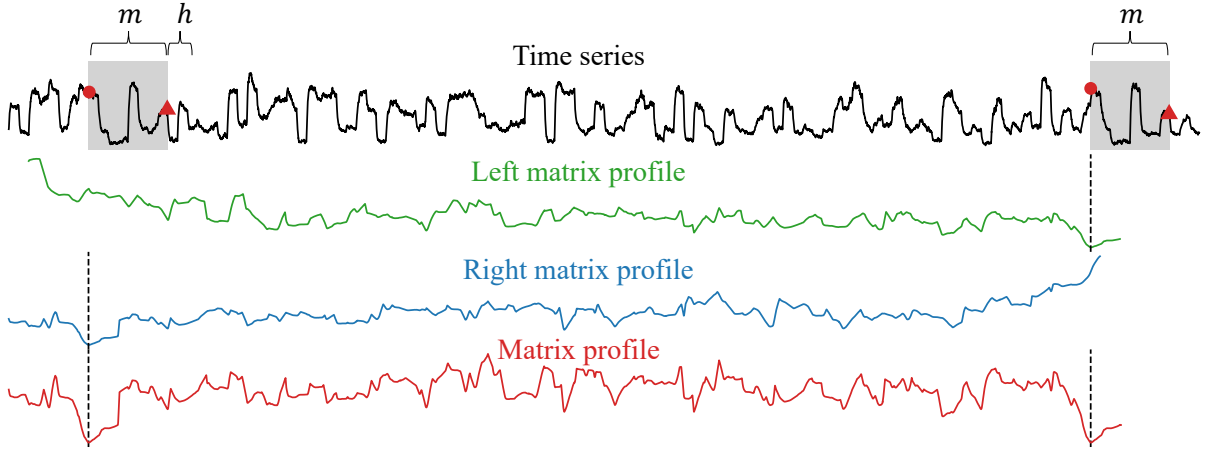


Figure 5.2: The **left** (**right**) matrix profile and the **matrix profile** of a time series. The **matrix profile** shows the distances between each  $m$ -subsequence and its nearest neighbor, where  $m$  is a user-given value. The **left** (**right**) matrix profile shows the same information but is limited to its left (right) nearest neighbor. For a particular  $m$ -subsequence shown by the right gray box, its nearest neighbor is the left gray box, as indicated by the dashed line in the **left matrix profile** and the **matrix profile**. Similarly, the nearest neighbor of the left gray box is the right gray box, as indicated by the dashed line in the **right matrix profile** and the **matrix profile**. The first (last) point in each box is denoted by a red circle (triangle).  $h$  denotes the length of the immediate subsequence of the nearest neighbor. Intuitively, this subsequence should be similar to the immediate subsequence (i.e., future) of the right gray box. To note, the **left** (**right**) matrix profile starts (ends) at a later (earlier) index because the corresponding nearest neighbor with length  $m$  does not exist.

---

**Algorithm 6** The brute force approach to compute Matrix Profile

---

```

1: for  $i \leftarrow 1$  to  $n - m + 1$  do
2:   for  $j \leftarrow 1$  to  $n - m + 1$  do
3:     Compute the z-normalized Euclidean distance between  $t_{i,m}$  and  $t_{j,m}$ .

```

---

Based on these findings, this study proposes a method to improve the performance of 1868 existing forecasters by leveraging information from the nearest neighbors of each subsequence in the target variable. For each time point  $y_i$  of the target variable  $Y$ , a window 1869 of length  $w$  is constructed with  $y_i$  as the last point, then we retrieve the window's historical 1870 nearest neighbors and use their information to create new covariates for the window. 1871 The information includes the similarities between the window and its nearest neighbors, 1872 as well as the immediate subsequences of them. The similarity can be interpreted as a 1873 measure of confidence or weight in using the information from the corresponding nearest 1874 neighbor. The intuition is that, if the similarity of the window and a neighbor is high, 1875 then the future (i.e., immediate subsequence) of the neighbor should also be similar to 1876 the future of the window. The fundamental difference between this study and previous 1877 approaches [84, 83, 85] is that they directly use the subsequent points for prediction, 1878 whereas we use the nearest neighbor information for each subsequence as covariates, 1879 1880

1881 which are used as primitives for other forecasters. We explain this subtle difference by  
1882 Figure 5.2. The previous approaches simply use the information of the nearest neighbors  
1883 of the last look-back window, which consisted of the last time point and its lagged values  
1884 (i.e., the right gray box), for prediction. In contrast, we use the information of the nearest  
1885 neighbors of **all** of the windows.

1886 We use the Matrix Profile [86, 87] to annotate the nearest neighbor for each  $m$ -  
1887 subsequence of a time series  $T$  of length  $n$ . The distance is the z-normalized Euclidean  
1888 distance. It may seem computationally expensive to perform this annotation at first  
1889 glance. Algorithm 6 shows the brute force approach to compute the matrix profile.  
1890 The two for-loops and the computation of z-normalized Euclidean distance, which takes  
1891  $\mathcal{O}(m)$ , indicate that the computational complexity is  $\mathcal{O}(n^2m)$ . The space complexity is  
1892  $\mathcal{O}(n^2)$  because of the pairwise distance of each subsequence with the other subsequence.  
1893 However, the matrix profile can be computed in  $\mathcal{O}(n^2)$  using an exact method, namely  
1894 STOMP [86] or its community-open-sourced version, STUMP [88]. Besides, the running  
1895 time can be further sped up by parallelization for a single machine with multiple compu-  
1896 tation units, such as CPUs or GPUs. The tool also allows us to compute the left matrix  
1897 profile to find the left nearest neighbor of each window. To note, the matrix profile an-  
1898 notates a time series with information about the nearest neighbor of each subsequence,  
1899 including the similarity with its nearest neighbor and its location, as shown in Figure 5.2.

1900 In this study, we make the following contributions:

- 1901 • We are the first to propose leveraging the matrix profile to create meaningful co-  
1902 variates that improve forecaster performance.

1903 The rest of this paper is organized as follows. Section 5.2 presents the related-work.  
1904 In Section 5.3, we introduce the necessary background knowledge, then introduce our  
1905 method. Section 5.4 contains an empirical evaluation. Finally, we conclude this paper  
1906 and provide future work in Section 5.5.

## 1907 5.2 Related Work

1908 Many methods have been developed for time series forecasting. Traditional methods in-  
1909 clude rolling averages (RA), vector auto-regression (VAR) [73, 89], and auto-regressive  
1910 integrated moving averages (ARIMA) [90, 91, 89]. Because of their rigorous statisti-  
1911 cal properties, they have long been the standard. The shortcomings of ARIMA and  
1912 its variants include their high computational cost [73]. In contrast, VAR is arguably  
1913 the most widely used method, particularly in multivariate time series analysis, owing to  
1914 its simplicity. However, most of these traditional approaches have certain limitations.  
1915 They perform well when the data meet specific statistical assumptions, such as station-  
1916 arity [92], which means that the mean and variance of the time series remain constant

over time. It motivates the community to develop machine learning methods, particularly deep learning methods for time series forecasting. Many deep learning models have been proposed, including RNN-based models, CNN-based models, GNN-based models, Transformer-based models, and compound models that incorporate different base models mentioned before [78]. The compound models are promising. For example, RNNs are well suited to capturing long-term dependencies, whereas CNNs are well suited to capturing short-term dependencies. A good way to improve performance is to compound them. For example, LSTnet [73] integrates CNN, RNN, and autoregressive [93] techniques to extract both short-term and long-term patterns. Using the occupancy rate of a freeway as an example [73] to explain these two patterns, the “short-term” patterns refer to the morning peaks against evening peaks, while the “long-term” patterns refer to the workday patterns against weekend patterns. Clearly, a good forecaster needs to capture and distinguish both kinds of patterns. Despite the superior performance deep learning methods have achieved, they tend to be overly complex, opaque, and incur high computational costs compared to traditional techniques.

### 5.3 Method

In this section, we first formulate the time series forecasting problem, followed by the evaluation method. We then explain how to use a Gradient Boosting Regression Tree (GBRT) for forecasting. Subsequently, we discuss how to leverage the nearest neighbors’ information of each subsequence to improve GBRT’s performance. Finally, we discuss how to compute those nearest neighbors using the Matrix Profile.

To begin, we define the data type of interest: time series.

**Definition 10** (Time series). A *time series*  $T = t_1, t_2, \dots, t_n$  is a sequence of real-valued numbers with length  $= n$ .

In Definition 10,  $T$  is a univariate time series where each entry is a scalar number. If each entry is a vector consisting of scalar numbers with size  $> 1$ ,  $T$  is a multivariate time series. A multivariate time series can be regarded as a sequence of vectors. It can also be represented as a vector of univariate time series, where each univariate time series is referred to as a channel. In a dataset with more than one time series, we use  $T_i$  to denote a time series in a dataset with  $N$  time series, where  $1 \leq i \leq N$ .

The local properties of  $T$  can be analyzed through its subsequences.

**Definition 11** (Subsequence). A *subsequence*  $T_{i,m} = t_i, t_{i+1}, \dots, t_{i+m-1} = t_{i:i+m-1}$  of a  $T$  is a sequence that consists of a continuous subset of the entries from  $T$  of length  $m$  starting from  $i$ .

### 1951 5.3.1 Problem Formulation

1952 Time series forecasting is the task of predicting  $h$ -future values  $y_{t+1}, y_{t+2}, \dots, y_{t+h}$  of a  
1953 target  $Y$  at the current time point  $t$ . In this study, there is only one target variable  $Y$ .  $h$  is  
1954 the number of steps we want to predict in the future. The simplest case is one-step-ahead  
1955 forecasting, where  $h = 1$ . The predicted value is denoted as  $\hat{y}_{t+1}$  where the actual value  
1956 is  $y_{t+1}$ . It is preferable to predict multiple points in the future. It is called multi-horizon  
1957 (multi-step) forecasting, where  $h > 1$ . The task of forecasting is encoded in Equation 5.1.

$$\hat{y}_{t+\tau} = f(y_{t-w+1:t}, x_{t-w+1:t}, u_{t-w+1:t+\tau}, \tau) \quad (5.1)$$

1958 where

- 1959 •  $\hat{y}_{t+\tau}$  is a prediction of the target value at  $t + \tau$ , where  $\tau \in \{1, 2, \dots, h\}$ .
- 1960 •  $y_{t-w+1:t}$  are the actual values consisting of the current value  $y_t$  and the lag values  
1961 before it.  $y_{t-i}$  is called the lag of  $i$  or  $i$ -lag.
- 1962 •  $x_t$  are inputs that can only be known historically at time  $t$ .  $x_{t+1}$  is not known at  $t$ .
- 1963 •  $u_t$  are known inputs for all time. For example, the date information such as the  
1964 day of the week or month [92]. Even at  $t$ ,  $u_{t+i}$  where  $1 \leq i \leq \infty$  are known.

1965  $x_t$  and  $u_t$  are called covariates of  $y_t$ . The input of Equation 5.1 is a look-back window  $w$ .

1966 We explain the task of forecasting in terms of Equation 5.1. The forecasting process  
1967 estimates the value of  $y_{t+\tau}$ , denoted by  $\hat{y}_{t+\tau}$  with the aim to minimize the error function,  
1968 typically represented as a function of  $y_{t+\tau} - \hat{y}_{t+\tau}$  for each  $\tau$ . It is obvious that date  
1969 information is useful when the target variable depends on when the measurement is  
1970 taken. For example, if the target variable is the electricity consumption rate, there is a  
1971 clear pattern by month: consumption is higher during the winter and summer months,  
1972 when air conditioners and heaters are used.  $x_t$  provides additional information about the  
1973 state of  $y_t$ . For example, if the target variable is the body temperature, and  $x_t$  tells us  
1974 the severity of the sore throat, we may guess the body temperature will raise tomorrow.

### 1975 5.3.2 Evaluation Method

1976 Given a dataset  $D$  of  $N$  time series  $T_i$ , where  $1 \leq i \leq N$ , we explain how to evaluate the  
1977 performance of a forecaster on  $T_i$ . The error made by the forecaster on  $D$  is simply the  
1978 summation of errors made by the forecaster on each  $T_i$ . We now focus on a single time  
1979 series; hence, we drop the index  $i$ .  $T$  is divided into two subsequences, namely training  
1980 subsequence  $T_{\text{train}}$  and test subsequence  $T_{\text{test}}$ .

1981 In our study, the forecaster is only allowed to train on  $T_{\text{train}}$ . Recall that we are  
1982 predicting the  $h$  future values from the  $w$  values just before them. Hence, we use a

sliding window of length  $w + h$  to generate the  $w$ -predictor- $h$ -response pairs in  $T_{\text{train}}$ , enabling the forecaster to train on them. During the test (evaluation) phase, we do rolling forecasts. We predict based on the ground truth, not results generated from the model. It is used to prevent the accumulation of errors.

This concept is called “Teacher forcing” [94] because the teacher’s values are “force fed” into the forecaster when we “roll” the forecaster on the  $T_{\text{test}}$  [95]. The intuition is that, suppose each question (except the first one) in an exam depends on the answers to the previous questions, rather than simply grading every answer in the end, a teacher would grade (evaluate) the answer once it is given by the student, and provide the correct answer to the student so he can answer the next question based on the correct answer.

To evaluate the forecaster, we used the following three evaluation metrics defined as:

- Root Mean Square Error (RMSE)

$$\text{RMSE} = \sqrt{\frac{1}{n} \sum_{i=1}^n (y_i - \hat{y}_i)^2} \quad (5.2)$$

- Weighted Absolute Percentage Error (WAPE)

$$\text{WAPE} = \frac{\sum_{i=1}^n |y_i - \hat{y}_i|}{\sum_{i=1}^n |y_i|} \quad (5.3)$$

- Mean Absolute Error (MAE)

$$\text{MAE} = \frac{1}{n} \sum_{i=1}^n |y_i - \hat{y}_i| \quad (5.4)$$

where  $n$  is the length of the time series,  $y_i$ ,  $\hat{y}_i$  is ground true value and predicted value, respectively. RMSE and MAE are widely used metrics. MAE can better reflect the actual error situation than RMSE [76]. WAPE was introduced by [96]. By rewriting Equation 5.3 to Equation 5.5, it is more obvious that it is a weighted absolute percentage error.

$$\text{WAPE} = \sum_{i=1}^n w_i \frac{|y_i - \hat{y}_i|}{|y_i|} \quad (5.5)$$

where the weights are given by

$$w_i = \frac{|y_i|}{\sum_{i=1}^n |y_i|} \quad (5.6)$$

For all of them, a lower value is better.

### 2004 5.3.3 Gradient Boosting Regression Tree (GBRT)

2005 Gradient boosting [97] is a boosting algorithm that ensembles a group of weak learners  
2006 (usually decision trees) to make predictions. It sequentially adds learners to an ensemble,  
2007 with each learner connecting its predecessor. It constructs weak learners in a way that  
2008 each learner strategically corrects the predecessor’s mistakes by fitting the new learner  
2009 to the residual errors made by the predecessor [98, 99]. It can be used in classification  
2010 and regression. In this study, we focus on its use in regression. For the usage in regres-  
2011 sion, the model is called “Gradient Boosting Regression Tree (GBRT)”. Some popular  
2012 optimized implementations of gradient boosting are XGBoost [100], CatBoost [101], and  
2013 LightGBM [102]. In this study, we use XGBoost.

2014 In order to apply GBRT into time series forecasting problem, we need to cast the  
2015 input into an appropriate format to input into GBRT. The casting approach is similar to  
2016 successful time-series forecasting models, which reconfigure the time series into windowed  
2017 inputs [90]. Figure 5.1 presents the reconfiguration. For each entry of the target variable  
2018  $y_i$ , we retrieve its  $u_i$ , such as the day information from the calendar. Hence, for each  $y_i$ , it  
2019 is associated with  $x_i$  and  $u_i$ . To simplify the notation, we absorb  $u_i$  into  $x_i$ , and it is called  
2020 the covariates of  $y_i$ . The 2D window, as shown on the left-hand side in Figure 5.1, with  
2021 size  $w \times M$ , where  $M$  is the total number of covariates, is flattened into a 1D array on the  
2022 right-hand side with length  $w + M$ . To note, as suggested in the literature [90], only the  
2023 covariates of the last time-point  $i$  are kept and appended to the final vector. By recon-  
2024 figuration, we obtain the predictor-response pairs for training. In detail, the predictor is  
2025  $y_{i-w+1}, y_{i-w+2}, \dots, y_i, x_i^1, x_i^2, \dots, x_i^M$  where the red part refers to the current target value  
2026  $y_i$  and its lag values, and the blue part refers to the covariates of  $y_i$ . The corresponding  
2027 output is  $y_{i+1}, y_{i+2}, \dots, y_{i+h}$ , with length =  $h$ . We predict the  $h$ -horizon from the  $w$ -look  
2028 back window (i.e.,  $w + M$ -flattened predictor). With this predictor-response formulation,  
2029 the forecasting problem becomes a multi-output regression problem. Standard XGBoost  
2030 cannot return a sequence of predicted values; it only returns a single number [90]. To  
2031 note, a multi-output regression problem is simply a group of single-output regression  
2032 problems. In other words, XGBoost internally simply treats the prediction of  $h$ -steps as  
2033  $h$  individual problems. Hence, the final output is produced by the  $h$  regressors rather  
2034 than by a single model. One may argue that the  $h$  regressors operate individually and  
2035 hence the temporal relationship in the output sequence is lost. However, as the individual  
2036 regressors are trained on the same flattened input, the prediction would still preserve the  
2037 temporal relationship [90].

### 5.3.4 Matrix Profile

2038

**Definition 12** (Distance profile). A *distance profile*  $D_i = d_{i,1}, d_{i,2}, \dots, d_{i,n-m+1}$  of a  $T$  is a vector of the Euclidean distances between a given subsequence  $T_{i,m}$  and each subsequences in  $T$ , where  $d_{i,j}$  is the distance between  $T_{i,m}$  and  $T_{j,m}$ ,  $1 \leq i, j \leq n - m + 1$ .  
2039  
2040  
2041

The distances are measured between z-normalized time series.  
2042

**Definition 13** (Matrix profile). A *matrix profile*  $P = \min(D_1), \min(D_2), \dots, \min(D_{n-m+1})$  of  $T$  is a vector of Euclidean distances between every subsequence  $T_{i,m}$  of  $T$  and its nearest neighbor in  $T$ .  
2043  
2044  
2045

**Definition 14** (Matrix profile index). A *matrix profile index*  $I = I_1, I_2, \dots, I_{n-m+1}$  of  $T$  is a vector of integers, where  $I_i = j$  if  $d_{i,j} = \min D_i$ .  
2046  
2047

**Definition 15** (Left distance profile). A *left distance profile*  $D_i^L = d_{i,1}, d_{i,2}, \dots, d_{i,i-\lceil m/4 \rceil - 1}$  of  $T$  is a vector of Euclidean distances between a given subsequence  $T_{i,m}$  and each subsequence that appears before  $T_{i,m}$ . To note,  $i - \lceil m/4 \rceil - 1$  is the index location of the last eligible subsequence before  $T_{i,m}$  because of the exclusion zone.  
2048  
2049  
2050  
2051

**Definition 16** (Left matrix profile). A *left matrix profile*  $P^L = \min(D_1^L), \min(D_2^L), \dots, \min(D_{n-m+1}^L)$  of  $T$  is a vector of Euclidean distances between every subsequence  $T_{i,m}$  of  $T$  and its nearest neighbor in  $T$  before it.  
2052  
2053  
2054

**Definition 17** (Left matrix profile index). A *left matrix profile index*  $I^L = I_1^L, I_2^L, \dots, I_{n-m+1}^L$  of  $T$  is a vector of integers, where  $I_i^L = j$  if  $d_{i,j} = \min D_i^L$ .  
2055  
2056

## 5.4 Experiments

2057

Table 5.1: Dataset Statistics.  $N$  is the number of time series in the dataset, while  $|T| = n$  is the length of each time series. “rate” refers to the measuring rate.  $w$  is the size of the look-back window.  $h$  is the size of the forecasting window, also known as the forecasting horizon.  $T_{\text{train}}$  is the training subsequence of  $T$ .  $T_{\text{test}}$  is the test subsequence of  $T$ . To note,  $|T_{\text{train}}| + |T_{\text{test}}| = n$ .

Dataset	Data			Forecasting Task		
	$N$	$n$	rate	$w, h$	$ T_{\text{train}} $	$ T_{\text{test}} $
Electricity [103]	70	26,136	hourly	24	25,968	168
Traffic [103]	90	10,560	hourly	24	10,392	168
PeMSD7(M) [103]	228	12,672	/5 mins	9	11,232	1,440
Exchange-Rate [73]	8	7,536	daily	24	6,048	1,488

2058 **5.5 Conclusion and Future work**

2059 **5.5.1 Conclusion**

2060 **5.5.2 Future Work**

2061 **Leveraging nearest neighbors' location information:** It would be beneficial to re-  
2062 trive the nearest neighbors for each subsequence in a specific range with respect to it.  
2063 Real-world applications often require the separation of information of short-term and  
2064 long-term repeating patterns for making accurate predictions [73]. Notably, the matrix  
2065 profile also provides the locations of the nearest neighbors from the matrix profile in-  
2066 dex. Using this location (index) information, we can retrieve the nearest neighbors of  
2067 each subsequence in a specified range with respect to it to find those "short-term" and  
2068 "long-term" patterns.

2069 **Extend to multidimensional case:** This study focuses on univariate time series fore-  
2070 casting, where there is a single target and no exogenous inputs. It only requires us  
2071 to find one-dimensional nearest neighbors. When there are multiple targets or a sin-  
2072 gle target with multiple exogenous inputs, we need to identify multidimensional nearest  
2073 neighbors [104] and leverage their information for forecasting.

2074 **Top- $k$  motifs:** We can use motifs instead of neighbors to receive more stable "future"  
2075 information for each window. Recall that a time series motif is a repeated pattern that  
2076 consists of at least two occurrences. A motif can be considered as a family of nearest  
2077 neighbors A nearest neighbor is a historical occurrence that instantiates this motif. The  
2078 motif captures the ideal behavior. By finding the occurrences of a motif and considering  
2079 their immediate subsequences, we can make a more confident guess about this motif. We  
2080 outline the approach for finding members of a motif<sup>1</sup> Given a subsequence  $A$  in a time  
2081 series  $T$ , we denote the left-hand side of  $A$  in  $T$  as  $T_L$ . We find  $A$ 's nearest neighbor in  
2082  $T_L$ , denoted as  $B$ . They are the two members of a motif  $M$ . We want to identify other  
2083 subsequences in  $T_L$  that belong to  $M$ . We define a threshold  $\theta = r \times \text{ED}(A, B)$ , where  
2084  $r > 1$ . The center  $M_C$  of  $M$  is defined as the average of  $A$  and  $B$ . Then, we compute  
2085 the distance profile between  $M_C$  and  $T_L$ . Any part of the distance profile that is smarter  
2086 than  $\theta$  points to a member of  $M$  in  $T_L$ . These members can then be added to  $M$ . After  
2087 identifying all the members of  $M$  and excluding these members in the next consideration,  
2088 we can find the next left nearest neighbor of  $A$  in  $T_L$ , and repeat the same process for  
2089 finding the next motif. Given a set of immediate subsequences of members (occurrences)  
2090 of  $M$ , we can compute a more stable immediate subsequence (future) associated with  $M$   
2091 by excluding the outliers among them or using the ensemble value, such as the mean or  
2092 median of them, to cancel the noise.

---

<sup>1</sup>The idea has been mentioned in <https://www.cs.ucr.edu/~eamonn/TimeSeriesMotifs/>.

**Identify outliers of immediate subsequences:** When we have a set of immediate 2093 subsequences, we can determine whether an immediate subsequence is an outlier or not 2094 by comparing it with others. We provide a heuristic to identify an outlier as follows. 2095 Recall that the length of a nearest neighbor and its immediate subsequence is  $m$  and  $h$ , 2096 respectively. We concatenate all nearest neighbors into a single long time series  $T'$ . To 2097 establish a clear boundary, we append a NaN value after each of them. It ensures that all 2098 matrix profile computations do not consider subsequences that span multiple neighbors. 2099 Then, we compute a distance profile of  $T'$  to find the nearest neighbor distance  $d_i$  of each 2100 neighbor  $i$ . Let  $S_i$  be the sequence consisting of neighbor  $i$  of length  $m$  and its immediate 2101 subsequence of length  $h$ . The expected nearest neighbor distance of  $S_i$  (found within the 2102 set of all extended sequences) should be proportional to the increase in length:  $d_i \times \frac{m+h}{m}$ . 2103 If the actual nearest neighbor distance of  $S_i$  is greater than  $r' \times (d_i \times (m + h)/m)$  among 2104 the others, where  $r'$  is a user-given value, the immediate subsequence in  $S_i$  is considered 2105 as an outlier. 2106



# Chapter 6

2107

## Conclusion and Future Directions

2108

In this thesis, we contribute to time series analysis by addressing two aspects, with applications in bioinformatics. The first is to frame the prediction of biological sequence problems as time series classification tasks. The second addresses a fundamental limitation in existing time series distance measures.

In the first study, we investigate the prediction of human Dicer cleavage sites. This task is important for the biogenesis of microRNAs (miRNAs). Accurate prediction of Dicer cleavage sites is crucial for elucidating mechanisms of post-transcriptional gene regulation. Computationally, this task is a classification problem. First, we curate the dataset based on existing studies. The resulting datasets are 14-strings. Then, they are transformed into time series. We employ ROCKET-based classifiers for the classification. The main contributions are summarized as follows. We are the first to frame this problem as a multivariate time series classification problem. We introduced nine encoding methods for the transformation. In the transformation, to our surprise, we are the first to use the base-pair probabilities derived from the predicted secondary structure. We employ state-of-the-art time-series classifiers, namely ROCKET-based classifiers. They use random convolutional kernels to generate the summary statistics and then use a simple ridge classifier to generate the final results. Because of the simplicity of the transformation method and the classifiers we adopted, our framework, namely MTSCCleave, is fast. It achieved predictive performance comparable to or even better than deep learning-based state-of-the-art methods. Furthermore, MTSCCleave demonstrated substantial computational efficiency, with speedups ranging from 3.7X to 28.8X relative to existing methods. We carried out perturbation-based experiments to identify the subsequence that are important for the classification. We found that regions near the center of the pre-miRNA secondary structure are most critical for Dicer cleavage site determination. It aligns with the existing study. Future work for this study is as follows. We make use of the predicted secondary structure information to construct the complementary strand and the base pair probability sequence for the input strand. However, there is more than one predicted secondary structure for the given RNA sequence. One future work is to make

2137 use of all potential secondary structures, each with its own pair probability sequence,  
2138 and encode this data into a multivariate time series with more channels. Another area  
2139 for future work is to use interpretable time series classifiers, such as those based on  
2140 time series shapelets. By doing this, we can study which subsequence is critical for  
2141 the definition of the classes, namely “5p cleav”, “5p non-cleav”, “3p leav”, and “3p non-  
2142 cleav” because shapelets serve as the subsequence that has the most discriminating power  
2143 between classes.

2144 The second study develops a new distance measure framework, namely PSD. It aims  
2145 to release a fundamental assumption that the prior studies have overlooked. There is  
2146 only one scaling rate throughout the entire time series. However, there are much data  
2147 that exhibits multiple rates. For example, human motion or music performance. They  
2148 consist of phases. Each phase has its own expression rate. Existing distance measures  
2149 cannot account for such variations. For example, DTW is designed for handling local  
2150 distortions. US assumes that there is only one scaling factor in the whole series. To  
2151 address this, we introduced the Piecewise Scaling Distance (PSD) framework, the first  
2152 of its kind to account for multiple scaling factors. Recall that PSD is agnostic to the  
2153 base measure we used. We can use any existing distance measure as the base measure.  
2154 We studied the two instantiations of it. They are PSED (using Euclidean Distance as  
2155 the base measure) and PSDTW (using DTW as the base measure). We provided an  
2156 exact dynamic programming solution to compute PSD and three general ways to speed  
2157 it up. In particular, we proposed a constrained version of it that limits the search space  
2158 based on allowed segment lengths derived from scaling factor bounds. Besides, we use  
2159 parallel computing and early abandoning to further accelerate it. For PSDTW, due to  
2160 its quadratic complexity, we can further speed it up using lower-bounding techniques.  
2161 Experiments show that PSD, and in particular PSED, perform best when the query  
2162 contains multi-rate distortions, compared with ED, DTW and the other five DTW-based  
2163 methods.

2164 Future works on it are as follows. Currently, the number of segments  $P$  is given by  
2165 users. It is preferable to develop a heuristic or algorithmic approach to automatically  
2166 determine  $P$ . A simple heuristic is to test a range of possible  $P$ . Besides, while we have  
2167 successfully applied a lower bound on PSDTW and accelerated it, the computational  
2168 overhead of calculating a lower bound on PSED outweighs the pruning benefit and makes  
2169 the computation slower eventually. Developing a specialized lower bound for PSED could  
2170 further improve its running time. In addition, some existing works on speeding up DTW  
2171 such as “incremental DTW” can reuse the accumulated cost matrix  $D$ . However, it  
2172 is challenging to apply a similar method to USDTW and PSDTW due to time series  
2173 interpolation.

2174 The third study develops a new method to create covariates for time series data using  
2175 the immediate subsequences of the left nearest neighbor of each forecasting windows. We

have studied the effect of the length of the immediate subsequences on the forecaster. <sup>2176</sup>  
Future work of this study includes finding nearest neighbors in a specific range to capture <sup>2177</sup>  
the short pattern and long pattern, extending the framework to a multivariate time series <sup>2178</sup>  
forecasting task, using motif family instead of simply top- $k$  nearest neighbors, and how <sup>2179</sup>  
to handle the outliers among the immediate subsequences. <sup>2180</sup>



# Bibliography

2181

- [1] M. Middlehurst, P. Schäfer, and A. Bagnall, “Bake off redux: A review and experimental evaluation of recent time series classification algorithms,” *Data Mining and Knowledge Discovery*, vol. 38, no. 4, pp. 1958–2031, Jul. 2024. 2182  
2183  
2184
- [2] H. Sakoe and S. Chiba, “Dynamic programming algorithm optimization for spoken word recognition,” *IEEE Transactions on Acoustics, Speech, and Signal Processing*, vol. 26, no. 1, pp. 43–49, Feb. 1978. 2185  
2186  
2187
- [3] F. Itakura, “Minimum prediction residual principle applied to speech recognition,” *IEEE Transactions on Acoustics, Speech, and Signal Processing*, vol. 23, no. 1, pp. 67–72, Feb. 1975. 2188  
2189  
2190
- [4] E. J. Keogh and M. J. Pazzani, “Derivative Dynamic Time Warping,” in *Proceedings of the 2001 SIAM International Conference on Data Mining (SDM)*, ser. 2191  
2192  
Proceedings. Society for Industrial and Applied Mathematics, Apr. 2001, pp. 1–11. 2193
- [5] Y.-S. Jeong, M. K. Jeong, and O. A. Omitaomu, “Weighted dynamic time warping 2194  
for time series classification,” *Pattern Recognition*, vol. 44, no. 9, pp. 2231–2240, 2195  
Sep. 2011. 2196
- [6] J. Zhao and L. Itti, “shapeDTW: Shape Dynamic Time Warping,” *Pattern Recognition*, vol. 74, pp. 171–184, Feb. 2018. 2197  
2198
- [7] E. Keogh, K. Chakrabarti, M. Pazzani, and S. Mehrotra, “Dimensionality Reduction 2199  
for Fast Similarity Search in Large Time Series Databases,” *Knowledge and 2200  
Information Systems*, vol. 3, no. 3, pp. 263–286, Aug. 2001. 2201
- [8] B.-K. Yi and C. Faloutsos, “Fast Time Sequence Indexing for Arbitrary L<sub>p</sub> Norms,” 2202  
in *Proceedings of the 26th International Conference on Very Large Data Bases*, ser. 2203  
VLDB ’00. San Francisco, CA, USA: Morgan Kaufmann Publishers Inc., Sep. 2204  
2000, pp. 385–394. 2205
- [9] J. Zhao and L. Itti, “Decomposing time series with application to temporal seg- 2206  
mentation,” in *2016 IEEE Winter Conference on Applications of Computer Vision 2207  
(WACV)*, Mar. 2016, pp. 1–9. 2208

- 2209 [10] M. Herrmann and G. I. Webb, "Amercing: An intuitive and effective constraint for  
2210 dynamic time warping," *Pattern Recognition*, vol. 137, p. 109333, May 2023.
- 2211 [11] L. A. Urry, M. L. Cain, S. A. Wasserman, P. V. Minorsky, R. B. Orr, and N. A.  
2212 Campbell, *Campbell Biology*, twelfth ed. New York, NY: Pearson, 2020.
- 2213 [12] B. Alberts, *Molecular Biology of the Cell*, 7th ed. New York: W. W. Norton &  
2214 Company, 2022.
- 2215 [13] W. W. Cohen, *A Computer Scientist's Guide to Cell Biology: A Travelogue from a*  
2216 *Stranger in a Strange Land*. New York, NY: Springer-Verl, 2007.
- 2217 [14] Y. Lee, K. Jeon, J.-T. Lee, S. Kim, and V. N. Kim, "MicroRNA maturation:  
2218 Stepwise processing and subcellular localization," *The EMBO Journal*, vol. 21,  
2219 no. 17, pp. 4663–4670, Sep. 2002.
- 2220 [15] S. Gu, L. Jin, Y. Zhang, Y. Huang, F. Zhang, P. N. Valdmanis, and M. A. Kay,  
2221 "The Loop Position of shRNAs and Pre-miRNAs Is Critical for the Accuracy of  
2222 Dicer Processing In Vivo," *Cell*, vol. 151, no. 4, pp. 900–911, Nov. 2012.
- 2223 [16] Y. Feng, X. Zhang, P. Graves, and Y. Zeng, "A comprehensive analysis of precursor  
2224 microRNA cleavage by human Dicer," *RNA*, vol. 18, no. 11, pp. 2083–2092, Nov.  
2225 2012.
- 2226 [17] I. J. MacRae, K. Zhou, and J. A. Doudna, "Structural determinants of RNA recogni-  
2227 tion and cleavage by Dicer," *Nature Structural & Molecular Biology*, vol. 14,  
2228 no. 10, pp. 934–940, Oct. 2007.
- 2229 [18] F. Ahmed, R. Kaundal, and G. P. Raghava, "PHDcleav: A SVM based method for  
2230 predicting human Dicer cleavage sites using sequence and secondary structure of  
2231 miRNA precursors," *BMC Bioinformatics*, vol. 14, no. 14, p. S9, Oct. 2013.
- 2232 [19] Y. Bao, M. Hayashida, and T. Akutsu, "LBSIZECLEAV: Improved support vector  
2233 machine (SVM)-based prediction of Dicer cleavage sites using loop/bulge length,"  
2234 *BMC Bioinformatics*, vol. 17, no. 1, p. 487, Nov. 2016.
- 2235 [20] P. Liu, J. Song, C.-Y. Lin, and T. Akutsu, "ReCGBM: A gradient boosting-based  
2236 method for predicting human dicer cleavage sites," *BMC Bioinformatics*, vol. 22,  
2237 no. 1, p. 63, Feb. 2021.
- 2238 [21] L. Mu, J. Song, T. Akutsu, and T. Mori, "DiCleave: A deep learning model for  
2239 predicting human Dicer cleavage sites," *BMC Bioinformatics*, vol. 25, no. 1, p. 13,  
2240 Jan. 2024.

- [22] L. Mu and T. Akutsu, “DiCleavePlus: A Transformer-Based Model to Detect Human Dicer Cleavage Sites Within Cleavage Patterns,” *Genes to Cells*, vol. 31, no. 1, p. e70074, 2026. 2241  
2242  
2243
- [23] S. Griffiths-Jones, H. K. Saini, and S. van Dongen, “miRBase: Tools for microRNA 2244  
genomics,” *Nucleic Acids Research*, vol. 36, no. suppl\_1, pp. D154–D158, Jan. 2008. 2245
- [24] T. Xu, N. Su, L. Liu, J. Zhang, H. Wang, W. Zhang, J. Gui, K. Yu, J. Li, and T. D. 2246  
Le, “miRBaseConverter: An R/Bioconductor package for converting and retrieving 2247  
miRNA name, accession, sequence and family information in different versions of 2248  
miRBase,” *BMC Bioinformatics*, vol. 19, no. 19, p. 514, Dec. 2018. 2249
- [25] M. J. Zvelebil, J. O. Baum, and M. Zvelebil, *Understanding Bioinformatics*. New 2250  
York: Garland Science, 2008. 2251
- [26] R. Lorenz, S. H. Bernhart, C. Höner zu Siederdissen, H. Tafer, C. Flamm, P. F. 2252  
Stadler, and I. L. Hofacker, “ViennaRNA Package 2.0,” *Algorithms for Molecular 2253  
Biology*, vol. 6, no. 1, p. 26, Nov. 2011. 2254
- [27] C. C. Aggarwal, *Data Mining: The Textbook*. Cham: Springer International Pub- 2255  
lishing, 2015. 2256
- [28] G. Mendizabal-Ruiz, I. Román-Godínez, S. Torres-Ramos, R. A. Salido-Ruiz, and 2257  
J. A. Morales, “On DNA numerical representations for genomic similarity compu- 2258  
tation,” *PLOS ONE*, vol. 12, no. 3, p. e0173288, Mar. 2017. 2259
- [29] D. Anastassiou, “Genomic signal processing,” *IEEE Signal Processing Magazine*, 2260  
vol. 18, no. 4, pp. 8–20, Jul. 2001. 2261
- [30] T. Rakthanmanon, B. Campana, A. Mueen, G. Batista, B. Westover, Q. Zhu, J. Za- 2262  
karia, and E. Keogh, “Searching and mining trillions of time series subsequences 2263  
under dynamic time warping,” in *Proceedings of the 18th ACM SIGKDD Interna- 2264  
tional Conference on Knowledge Discovery and Data Mining*, ser. KDD ’12. New 2265  
York, NY, USA: Association for Computing Machinery, Aug. 2012, pp. 262–270. 2266
- [31] P. D. Cristea, “Conversion of nucleotides sequences into genomic signals,” *Journal 2267  
of Cellular and Molecular Medicine*, vol. 6, no. 2, pp. 279–303, 2002. 2268
- [32] N. Chakravarthy, A. Spanias, L. D. Iasemidis, and K. Tsakalis, “Autoregressive 2269  
Modeling and Feature Analysis of DNA Sequences,” *EURASIP Journal on Ad- 2270  
vances in Signal Processing*, vol. 2004, no. 1, pp. 1–16, Dec. 2004. 2271
- [33] J. Zhao, X. W. Yang, J. P. Li, and Y. Y. Tang, “DNA Sequences Classification 2272  
Based on Wavelet Packet Analysis,” in *Wavelet Analysis and Its Applications*. 2273  
Springer, Berlin, Heidelberg, 2001, pp. 424–429. 2274

- 2275 [34] T. Holden, R. Subramaniam, R. Sullivan, E. Cheung, C. Schneider, G. T. Jr,  
2276 A. Flamholz, D. H. Lieberman, and T. D. Cheung, “ATCG nucleotide fluctuation  
2277 of *Deinococcus radiodurans* radiation genes,” in *Instruments, Methods, and*  
2278 *Missions for Astrobiology X*, vol. 6694. SPIE, Oct. 2007, pp. 402–411.
- 2279 [35] A. S. Nair and S. P. Sreenadhan, “A coding measure scheme employing electron-  
2280 ion interaction pseudopotential (EIIP),” *Bioinformation*, vol. 1, no. 6, pp. 197–202,  
2281 Oct. 2006.
- 2282 [36] M. Akhtar, J. Epps, and E. Ambikairajah, “On DNA Numerical Representations  
2283 for Period-3 Based Exon Prediction,” in *2007 IEEE International Workshop on*  
2284 *Genomic Signal Processing and Statistics*, Jun. 2007, pp. 1–4.
- 2285 [37] R. Zhang and C.-T. Zhang, “Z Curves, An Intutive Tool for Visualizing and An-  
2286 alyzing the DNA Sequences,” *Journal of Biomolecular Structure and Dynamics*,  
2287 vol. 11, no. 4, pp. 767–782, Feb. 1994.
- 2288 [38] J. A. Berger, S. K. Mitra, M. Carli, and A. Neri, “Visualization and analysis of DNA  
2289 sequences using DNA walks,” *Journal of the Franklin Institute*, vol. 341, no. 1, pp.  
2290 37–53, Jan. 2004.
- 2291 [39] A. Bagnall, J. Lines, A. Bostrom, J. Large, and E. Keogh, “The great time series  
2292 classification bake off: A review and experimental evaluation of recent algorithmic  
2293 advances,” *Data Mining and Knowledge Discovery*, vol. 31, no. 3, pp. 606–660, May  
2294 2017.
- 2295 [40] A. P. Ruiz, M. Flynn, J. Large, M. Middlehurst, and A. Bagnall, “The great multi-  
2296 variate time series classification bake off: A review and experimental evaluation  
2297 of recent algorithmic advances,” *Data Mining and Knowledge Discovery*, vol. 35,  
2298 no. 2, pp. 401–449, Mar. 2021.
- 2299 [41] A. Dempster, F. Petitjean, and G. I. Webb, “ROCKET: Exceptionally fast and  
2300 accurate time series classification using random convolutional kernels,” *Data Mining*  
2301 and *Knowledge Discovery*, vol. 34, no. 5, pp. 1454–1495, Sep. 2020.
- 2302 [42] A. Dempster, D. F. Schmidt, and G. I. Webb, “MiniRocket: A Very Fast (Almost)  
2303 Deterministic Transform for Time Series Classification,” in *Proceedings of the 27th*  
2304 *ACM SIGKDD Conference on Knowledge Discovery & Data Mining*, ser. KDD  
2305 ’21. New York, NY, USA: Association for Computing Machinery, Aug. 2021, pp.  
2306 248–257.
- 2307 [43] C. W. Tan, A. Dempster, C. Bergmeir, and G. I. Webb, “MultiRocket: Multiple  
2308 pooling operators and transformations for fast and effective time series classifica-

tion,” *Data Mining and Knowledge Discovery*, vol. 36, no. 5, pp. 1623–1646, Sep. 2022. 2309  
2310

- [44] A. Dempster, D. F. Schmidt, and G. I. Webb, “Hydra: Competing convolutional 2311  
kernels for fast and accurate time series classification,” *Data Mining and Knowledge 2312  
Discovery*, vol. 37, no. 5, pp. 1779–1805, Sep. 2023. 2313
- [45] B. W. Matthews, “Comparison of the predicted and observed secondary structure 2314  
of T4 phage lysozyme,” *Biochimica et Biophysica Acta (BBA) - Protein Structure*, 2315  
vol. 405, no. 2, pp. 442–451, Oct. 1975. 2316
- [46] J. Gorodkin, “Comparing two K-category assignments by a K-category correlation 2317  
coefficient,” *Computational Biology and Chemistry*, vol. 28, no. 5, pp. 367–374, Dec. 2318  
2004. 2319
- [47] T.-c. Fu, “A review on time series data mining,” *Engineering Applications of Arti- 2320  
ficial Intelligence*, vol. 24, no. 1, pp. 164–181, Feb. 2011. 2321
- [48] C. Rose, B. Guenter, B. Bodenheimer, and M. F. Cohen, “Efficient generation of 2322  
motion transitions using spacetime constraints,” in *Proceedings of the 23rd Annual 2323  
Conference on Computer Graphics and Interactive Techniques*, ser. SIGGRAPH 2324  
'96. New York, NY, USA: Association for Computing Machinery, Aug. 1996, pp. 2325  
147–154. 2326
- [49] Y. Li, T. Wang, and H.-Y. Shum, “Motion texture: A two-level statistical model 2327  
for character motion synthesis,” *ACM Trans. Graph.*, vol. 21, no. 3, pp. 465–472, 2328  
Jul. 2002. 2329
- [50] R. B. Dannenberg, W. P. Birmingham, G. P. Tzanetakis, C. P. Meek, N. P. Hu, 2330  
and B. P. Pardo, “The MUSART Testbed for Query-by-Humming Evaluation,” 2331  
*Comput. Music J.*, vol. 28, no. 2, pp. 34–48, Jun. 2004. 2332
- [51] K.-C. Li, M. Yan, and S. Yuan, “A Simple Statistical Model for Depicting the 2333  
Cdc15-Synchronized Yeast Cell-Cycle Regulated Gene Expression Data,” *Statistica 2334  
Sinica*, vol. 12, no. 1, pp. 141–158, 2002. 2335
- [52] G. E. A. P. A. Batista, E. J. Keogh, O. M. Tataw, and V. M. A. de Souza, “CID: An 2336  
efficient complexity-invariant distance for time series,” *Data Mining and Knowledge 2337  
Discovery*, vol. 28, no. 3, pp. 634–669, May 2014. 2338
- [53] A. W.-C. Fu, E. Keogh, L. Y. H. Lau, C. A. Ratanamahatana, and R. C.-W. Wong, 2339  
“Scaling and time warping in time series querying,” *The VLDB Journal*, vol. 17, 2340  
no. 4, pp. 899–921, Jul. 2008. 2341

- 2342 [54] Y. Shen, Y. Chen, E. Keogh, and H. Jin, “Searching Time Series with Invariance to  
 2343 Large Amounts of Uniform Scaling,” in *2017 IEEE 33rd International Conference*  
 2344 *on Data Engineering (ICDE)*, Apr. 2017, pp. 111–114.
- 2345 [55] ——, “Accelerating Time Series Searching with Large Uniform Scaling,” in *Pro-  
 2346 ceedings of the 2018 SIAM International Conference on Data Mining (SDM)*, ser.  
 2347 Proceedings. Society for Industrial and Applied Mathematics, May 2018, pp.  
 2348 234–242.
- 2349 [56] C. C. Aggarwal and C. K. Reddy, Eds., *Data Clustering: Algorithms and Applica-  
 2350 tions*, 1st ed. Boca Raton: Chapman and Hall/CRC, Aug. 2013.
- 2351 [57] P. Esling and C. Agon, “Time-series data mining,” *ACM Computing Surveys*,  
 2352 vol. 45, no. 1, pp. 1–34, Nov. 2012.
- 2353 [58] T. Rakthanmanon, B. Campana, A. Mueen, G. Batista, B. Westover, Q. Zhu,  
 2354 J. Zakaria, and E. Keogh, “Addressing Big Data Time Series: Mining Trillions of  
 2355 Time Series Subsequences Under Dynamic Time Warping,” *ACM Trans. Knowl.  
 2356 Discov. Data*, vol. 7, no. 3, pp. 10:1–10:31, Sep. 2013.
- 2357 [59] C. W. Tan, F. Petitjean, and G. I. Webb, “Elastic bands across the path: A new  
 2358 framework and method to lower bound DTW,” in *Proceedings of the 2019 SIAM*  
 2359 *International Conference on Data Mining (SDM)*, ser. Proceedings. Society for  
 2360 Industrial and Applied Mathematics, May 2019, pp. 522–530.
- 2361 [60] A. Shifaz, C. Pelletier, F. Petitjean, and G. I. Webb, “Elastic similarity and distance  
 2362 measures for multivariate time series,” *Knowledge and Information Systems*, vol. 65,  
 2363 no. 6, pp. 2665–2698, Jun. 2023.
- 2364 [61] S. Salvador and P. Chan, “Toward accurate dynamic time warping in linear time  
 2365 and space,” *Intelligent Data Analysis*, vol. 11, no. 5, pp. 561–580, Oct. 2007.
- 2366 [62] E. Keogh, T. Palpanas, V. B. Zordan, D. Gunopoulos, and M. Cardle, “Indexing large  
 2367 human-motion databases,” in *Proceedings of the Thirtieth International Conference*  
 2368 *on Very Large Data Bases - Volume 30*, ser. VLDB ’04. Toronto, Canada: VLDB  
 2369 Endowment, Aug. 2004, pp. 780–791.
- 2370 [63] D. Yankov, E. Keogh, J. Medina, B. Chiu, and V. Zordan, “Detecting time series  
 2371 motifs under uniform scaling,” in *Proceedings of the 13th ACM SIGKDD Interna-  
 2372 tional Conference on Knowledge Discovery and Data Mining*, ser. KDD ’07. New  
 2373 York, NY, USA: Association for Computing Machinery, Aug. 2007, pp. 844–853.
- 2374 [64] Y. Zhu and D. Shasha, “Warping indexes with envelope transforms for query by  
 2375 humming,” in *Proceedings of the 2003 ACM SIGMOD International Conference on*

- Management of Data*, ser. SIGMOD '03. New York, NY, USA: Association for Computing Machinery, Jun. 2003, pp. 181–192. 2377
- [65] E. Keogh and C. A. Ratanamahatana, “Exact indexing of dynamic time warping,” 2378  
*Knowledge and Information Systems*, vol. 7, no. 3, pp. 358–386, Mar. 2005. 2379
- [66] S.-W. Kim, S. Park, and W. Chu, “An index-based approach for similarity search 2380  
supporting time warping in large sequence databases,” in *Proceedings 17th Intern- 2381  
ational Conference on Data Engineering*, Apr. 2001, pp. 607–614. 2382
- [67] C. W. Tan, M. Herrmann, G. Forestier, G. I. Webb, and F. Petitjean, “Efficient 2383  
search of the best warping window for Dynamic Time Warping,” in *Proceedings of 2384  
the 2018 SIAM International Conference on Data Mining (SDM)*, ser. Proceedings. 2385  
Society for Industrial and Applied Mathematics, May 2018, pp. 225–233. 2386
- [68] C. A. Ratanamahatana and E. Keogh, “Everything you know about Dynamic Time 2387  
Warping is Wrong,” in *3 Rd International Workshop on Mining Temporal and 2388  
Sequential Data (TDM-04)*. Citeseer, 2004. 2389
- [69] H. A. Dau, A. Bagnall, K. Kamgar, C.-C. M. Yeh, Y. Zhu, S. Gharghabi, C. A. 2390  
Ratanamahatana, and E. Keogh, “The UCR time series archive,” *IEEE/CAA Jour- 2391  
nal of Automatica Sinica*, vol. 6, no. 6, pp. 1293–1305, Nov. 2019. 2392
- [70] M. Middlehurst, A. Ismail-Fawaz, A. Guillaume, C. Holder, D. Guijo-Rubio, G. Bu- 2393  
latova, L. Tsaprounis, L. Mentel, M. Walter, P. Schäfer, and A. Bagnall, “Aeon: 2394  
A Python Toolkit for Learning from Time Series,” *Journal of Machine Learning 2395  
Research*, vol. 25, no. 289, pp. 1–10, 2024. 2396
- [71] N. Tatbul, T. J. Lee, S. Zdonik, M. Alam, and J. Gottschlich, “Precision and Recall 2397  
for Time Series,” in *Advances in Neural Information Processing Systems*, vol. 31. 2398  
Curran Associates, Inc., 2018. 2399
- [72] M. Leodolter, C. Plant, and N. Brändle, “IncDTW: An R Package for Incremental 2400  
Calculation of Dynamic Time Warping,” *Journal of Statistical Software*, vol. 99, 2401  
pp. 1–23, Sep. 2021. 2402
- [73] G. Lai, W.-C. Chang, Y. Yang, and H. Liu, “Modeling Long- and Short-Term 2403  
Temporal Patterns with Deep Neural Networks,” in *The 41st International ACM 2404  
SIGIR Conference on Research & Development in Information Retrieval*, ser. SIGIR 2405  
’18. New York, NY, USA: Association for Computing Machinery, Jun. 2018, pp. 2406  
95–104. 2407
- [74] C. Chatfield, *The Analysis of Time Series: An Introduction*, Sixth ed. 2408  
New York: Chapman and Hall/CRC, Jul. 2003. 2409

- 2410 [75] O. Y. Al-Jarrah, P. D. Yoo, S. Muhaidat, G. K. Karagiannidis, and K. Taha,  
2411 “Efficient Machine Learning for Big Data: A Review,” *Big Data Research*, vol. 2,  
2412 no. 3, pp. 87–93, Sep. 2015.
- 2413 [76] W. Li and K. L. E. Law, “Deep Learning Models for Time Series Forecasting: A  
2414 Review,” *IEEE Access*, vol. 12, pp. 92 306–92 327, 2024.
- 2415 [77] N. I. Sapankevych and R. Sankar, “Time Series Prediction Using Support Vector  
2416 Machines: A Survey,” *IEEE Computational Intelligence Magazine*, vol. 4, no. 2,  
2417 pp. 24–38, May 2009.
- 2418 [78] Z. Chen, M. Ma, T. Li, H. Wang, and C. Li, “Long sequence time-series forecasting  
2419 with deep learning: A survey,” *Information Fusion*, vol. 97, p. 101819, Sep. 2023.
- 2420 [79] J. F. Torres, D. Hadjout, A. Sebaa, F. Martínez-Álvarez, and A. Troncoso, “Deep  
2421 Learning for Time Series Forecasting: A Survey,” *Big Data*, vol. 9, no. 1, pp. 3–21,  
2422 Feb. 2021.
- 2423 [80] D. B. da Silva, D. Schmidt, C. A. da Costa, R. da Rosa Righi, and B. Eskofier,  
2424 “DeepSigns: A predictive model based on Deep Learning for the early detection of  
2425 patient health deterioration,” *Expert Systems with Applications*, vol. 165, p. 113905,  
2426 Mar. 2021.
- 2427 [81] N. Wu, B. Green, X. Ben, and S. O’Banion, “Deep Transformer Models for Time  
2428 Series Forecasting: The Influenza Prevalence Case,” Jan. 2020.
- 2429 [82] F. Martínez-Álvarez, G. Asencio-Cortés, J. F. Torres, D. Gutiérrez-Avilés,  
2430 L. Melgar-García, R. Pérez-Chacón, C. Rubio-Escudero, J. C. Riquelme, and  
2431 A. Troncoso, “Coronavirus Optimization Algorithm: A Bioinspired Metaheuristic  
2432 Based on the COVID-19 Propagation Model,” *Big Data*, vol. 8, no. 4, pp. 308–322,  
2433 Aug. 2020.
- 2434 [83] F. Martínez, M. P. Frías, M. D. Pérez, and A. J. Rivera, “A methodology for ap-  
2435 plying k-nearest neighbor to time series forecasting,” *Artificial Intelligence Review*,  
2436 vol. 52, no. 3, pp. 2019–2037, Oct. 2019.
- 2437 [84] S. Tajmouati, B. E. L. Wahbi, A. Bedoui, A. Abarda, and M. Dakkon, “Applying  
2438 k-nearest neighbors to time series forecasting: Two new approaches,” *Journal of  
2439 Forecasting*, vol. 43, no. 5, pp. 1559–1574, 2024.
- 2440 [85] D. T. Thi, N. T. Phong, and N. D. Bui, “Forecast Timeseries Based On Matrix  
2441 Profile,” *Journal of Informatics and Innovative Technologies (JIIT)*, 2021.

- [86] C.-C. M. Yeh, Y. Zhu, L. Ulanova, N. Begum, Y. Ding, H. A. Dau, D. F. Silva, A. Mueen, and E. Keogh, “Matrix Profile I: All Pairs Similarity Joins for Time Series: A Unifying View That Includes Motifs, Discords and Shapelets,” in *2016 IEEE 16th International Conference on Data Mining (ICDM)*. Barcelona, Spain: IEEE, Dec. 2016, pp. 1317–1322. 2442  
2443  
2444  
2445  
2446
- [87] Y. Zhu, M. Imamura, D. Nikovski, and E. Keogh, “Matrix Profile VII: Time Series Chains: A New Primitive for Time Series Data Mining,” in *2017 IEEE International Conference on Data Mining (ICDM)*, Nov. 2017, pp. 695–704. 2447  
2448  
2449
- [88] S. M. Law, “STUMPY: A Powerful and Scalable Python Library for Time Series Data Mining,” *Journal of Open Source Software*, vol. 4, no. 39, p. 1504, Jul. 2019. 2450  
2451
- [89] G. E. P. Box, G. M. Jenkins, G. C. Reinsel, and G. M. Ljung, *Time Series Analysis: Forecasting and Control*. John Wiley & Sons, May 2015. 2452  
2453
- [90] S. Elsayed, D. Thyssens, A. Rashed, H. S. Jomaa, and L. Schmidt-Thieme, “Do We Really Need Deep Learning Models for Time Series Forecasting?” Oct. 2021. 2454  
2455
- [91] G. E. P. Box and D. A. Pierce, “Distribution of Residual Autocorrelations in Autoregressive-Integrated Moving Average Time Series Models,” *Journal of the American Statistical Association*, vol. 65, no. 332, pp. 1509–1526, 1970. 2456  
2457  
2458
- [92] B. Lim and S. Zohren, “Time-series forecasting with deep learning: A survey,” *Philosophical Transactions of the Royal Society A: Mathematical, Physical and Engineering Sciences*, vol. 379, no. 2194, p. 20200209, Feb. 2021. 2459  
2460  
2461
- [93] G. U. Yule, “On a Method of Investigating Periodicities in Disturbed Series, with Special Reference to Wolfer’s Sunspot Numbers,” *Philosophical Transactions of the Royal Society of London. Series A, Containing Papers of a Mathematical or Physical Character*, vol. 226, pp. 267–298, 1927. 2462  
2463  
2464  
2465
- [94] R. J. Williams and D. Zipser, “A Learning Algorithm for Continually Running Fully Recurrent Neural Networks,” *Neural Computation*, vol. 1, no. 2, pp. 270–280, Jun. 1989. 2466  
2467  
2468
- [95] K. P. Murphy, *Probabilistic Machine Learning: An Introduction*, ser. Adaptive Computation and Machine Learning. Cambridge, Massachusetts London, England: The MIT Press, 2022. 2469  
2470  
2471
- [96] S. Kolassa and W. Schütz, “Advantages of the MAD/Mean Ratio over the MAPE,” *Foresight: The International Journal of Applied Forecasting*, vol. 6, pp. 40–43, 2007. 2472  
2473

- 2474 [97] J. H. Friedman, “Greedy function approximation: A gradient boosting machine.”
- 2475     *The Annals of Statistics*, vol. 29, no. 5, pp. 1189–1232, Oct. 2001.
- 2476 [98] L. G. Serrano and S. Thrun, *Grokking Machine Learning*. Shelter Island: Manning,
- 2477     2021.
- 2478 [99] A. Géron, *Hands-On Machine Learning with Scikit-Learn and PyTorch: Concepts,*
- 2479     *Tools, and Techniques to Build Intelligent Systems*. US: O'Reilly Media, 2025.
- 2480 [100] T. Chen and C. Guestrin, “XGBoost: A Scalable Tree Boosting System,” in *Proceedings of the 22nd ACM SIGKDD International Conference on Knowledge Discovery and Data Mining*, ser. KDD ’16. New York, NY, USA: Association for Computing Machinery, Aug. 2016, pp. 785–794.
- 2484 [101] A. V. Dorogush, V. Ershov, and A. Gulin, “CatBoost: Gradient boosting with categorical features support,” in *Workshop on ML Systems at NIPS 2017*, 2017.
- 2486 [102] G. Ke, Q. Meng, T. Finley, T. Wang, W. Chen, W. Ma, Q. Ye, and T.-Y. Liu,
- 2487     “LightGBM: A Highly Efficient Gradient Boosting Decision Tree,” in *Advances in Neural Information Processing Systems*, vol. 30. Curran Associates, Inc., 2017.
- 2489 [103] R. Sen, H.-F. Yu, and I. S. Dhillon, “Think Globally, Act Locally: A Deep Neural Network Approach to High-Dimensional Time Series Forecasting,” in *Advances in Neural Information Processing Systems*, vol. 32. Curran Associates, Inc., 2019.
- 2492 [104] C.-C. M. Yeh, N. Kavantzas, and E. Keogh, “Matrix Profile VI: Meaningful Multidimensional Motif Discovery,” in *2017 IEEE International Conference on Data Mining (ICDM)*, Nov. 2017, pp. 565–574.